



*Instytut Podstawowych Problemów Techniki
Polska Akademia Nauk*

DOCTOR OF PHILOSOPHY THESIS

**Molecular Acoustic and
Advanced Signal Processing
Backgrounds of Acoustocerebrography**

by
Mirosław Krystian Wróbel

**PhD supervisors: Prof. Andrzej Nowicki Ph.D., Dr. Habil., Eng.
Robert Olszewski, Ph.D., Dr. Habil., MD**
PhD co-supervisor: Marcin Lewandowski, Ph.D.

2019

This dissertation is lovingly dedicated to my wife Anna and my son Matthias whose patience and support gave me the inspiration to complete my doctorate.

Acknowledgments

During the creation of this thesis I was fortunate to have the help of many people. Without their aid this work, and the associated medical experiments, might never have been completed. Their contributions included performing the animal und human medical trials, text reviews, discussing data processing and providing key suggestions for some algorithms and mathematical formulas. The author would be remiss in omitting Prof. Andrzej Nowicki, who has helped him in many years of working on this fascinating topic through his constant interest and encouragement to work on the field of molecular acoustics theoretically and experimentally. My special thanks go to Prof. Robert Olszewski MD, Department of Gerontology, Public Health and Didactics National Institute of Geriatrics, Rheumatology and Rehabilitation, with whom I have a long-standing collaboration and who has always encouraged me as a medical supervisor to this dissertation, as well as Doctor Marcin Lewandowski of the Institute of Fundamental Technological Research, Polish Academy of Sciences, for his mathematical and engineering supervision of this work.

I am also indebted to my mathematics and medical colleagues in Leipzig, for their contributions to the editing of this work and for creating an atmosphere in which I could learn a lot from their knowledge and practice. Adam Kolany, Angelika Mucha, Paul Schmude, Pawel Karlowicz and Andrzej Dabrowski have contributed to and criticized initial drafts of a large portions of text. I am also indebted to the other colleagues, veterinarian Antje Dreyer, Björn Nitzsche and Johannes Boltze, who have supplied me with a large part of medical material from our joint experiments used for this thesis. My thanks also go to my colleague Mr. James Parsons, who helped me a lot in reading the corrections and proofreading the final drafts. Finally, I also would thank many of my Sonovum AG colleagues who have supported me in this research project.

Abstract

Molecular Acoustic and Advanced Signal Processing Backgrounds of Acoustocerebrography

by

Mirosław Krystian Wróbel
Doctor of Philosophy

Instytut Podstawowych Problemów Techniki
Polska Akademia Nauk

This work describes the latest innovative development on the use of ultrasound quasi-constant wave packages at different frequencies to track the dispersion properties of intracranial tissues which may have been altered due to traumatic or other neurological brain injuries. A new medical innovation, called Acousto-Cerebro-Graphy or short ACG, use dispersive ultrasound and does not provide imaging. It can provide data of significant diagnostic value by using decision support systems that can be trained as a medical diagnostic system for different brain pathologies applications, to detect specific patterns of dispersion that are associated with specific intracranial injuries. The background of here presented approach, is the molecular acoustic. “The molecular acoustics teach the mechanism of the transmission of sound energy through real molecules in liquids and gases”. By the above given definition, the molecular acoustics are essentially limited to the discussion of sound velocity and sound absorption. Nevertheless, the advanced signal processing and system developments relevant to this novel diagnostic concept have been completed as well as the necessary medical experiments. Additionally, some simulations to support the ACG ultrasound diagnostic concept theoretical basis capabilities are also offered. Furthermore, in early medical experiments ACG dispersive ultrasound technology has been used successfully to identify e.g. stroke or sepsis associated encephalopathy, based on the ultrasonic dispersion pattern they produce. Today a correct diagnosis, in the early phases of brain disorders, can only be made by a very experienced specialist, such as a neurologist or psychiatrist, who can interpret a patient’s initial symptoms. Unfortunately, similarly to mental health problems, other brain illnesses such as traumatic brain injuries are hard to detect or to track with standard imaging or bio-chemical analysis. On the one hand, these are often too minor to occur on the single image, and on the other hand, they are too fast for chemical analysis, thus making it difficult to treat them effectively. The investigation proposes described in this work, the use of dispersive ultrasound as a non-invasive diagnostic system for brain applications may close the gap.

Streszczenie

Akustyka molekularna i zaawansowane przetwarzanie sygnałów
– techniczne podstawy akustocerebrografii

Praca Doktorska
Mirosław Krystian Wróbel

Instytut Podstawowych Problemów Techniki
Polska Akademia Nauk

W pracy opisano najnowsze innowacyjne rozwiązanie dotyczące zastosowania ultradźwiękowych quasi-stałych pakietów fal o różnych częstotliwościach w celu śledzenia dyspersyjnych właściwości tkanek mózgowych (wewnątrzczaszkowych), które mogły ulec zmianie z powodów urazowych lub innych neurologicznych uszkodzeń mózgu. Ta nowa, nie obrazowa metoda medyczna zwana Akusto-Cerebro-Grafią lub krótko ACG, wykorzystuje jako podstawę pomiarów dyspersję ultradźwięków w biologicznych strukturach tkankowych. Może ona dostarczać informacje o znacznej wartości diagnostycznej, gdy połączy się obróbkę danych z systemami wspomagania decyzji. Systemy te można wytrenować jako automatyczne systemy decyzyjne do zróżnicowanych zastosowań diagnostycznych patologii mózgu, lub w celu wykrycia określonych wzorców, które są związane z konkretnymi uszkodzeniami wewnątrzczaszkowymi. Podstawą przedstawionego tu podejścia jest akustyka molekularna. "Akustyka molekularna opisuje mechanizm przekazywania energii dźwięku przez rzeczywiste cząsteczki w cieczach i gazach" – zgodnie z tą definicją, akustyka molekularna ogranicza się zasadniczo do omówienia zmian prędkości dźwięku oraz absorpcji w danym medium. Wykorzystanie zaawansowanego przetwarzania sygnałów pozwoliło na skonstruowanie systemu pozwalającego na weryfikację tej nowej koncepcji diagnostycznej, a także na wykonanie niezbędnych eksperymentów medycznych. Praca ta prezentuje także symulacje wspomagające teoretyczną koncepcję podstaw diagnostyki ACG. W przeprowadzonych wczesnych eksperymentach medycznych, z powodzeniem zastosowano dyspersyjną technikę ultradźwiękową ACG w celu identyfikacji m.in. udaru mózgu oraz posocznicy, w oparciu o ich specyficzny dyspersyjny wzorzec ultradźwiękowy. Dzisiaj, prawidłową diagnozę, we wczesnych fazach zaburzeń mózgu, może dokonać tylko bardzo doświadczony specjalista neurolog lub psychiatra, który potrafi zinterpretować początkowe objawy pacjenta. Niestety, podobnie jak w przypadku problemów ze zdrowiem psychicznym, również inne choroby mózgu, takie jak np. urazowe uszkodzenie mózgu, są trudne do wykrycia lub monitorowania przy pomocy standardowego obrazowania, czy też analiz bio-chemicznych. Z jednej strony zmiany są często zbyt małe, aby mogły występować na pojedynczym obrazie, z drugiej zaś strony są zbyt szybkie dla analiz chemicznych, co utrudnia ich skuteczną diagnozę i terapię. Celem badań eksploracyjnych opisanych w tej pracy, było użycie dyspersyjnych ultradźwięków jako nieinwazyjnej metody, która mogłaby wypełnić tę lukę w zaawansowanej diagnostyce mózgu.

Table of Contents

<i>Acknowledgments</i>	<i>i</i>
<i>Abstract</i>	<i>ii</i>
<i>Streszczenie</i>	<i>iii</i>
<i>Table of Contents</i>	<i>iv</i>
<i>List of Symbols</i>	<i>vii</i>
<i>Chapter A</i>	<i>1</i>
2 <i>Chapter 1</i>	<i>1</i>
2.1 Introduction.....	1
2.2 General description of the acoustic - physical and molecular basics.....	1
2.3 General characteristics of the brain anatomical and physiological environment.....	12
3 <i>Chapter 2</i>	<i>17</i>
3.1 General characteristics of the brain anatomical and physiological environment.....	17
3.2 Brain vascular system	18
3.2.1 The Arteries.....	18
3.2.2 The Veins	19
3.3 Intracranial pressure ICP.....	21
3.4 Cerebrospinal fluid CSF	24
4 <i>Chapter 3</i>	<i>26</i>
4.1 The basics configuration of ACG measurement.....	26
4.2 Dispersive Ultrasound as Non-Invasive Diagnostic System.....	33
5 <i>Chapter 4</i>	<i>36</i>
5.1 Dispersive Ultrasound as Non-Invasive Diagnostic System.....	36
5.2 Phase estimation for dispersive ultrasound.....	36
5.3 Lead time determination T_p	39
5.4 Matlab™ procedure for the phase calculating	41
5.5 Matrix algorithm for determining the phase and amplitude.....	45
5.6 Matlab™ matrix procedure for phase calculation.....	51
6 <i>Chapter 5</i>	<i>54</i>

6.1	Microchip devices for phase vector and bias block retrieving of the sampled monochromatic signal	54
6.2	Simulink™ simulator of monochrome Signal Phase Vector Determination Circuit	56
6.3	Simulink™ simulator of a Block Processors	57
6.4	Block processor model	57
6.5	Stream processors	62
6.6	Simulink™ simulator of the stream processor	65
6.7	TRI stream processors	66
6.8	LSM stream processors	68
6.9	Averaging module	71
7	<i>Chapter 6</i>	74
7.1	Multispectral – phase vector estimation from polychromatic signal [1]	74
7.2	Phase estimating and minimizing the errors	77
7.3	Unwinding	78
7.4	Choice of Initial phases	81
8	<i>Chapter 7</i>	83
8.1	Portable ACG system for animal und human trials	83
8.2	System configuration and technical parameters	84
8.3	System structure and the main board parameters	85
8.4	Advance TUS system parameters	87
9	<i>Chapter 8</i>	89
9.1	Maximal Stress	89
9.2	Summary experimental description	89
9.3	MRI evaluation	91
9.4	Pathological evaluations	92
9.5	Histological evaluation	92
9.6	Summary	94
10	<i>Chapter 9</i>	96
10.1	Portable ACG system for human clinical trials	96
10.2	Basic idea of the ACG measurement process	97
10.3	First analysis: Classifying with the aim 4 groups	98

10.4	Advance dynamic application for septic encephalopathy diagnosis	101
<i>11</i>	<i>Chapter 10</i>	<i>110</i>
11.1	Conclusion und Outlook.....	110
	<i>Table of Illustration</i>	<i>I</i>
	<i>Table of Tables</i>	<i>V</i>
	<i>References</i>	<i>VI</i>
	<i>STATUTORY DECLARATION</i>	<i>XI</i>

List of Symbols

μ	Shear modulus
ACG	Acousto-Cerebro-Graphy
ADC	Analog Digital Converter
AF	Atrial fibrillation
a_{ik}	Elastic state of element
APACHE II	Acute Physiology, Age, Chronic Health Evaluation II is a severity-of-disease classification system
ATP	Adenosine triphosphate
ATT	Attenuation
bpm	Beats per minute - Heart
c	Speed of sound
C	Cosine sequence comprising cosine values, Compliance
CAM-ICU	Confusion Assessment Method for the Intensive Care Unit
CBF	Cerebral blood flow
c_{ik}	Elasticity coefficients
CLK	Timing input - CLOCK
CSF	Cerebrospinal fluid
CT	Computed Tomography
d	Distance
DAC	Digital Analog Converter
DICOM	Digital Imaging and Communications in Medicine
DICV	Change in intracranial volume (cerebral)
DMA	Direct memory access
DP	Change in pressure (cerebral)
DSP	Digital signal processor
DWI	Diffusion Weighted Imaging, Diffusion Disorders
E	Internal energy, Elasticity modulus
EMIF	External Memory Interface
EOPS	Exa operations per second
FIFO	First In – First Out
f_p	Sampling frequency
FPGA	Field Programmable Gate Array
f_s	Signal frequency
GA	Genetic algorithm
GBM	General Boosting Machine
HT	Hyper tensions
ICDSC	Intensive Care Delirium Screening Checklist
ICP	Intracranial pressure
ICV	Intracranial volume
K	Compression module
L	Tissue layers
LSM	Streaming processor based on arbitrary amount of values taken from the data bus
LVDS	Low Voltage Differential Signaling
m	Mass
M	Molecular weight

MAP	Mean arterial pressure
MPF	Monochromatic phase processors
MPS	Measurements per second
MRI	Magnetic Resonance Imaging
mTBI	mild Traumatic Brain Injury
MTT	Mean transit time
P	Oscillation periods, Pressure
PC	Personal computer
PCT	Patent Cooperation Treaty, Procalcitonin
PET	Positron Emission Tomography
PRU	Peripheral Resistance Unit
PWI	Perfusion weighted imaging, perfusion disorders
Q	Flow through the blood vessel
R	Phase relations, Peripheral resistance
RASS	Richmond Agitation Sedation Scale
RES	Reset
S	Sine sequence comprising sine values, Entropy
SAE	Sepsis Associated Encephalopathy
SD	Standard deviation
SHT	Severe Traumatic Brain Injury
SoC	System on Chip
SOFA	Sepsis-related organ failure assessment score
SPS	Sampling rate - Samples per Second
T	Period
TBI	Traumatic Brain Injury
TOF	Time of flight
TPR	Total peripheral vascular resistance
TRI	Streaming processor based on three consecutive values taken from the data bus
TUS	Transcranial transmission ultrasound
U	Phase real part
USG	Ultrasound
V	Phase imaginary part, Volume
WMH	White matter hyperintensities
WML	White matter hyperintensities
Y	Receiving signal sequence
β	Bias - means establishing predetermined proper operating conditions and values - the operating point of a device
β_{ad}	Adiabatic compressibility
β_{is}	Isothermal compressibility
δ and μ	Lamé parameters
δA	Volume compression
δQ	Molar heat quantity
ε	Energy density
λ	Wavelength
ρ	Density
σ	Poisson's transverse contraction coefficient
φ	Phase
χ	Specific heats

Chapter A

Introduction

The brain is a complex organ and it is sensitive on external influences. Unlike the heart, liver or lung, an oxygen deficiency of eight to ten minutes can result in cell death. It needs special protection - already at the beginning of life. More than any other organ of the body, brain integrity depends on the continuous blood supply of oxygen and glucose for covering the energy demands of the tissue. Cessation or severe reduction of blood flow results in almost instantaneous biochemical and functional deficits which become rapidly irreversible unless the blood flow is promptly restored. The ischemia time that is tolerated by the brain depends, among other things, on the density of ischemia, the tissue concentration of primary and secondary energy stores and the rate of energy consumption which, in turn, depends on the temperature, the degree of functional activity and the absence or presence of anesthetics or other drugs. Timely and rapid detection of Brain Pathologies as Stroke, Traumatic Brain Injury (TBI) or Sepsis Associated Cranial Pathologies (SAE) remains a major challenge in medical field of diagnostics and operations. Mortality and morbidity from such pathologies can be reduced if they are quickly diagnosed and treated even in far-forward medical aid stations and ambulances, where sophisticated diagnostic tools such Computed Tomography (CT) and Magnetic Resonance Imaging (MRI) are limited or not available. As such, there is a pressing need for portable diagnostic tools that can be deployed for early detection of neurological injury in emergency situations, where such injuries are most likely to occur.

For the purposes of this Doctor of Philosophy Work author formulated a following thesis:

“Molecular Acoustic and Advance Signal Processing Backgrounds of Acoustocerebrography”

- *In order to prove the thesis, author has established the set of tasks and goals, the fulfillment of which will be the same as proving the thesis:*
- *analysis of physical issues related to acoustical wave propagation in amorph matter and ultrasonic wave dispersion in such matter. The quick description of the molecular acoustic background is given in chapter 1,*
- *analyzing the known data of the human cranial tissue and human cerebrovascular system as well as the interpretation of the biological process influence on the physical parameters of the acoustic wave propagation. The complex cranium and brain tissue are topic of chapter 2,*

- *development of a human cranium model and construction of a real control system implementing an acoustic signal measurement method such as requirement specification for such theoretical system are presented in chapter 3,*
- *chapter 4 conduct a review of already available methods for cranial tissue examination with deep analysis of its mathematical computational basis and propose some improvement of it,*
- *creating computational models for the new absolute filter signal processing method using simulation software. Where the method corresponds to the projection of the sampled signal interpreted as a single vector point of the N-dimensional Euclidean complex space into a subspace determined by target frequencies are deeply and explicit explain by chapter 5 and 6 which is the main part of the work,*
- *chapter 7 describe how the theoretical system requirement specification combine with the new computational method assumptions can be turn into a real diagnostic System.*
- *analysis of legal conditions for transcranial medical ultrasound diagnostic system and a safety test with the focus on the biological tissue effect caused by overdose exposure of the presented ultrasound system are reveal in chapter 8.*
- *example analysis of early human medical trials in which the application of dispersive ultrasound technology and dispersion pattern classification has been successfully used is offered in chapter 9*

This work describes the latest innovative development on the use of ultrasound quasi-constant wave packages at different frequencies to track the dispersion properties of intracranial tissues which may have been altered due to traumatic or other neurological brain injury. A new medical innovation, called Acousto-Cerebro-Graphy or short ACG, use dispersive ultrasound and does not provide imaging. It can provide data of significant diagnostic value by using decision support systems that can be trained as a medical diagnostic system for different brain pathologies applications, to detect specific patterns of dispersion that are associated with specific intracranial injuries [1]. The signal processing and system developments relevant to this ACG novel diagnostic concept have been completed as well as the necessary medical experiments.

1 Chapter 1

1.1 Introduction

Traditional diagnostic methods require information from medical imaging technologies and chemical analysis of bodily fluids. Currently, scientific advances in medical diagnostic imaging such as Magnetic Resonance Imaging (MRI), Computed Tomography (CT) or even Ultrasound (USG), have reached very high standards. These technologies provide comprehensive geometrical information about a patient's internal tissue structure but contain little information about its bio-chemical composition. On the other hand, laboratory analysis of biological and chemical components of a patient's blood, cerebrospinal fluid (CSF) or brain tissue provides very good information about the composition of all single substances, for instance by using chromatography, but not about the tissue structure. Furthermore, many brain tissue pathologies are often difficult to detect with standard medical imaging as minor changes in the brain tissue do not show any discrepancies in the picture that was taken. A correct diagnosis, in the early phases of such brain disorders can only be made by a very experienced specialist, such as a neurologist or psychiatrist, who can interpret a patient's initial symptoms. Unfortunately, similarly to mental health problems, other brain illnesses such as traumatic brain injuries are hard to detect or to track with standard imaging or bio-chemical analysis. On the one hand, these are often too minor to occur on the single image, and on the other hand, they are too fast for chemical analysis, thus making it difficult to treat them effectively. The, described in this work, ACG investigation proposes the use of dispersive ultrasound as a non-invasive diagnostic system for brain applications to close the gap by bringing a mobile device to the patient. The background of presented approach is the molecular acoustic. "The molecular acoustics teach the mechanism of the transmission of sound energy through real molecules in liquids and gases" as per definition [2]. In molecular acoustics, liquids and gases are investigated because these aggregate states are characterized by the properties of the single molecule. For the aggregation of solid state, which finds its clearest expression in the crystal, the concept of molecule is not quite applicable. Here, the parent cells of a crystal lattice replace the single molecule in a molecule swarm. By the above given definition, the molecular acoustics are essentially limited to the discussion of sound velocity and sound absorption. The sound waves themselves may be those of periodic nature and small vibration amplitude or have the shape of shock waves. In the medicine the behavior of the cells and molecules are of interest instead of the atoms or gaseous and liquid molecules. This made it clear, that the study of the cellular and molecular structure of biological matter or tissue can't stop even in the field of molecular acoustics.

1.2 General description of the acoustic - physical and molecular basics

Already in ancient times the first atomic theorist Δημόκριτος (Democritus) taught us that matter is built up from the smallest indivisible particles, which are similar in their substance, but

different in shape and size. Through the hypothesis of indivisibility, which is still valid in the framework of the today's mechanics, these elementary particles were given the name "atoms." With them, the "atomistic physicists" of the ancient Greek pre-Socratic philosophy had already declared the emergence and disintegration of things as the separation of the atoms passing away of a body. The creation of a body or matter was a gathering of atoms. So, they worked already with the concept of atoms combinations, which according to a suggestion of S. Cannizaro about 100 years ago, are call molecules today. But the true size of atoms and molecules could not even be vaguely hypothesized in ancient times.

Nothing was changed by Galileo and Newton, who established scientific mechanics as a doctrine of the material bodies movements and the forces causing them. This mechanical model of the matter uses extensively the concept of "material or substantial point." These points are thought to be infinitely small, but yet provided with mass and a certain field of force. Therefore, so defined elementary particles lack the complication of spatial extent. With the help of this working hypothesis, the Mechanics is divided in the kinematics and dynamics of material points and material point systems, in the mechanics of rigid bodies whose material points are always rigidly interconnected, and in the mechanics of the continuums, where the point systems are deformable and possess the property of elasticity the particles of these point systems, which are subjected to deformation, be in ordered or disordered motion. The previously described subgroup of the mechanics, the mechanics of the continuums, includes already the traditional acoustics. It is also considered and treated as part of the general wave and vibration theory. How little these mechanics and acoustics evaluate the material points as real atoms and molecules can be seen from many representations, but especially clear from the well-known historical-critical Ernst Mach publication entitled "Die Mechanik in ihrer Entwicklung" [3].

First the atomistic interpretation of the very extensive experimental observation material of chemistry on the one hand and the experimental development of the ultrasound field on the other, enabled a combination of acoustics and chemical constitutional theory. Only with this knowledge was it possible to answer several of the simplest questions, e.g. How does the speed of sound of a substance change when its chemical constitution changes? Is the sound energy supplied to a medium transformed into unordered thermal motion or does it make a detour via the internal vibrations of the molecules? This is the domain of the molecular acoustics research field as stated before.

The definitions of elastic stresses and deformations as well as the statements of sound waves and sound velocities elasticity theory relates to the sound field. The sound field is the area in which the transmission of sound impulses takes place from molecule to molecule. The properties of a sound field are described by a number of terms taken from the mechanics of the deformable point systems which were developed substantially in the last century [2].

The two most important properties for molecular acoustics are, as quoted above, the speed of sound and sound absorption. The train of thought outlined below deals with the question of which inner relationship exists between an elastic deformation and the resulting wave velocity. Under the influence of the force effects of a sound generator a medium is deformed. The

medium is called elastic if the deformations completely disappear after the cessation of the force effects. The description of this condition is based on a Cartesian coordinate system. The deforming force has the components X, Y, Z and put the medium in a mechanical stress state (Fig. 1) [4].

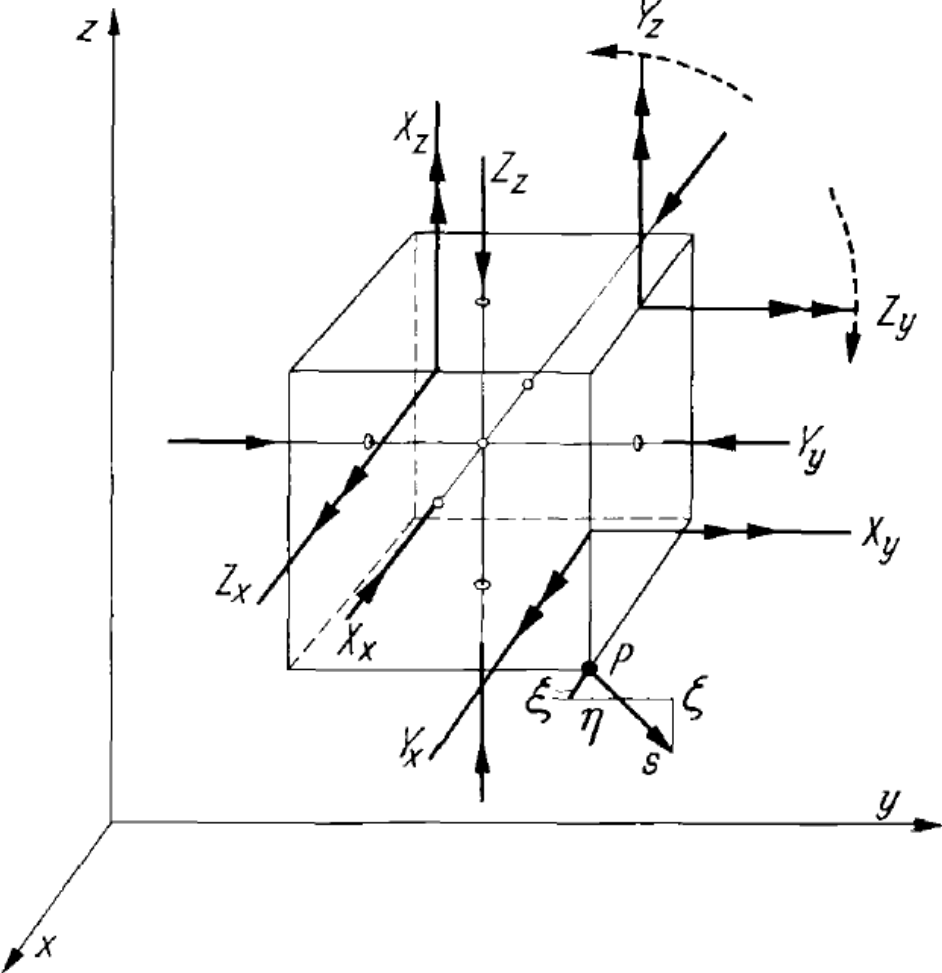


Figure 1: Normal pressures and shear stresses which act on a volume element of an elastically deformable medium [2]

This is described by the 6 components of the stress tensor, namely by three normal pressures

$$X_x, Y_y, Z_z$$

and by three shear stresses

$$X_y = Y_x, Y_z = Z_y, Z_x = X_z$$

The fact, that the shear stresses can be easily reduce from the number 6 to 3 values is simple, just considering the cube parallel axes and the coordinate according to fig. 1. The cube remains only at rest, if the cited Shear stresses are equal to each other. In the fig. 1, the normal pressures

have been drawn with simple arrows, the shear stresses with double arrows. The normal pressures have been taken as compression pressures, but they could as well have been drawn as tensile stresses. In order not to complicate the figure unnecessarily, the arrows for the shear stresses have been applied only on one side of the volume element. The shear stress Y_z alone would cause a rotation in the direction of the dotted arrow to the left, the shear stress Z_y alone, a turn to the right. The volume element remains at rest when both tensions are equal to each other, as already mentioned. The forces acting on the volume element according to figure 1, are the elastic stress forces and its lead to volume deformations. These are composed of "strains" and "shears" which are introduced in an analogous way by the designations.

$$x_x, y_y, z_z$$

and

$$x_y = y_x, y_z = z_y, z_x = x_z$$

These designations of the deformation tensor are the partial differential quotients

$$\frac{\partial \xi}{\partial x} = x_x, \frac{\partial \eta}{\partial y} = y_y, \frac{\partial \zeta}{\partial z} = z_z$$

$$\frac{\partial \zeta}{\partial y} + \frac{\partial \eta}{\partial z} = z_y = y_z$$

$$\frac{\partial \xi}{\partial z} + \frac{\partial \zeta}{\partial x} = x_z = z_x$$

$$\frac{\partial \eta}{\partial x} + \frac{\partial \xi}{\partial y} = y_x = x_y$$

If we consider the deformations of a volume element, they can be described by the spatial changes of small displacements ξ, η, ζ of the displacement vector s of a mass point between two closely adjacent path points. Such a mass point is for example the point P on figure 1. Of course, the pressures and tensions also apply in the Volume elements interior and can be described as shrinking together to the mass point P .

The answer to the question, what is the conceivable connection between the introduced deformation and tensions components of a medium in the sound field, is really simple and can be defined with the Hook's law [5]. Indeed, when the relation between infinitesimal deformations and the forces causing them is a linear one it is there a simplest connection. A medium which is elastic in the narrower sense, as it is in a sound field with small deformations, is one in which Hooke's law is given in the following general form

$$\begin{aligned}
X_x &= c_{11}x_x + c_{12}y_y + c_{13}z_z + c_{14}y_z + c_{15}z_x + c_{16}x_y \\
Y_y &= c_{21}x_x + c_{22}y_y + c_{23}z_z + c_{24}y_z + c_{25}z_x + c_{26}x_y \\
Z_z &= c_{31}x_x + c_{32}y_y + c_{33}z_z + c_{34}y_z + c_{35}z_x + c_{36}x_y \\
Y_z &= c_{41}x_x + c_{42}y_y + c_{43}z_z + c_{44}y_z + c_{45}z_x + c_{46}x_y \\
Z_x &= c_{51}x_x + c_{52}y_y + c_{53}z_z + c_{54}y_z + c_{55}z_x + c_{56}x_y \\
X_y &= c_{61}x_x + c_{62}y_y + c_{63}z_z + c_{64}y_z + c_{65}z_x + c_{66}x_y
\end{aligned} \tag{1}$$

This equation system possesses 36 c_{ik} elasticity coefficients. Using the Green-Gauss energy principle integral theorem to the equations system and the introduction the energy density ε (energy per unit volume) of the, by an adiabatic ultrasonic process elastically deformed medium, two important statements are made: one is, that the tension components on the left side of the equations system can be represented as differential quotients of the energy density ε , which is also referred to as the "adiabatic elastic potential". Second, the elastic potential ε is a homogeneous quadratic function given by the right side of deformation components. This leads to only 21 coefficient of elasticity having a following representation [2].

$$\begin{aligned}
-X_x &= \frac{\partial \varepsilon}{\partial x_x} = 2a_{11}x_x + 2a_{12}y_y + 2a_{13}z_z + 2a_{14}y_z + 2a_{15}z_x + 2a_{16}x_y \\
-Y_y &= \frac{\partial \varepsilon}{\partial y_y} = 2a_{12}x_x + 2a_{22}y_y + 2a_{23}z_z + 2a_{24}y_z + 2a_{25}z_x + 2a_{26}x_y \\
-Z_z &= \frac{\partial \varepsilon}{\partial z_z} = 2a_{13}x_x + 2a_{23}y_y + 2a_{33}z_z + 2a_{34}y_z + 2a_{35}z_x + 2a_{36}x_y \\
-Y_z &= \frac{\partial \varepsilon}{\partial y_z} = 2a_{14}x_x + 2a_{24}y_y + 2a_{34}z_z + 2a_{44}y_z + 2a_{45}z_x + 2a_{46}x_y \\
-Z_x &= \frac{\partial \varepsilon}{\partial z_x} = 2a_{15}x_x + 2a_{25}y_y + 2a_{35}z_z + 2a_{45}y_z + 2a_{55}z_x + 2a_{56}x_y \\
-X_y &= \frac{\partial \varepsilon}{\partial x_y} = 2a_{16}x_x + 2a_{26}y_y + 2a_{36}z_z + 2a_{46}y_z + 2a_{56}z_x + 2a_{66}x_y
\end{aligned} \tag{2}$$

Farther by Schaaffs, the 21 a_{ik} coefficients are describing the elastic state of element penetrated by sound waves in the most general case. A medium can be in the three aggregate states: solid, liquid and gaseous. The solid state comprises crystals and solid isotropic (or quasi-isotropic) bodies. For description of an isotropic solid in which the expression for the elastic potential is invariant against all rotations of a coordinate system, only two mutually independent coefficients of elasticity are sufficient, namely a_{11} and a_{44} . They are in the form of some mathematical elegance suggested by Gabriel Lamé.

$$\left. \begin{aligned}
\delta &= 2(a_{11} - 2a_{44}) \\
\mu &= 2a_{44}
\end{aligned} \right\} \tag{3}$$

δ and μ are therefore also called as the two Lamé constants or Lamé parameters.

The gaseous and liquid states of aggregation are summarized as a fluid body form. These latter have the property of having only a single elastic coefficient, making it easier to place the wealth of molecular-acoustical phenomena in an ordered system. Using the Lamé parameter, the elasticity theory for the elastic potential ε of the isotropic body provides the term

$$\varepsilon = \frac{1}{2} \delta (x_x + y_y + z_z)^2 + \mu \left(x_x^2 + y_y^2 + z_z^2 + \frac{1}{2} y_z^2 + \frac{1}{2} z_x^2 + \frac{1}{2} x_y^2 \right)$$

if this expression will be used in the Hooke equation system, then follows an equation for an isotropic or fluid body

$$\left. \begin{aligned} -X_x &= \delta(x_x + y_y + z_z) + 2\mu x_x \\ -Y_y &= \delta(x_x + y_y + z_z) + 2\mu y_y \\ -Z_z &= \delta(x_x + y_y + z_z) + 2\mu z_z \\ -Y_z &= \mu y_z \\ -Z_x &= \mu z_x \\ -X_y &= \mu x_y \end{aligned} \right\} \quad (4)$$

This formula group describes a static state of the volume elements of the medium. This state, however, was achieved dynamically by inserting the impressed forces at the mass points m of the medium of the macroscopic density ρ , initiating their movement and after then terminating it. The formal mathematical transfer of the static problem to a dynamic and vice versa is done with the help of d'Alembert's principle. It links the medium deformation state with the externally imprinted forces, the inherent inertial forces and the medium-specific material constants. It represents the dynamic formulation of the linear force law.

The representation of the same relationship for the deformation components obtain a complex combination of σ and μ . This can be summarized in the following formulas

$$E = \frac{\mu(3\delta+2\mu)}{\delta+\mu} \quad (5)$$

$$\sigma = \frac{\delta}{2(\delta + \mu)}$$

$$\frac{E}{2\mu} = 1 + \sigma$$

E is modulus of elasticity, called also Young's modulus or expansion modulus. σ is the Poisson's transverse contraction coefficient and μ is called shear or shear modulus. This formula group (2) describes a static state of the volume elements of the medium. This state, however, was achieved dynamically by inserting the impressed forces at the mass points m of the medium of the macroscopic density ρ , initiating their movement and after then terminating it. The formal mathematical transfer of the static problem to a dynamic and vice versa is done with the help of d'Alembert's principle. It links the medium deformation state with the externally imprinted

forces, the inherent inertial forces and the medium-specific material constants. It represents the dynamic formulation of the linear force law.

$$c = \sqrt{\frac{\delta + 2\mu}{\rho}} \quad (6)$$

The validity of two elastic coefficients does not depend so much on the isotropic but rather on the solid state of a substance. In a fluid medium, no process can be generated which can be described by the shear modulus μ . The completely free displacement of the molecules against each other prevents this. For liquids and gases, the shear modulus μ should be deleted. Sound propagates in the fluid body or biological tissue undulating and is transmitted through the interaction of the particles or molecules with each other conform to the well know Huygens–Fresnel principle. The sound wave spreads itself longitudinally in all fluid or gaseous bodies. Normally the longitudinal speed of sound c depends on the elastic coupling of the particles/molecules and is derived with δ as the Lamé parameter and the ρ as the density. The speed of sound c can be described with the formula

$$c = \sqrt{\frac{\delta}{\rho}} = \sqrt{V \cdot \frac{dp}{dV \cdot m}} = V \cdot \sqrt{\frac{dp}{dV \cdot m}} \quad (7)$$

The Lamé parameter δ , is also called the compression modulus (K) or volume elasticity modulus, results for a fluid as well as the biological tissues under the deformation pressure p , whose shear modulus $\mu=0$. This is to extract from the first three equations according to the general Hook law. What gives

$$p = \sigma(x_x + y_y + z_z)$$

By definition, the three summands of the bracket are the relative changes in length of the pressurized volume element. Their sum gives the relative volume change, or the relative density changed $\Delta\rho/\rho$ in the volume

$$\frac{\Delta\rho}{\rho} = x_x + y_y + z_z$$

This gives us the Lamé parameter

$$\delta = \frac{p \cdot \rho}{\Delta\rho}$$

The Lamé parameters δ or as equivalent, compression module K , can be transfer into pressure change dp divided by the volume V changes dV . The same can be done with the density ρ as an equation of the mass m and the volume V (see the equation 1) [6]. When we count only the differential pressures dp so we will expect only infinitesimal changes $d\rho$, so that

$$\delta = \rho \cdot \frac{dp}{d\rho}$$

This provides a following new formula on the sound velocity in a liquid or gaseous media

$$c^2 = \frac{dp}{d\rho} \quad (8)$$

The speed of sound, which generally has the value of the phase velocity, is direct the traveled distance d by the associated time t

$$c = \frac{d}{t}$$

The distances d means, the points between two similar phases φ and this distance is called wavelength λ . The associated time is the period T . The number of periods in the time unit of 1 sec is given by the frequency f .

$$c = \lambda \cdot f$$

Expression (8) with constant c is quite general and valid in any fluid medium under the assumption of the linear law of force. The environment pressure and temperature must be kept constant of course. However, the relationship between the longitudinal speed of sound and these two state variables, must be calculate as the thermal differential quotient equation. The acoustic processes are so fast, that they do not have to be treated as isothermal but as adiabatic processes. First Laplace calculated the differential quotient of the adiabatic equation characterized by the specific heats χ and then obtained the true value of the speed of sound in air

$$p \cdot V^\chi = const$$

now comes, according to Schaaffs [2], the dominant expression of molecular acoustics

$$c_{ad}^2 = \left(\frac{\partial p}{\partial \rho} \right)_s \quad (9)$$

The index S in Eq. (9) indicates, that an adiabatic process is characterized by constant entropy S. If ultrasonic waves were interpreted as isothermal processes, c would be an invariable constant at a given temperature from the frequency $f = 0.0\text{Hz}$ up to the highest conceivable frequencies, what is not the case in the real world.

By introducing the density ρ of a substance as a quotient of molecular weight M and molar volume V in the formula (9), we obtain

$$c_{ad}^2 = -\frac{v^2}{M} \left(\frac{\partial p}{\partial V} \right)_S = -\chi \frac{v^2}{M} \left(\frac{\partial p}{\partial V} \right)_T \quad (10)$$

There is another much-used appearing for this equation, in the form of using the adiabatic compressibility β_{ad} definition. Then for the speed of sound we have

$$c_{ad}^2 = \frac{1}{\rho \beta_{ad}}$$

Analogously, we can calculate a formula for the isothermal compressibility β_{is} . It is defined, in an analogous manner, by

$$\beta_{is} = -\frac{1}{V} \left(\frac{\partial V}{\partial p} \right)_T$$

so that the isothermal velocity of sound is

$$c_{is}^2 = \frac{1}{\rho \beta_{is}}$$

as well as

$$c_{is}^2 = \left(\frac{\partial p}{\partial \rho} \right)_T \quad (11)$$

in the given ultrasound field is the isothermal velocity of sound only an operand. Thermodynamics teaches, that the isothermal processes differ from the adiabatic ones by the ratio χ of the molar heats at constant pressure p and at constant volume V according to

$$\chi = \frac{C_p}{C_v}$$

It can therefore be expected, that this ratio also determines the difference between the two sound velocities. We consider the volume element (fig.1) of a fluid medium and use a following thermal equation

$$f(p, \rho, T) = 0$$

For this purpose, all electrical and magnetic variables are excluded. Also, volume elements with surface effects should not be considered as well. The internal energy E of the fluid medium is an unambiguous puncture of the state variables p , ρ and T . Since these state variables are linked together, the internal energy can be represented as a function of its three internal combinations: (ρ, T) , (p, T) or (p, ρ) . Formulas (9) and (11) require the use of the third combination (p, ρ) . This combination is almost never used, as a glance at the usual depictions of the inner energy in the textbooks on thermodynamics and physical chemistry shows. For the molecular acoustics point of view however, it is precisely the representation of the internal energy E as a function of (p, ρ) that makes it very important. A change dE of the internal energy E is then to be taken as the following differential equation

$$dE = \left(\frac{\partial E}{\partial p}\right)_{\rho} dp + \left(\frac{\partial E}{\partial \rho}\right)_{p} d\rho$$

when molar heat quantity δQ is supplied to the medium and a volume compression δA , against the external pressure p is performed, we have

$$dE = \delta Q - \delta A = \delta Q - p dV$$

the density ρ is still defined as M/V , then

$$dE = \delta Q + p \frac{M}{\rho^2} d\rho$$

Since the speed of sound, that is measured belongs to an adiabatic process where $\delta Q=0$ then follows

$$\left(\frac{\partial p}{\partial \rho}\right)_s \triangleq \left(\frac{dp}{d\rho}\right) = \frac{p \frac{M}{\rho^2} - \left(\frac{\partial E}{\partial \rho}\right)_p}{\left(\frac{\partial E}{\partial p}\right)_{\rho}}$$

When $dp=0$ and $C_V = \left(\frac{\partial Q}{\partial T}\right)_V = \left(\frac{\partial E}{\partial T}\right)_V$ is, then $\left(\frac{\partial E}{\partial p}\right)_{\rho} = C_V \left(\frac{\partial T}{\partial p}\right)_{\rho}$. This works analog with $dp=0$ and $C_p = \left(\frac{\partial Q}{\partial T}\right)_p = \left(\frac{\partial i}{\partial T}\right)_p$ is, then $i = E + pV$ is well known as enthalpy.

Then follows $\left(\frac{\partial E}{\partial \rho}\right)_p = C_p \left(\frac{\partial T}{\partial \rho}\right)_p + \frac{Mp}{\rho^2}$ what finally results in

$$\left(\frac{\partial p}{\partial \rho}\right)_s = \frac{C_p}{C_V} \left(\frac{\partial p}{\partial \rho}\right)_T$$

and thus, is the sought relationship between the two sound velocities

$$c_{ad}^2 = \chi \cdot c_{is}^2 \quad (12)$$

The relationship between adiabatic and isothermal sound velocity is very simple and means, that the two values differ only by the constant factor $\sqrt{\chi}$. The size χ can be interpreted in the form of the following three quotients:

$$\chi = \frac{C_p}{C_V} = \left(\frac{c_{ad}}{c_{is}}\right)^2 = \frac{\beta_{is}}{\beta_{ad}}$$

After introduction the equations definition for the two molar heats and using the second theorems of thermodynamics [7], as well as introduction of the expansion coefficient by the constant pressure $A = \frac{1}{V} \left(\frac{\partial V}{\partial T}\right)_p$ follows

$$C_p - C_V = -T \frac{\left(\frac{\partial V}{\partial T}\right)_p^2}{\left(\frac{\partial V}{\partial p}\right)_T}$$

and finally

$$\chi = 1 + \frac{MA^2T}{\rho\beta_{is}C_V}$$

After all, the sound velocity formula takes a following shape.

$$\left(\frac{c_{ad}}{c_{is}}\right)^2 = 1 + \frac{A^2TV}{\beta_{is}C_V}$$

$$c_{ad} = \sqrt{\frac{\rho\beta_{is}C_p + A^2TM\chi}{\rho^2\beta_{is}^2C_p}} \quad (13)$$

This formula is very useful when we are looking for sound velocity anomalies. This is exactly this behaviour of the longitudinal acoustic waves and the reason why we use it for the detecting, even minor alteration in the human brain. It shows how many different parameters force the speed of sound – no governing dominant force can be chosen.

So, some other speed of sound general formula representation $c = \sqrt{\frac{dp}{d\rho}}$ indicates a very close relationship between the speed of sound c and the density of a substance ρ . It can almost be said, that neither c nor ρ alone are suitable for dealing with questions of molecular structure, but only a combination of both. We will later show, that possibly the density changes as the molecules suppress themselves and enters into the molecules space. Additionally, the electrical activities influence the stiffens of the biological tissue (cells and molecules) causing some significant changes in the density and elasticity of the brain tissue. This behavior of the human brain tissue essentially determines the value of the speed of sound. For our future calculation we will use the simple version of this formula as show in Eq.7.

1.3 General characteristics of the brain anatomical and physiological environment.

The anatomical data of the brain are well known. The human brain consists of two hemispheres located in the cranial cavity. The brain has an oval shape with a narrower diameter in the front (frontal) and a wider one in the back. The brain length is about 15-17cm, the largest vertical dimension is on average about 12cm, and the diagonal ca.14cm. The absolute mass of the adult male brain is 1,375g and 1,245g for a woman. Mean density of the brain is given as 1.030g/cm³. In the cranial cavity, next to the brain, there are still 4 ventricles, this system of interconnected cavities is filled with cerebrospinal fluid. The brain has 3 meninges: hard skin (dura mater), arachnoid and soft skin. The chamber system of the brain is relatively large and occupies a volume of about 0.15dm³. The density of cerebrospinal fluid (CSF) filling the system is about 1.006-1.009g/cm³. One of the most important part of this system is a blood. Its amount alternates periodically, between Diastolic and Systolic point of heart beat and is defined as mean arterial pressure (MAP). The human vascular system, and the brain vascular system especially, could be very well described by the vascular input impedance. This thesis is represented by McDonald and Taylor (since 1959). Total peripheral resistance or total peripheral vascular resistance (TPR) - is a medical term used to determine the total resistance of blood flow in the vessels. It is the sum of the individual peripheral resistances. It is defined as the ratio of the blood pressure in the vessel to the velocity of the flowing blood through the vessel, measured at the same time and the same cross-section of the vessel. The peripheral resistance (R) could be calculated from the following formula

$$R = \frac{P}{Q}$$

where (P) is the pressure difference between the beginning and the end of the measuring path and Q is the flow through the vessel. As an example, the total peripheral vessel resistance could be shown to be the human circulatory system. It is the ratio between the average difference in pressure in the aorta about 100mmHg and the pressure in the right atrium about 0,0mmHg as well as the cardiac output about 5L/min, or

$$TPR = \frac{100 \text{ mmHg}}{5 \text{ L/min}} = 20 \text{ mmHg/L/min}$$

Vascular resistance in the pulmonary circulation is about 10 times less than the resistance in the systemic circulation. The unit of flow resistance PRU (Peripheral Resistance Unit) or resistance, is defined as a unit where the driving pressure of 1mmHg is sufficient to pass through the measuring path through the flow, 1mL (millilitre) of blood within 1min and to move per 100g of tissue is (is always converted to 100 gram)

$$1PRU = \frac{1 \text{ mmHg}}{1 \text{ mL/min}}$$

The vascular impedance is mostly presented in a module and phase form as a function of frequency. For the brain a following parameter can be taken. The brain blood circulation or cerebral blood flow (CBF) [8] [9] estimated in milliliters of blood per 100g brain tissue, per minute is usually counted as 50mL/100g/min. However, when the CBF drops below 20mL/100g/min, it is the first signal of blood supply shortage in the brain and the beginning of ischemia. When CBF rapidly increases, we speak about the term hemorrhage. The exact values of when it is a hemorrhage are not yet precisely defined. There are different CBF values for the formation and expansion of a penumbra. It is the area surrounding an ischemic event such as thrombotic or embolic stroke. The penumbra region typically occurs when blood flow drops below 20mL/100g/min. At this point electrical communication between neurons fails to exist. Cells in this region are alive but metabolic pumps are inhibited, oxidative metabolism is reduced but neurons may begin to depolarise again. Areas of the brain generally do not become infarcted until blood flow to the region drops below 10 to 12 mL/100g/min. In a massive ischemic infarct, the values of brain blood supply, in some particular region, is often dropping to less than 8mL/100g/min. At this point, glutamate release becomes unregulated, ion pumps are inhibited and adenosine triphosphate (ATP) synthesis also stops which ultimately leads to the disruption of intracellular processes and neuronal death

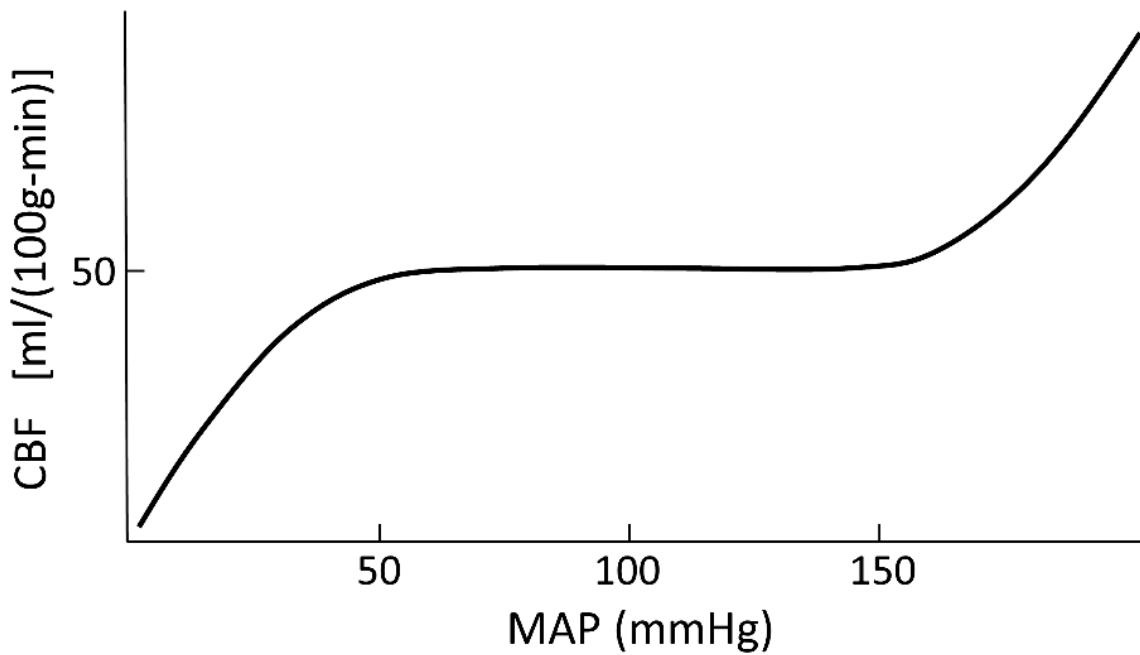


Figure 2: Cerebral blood flow as a function of central blood pressure

Common values for the cerebral perfusion pressure are between 70-100mmHg. Values over 100mmHg are counts as the hyper tensions (HT) and should be taking over medical investigation. The possible pressure changes dP from equation 14 can initially be neglected according to figure 2. The body counteracts them with autoregulation (for example, Bayliss-Effect, para- / sympathetic innervation) and keeps the brain blood flow almost constant within the marked limits [10]. The blood volume, which has a significant influence on density and compression modulus of the brain, will be therefore an important variable for the future diagnostics. Since it is difficult to classify areas of 100 grams of the brain tissue, it is advisable to study the blood flow, not only for specific regions, but for the brain as a whole. For an average brain with the weight of 1,375g, the mean CBF is than something around $\sim 690\text{mL}$ per minute, which gives a value of around $11,6\text{mL}$ per second (estimated as the volume per heartbeat) [11].

Anatomy of the Cerebral Vasculature

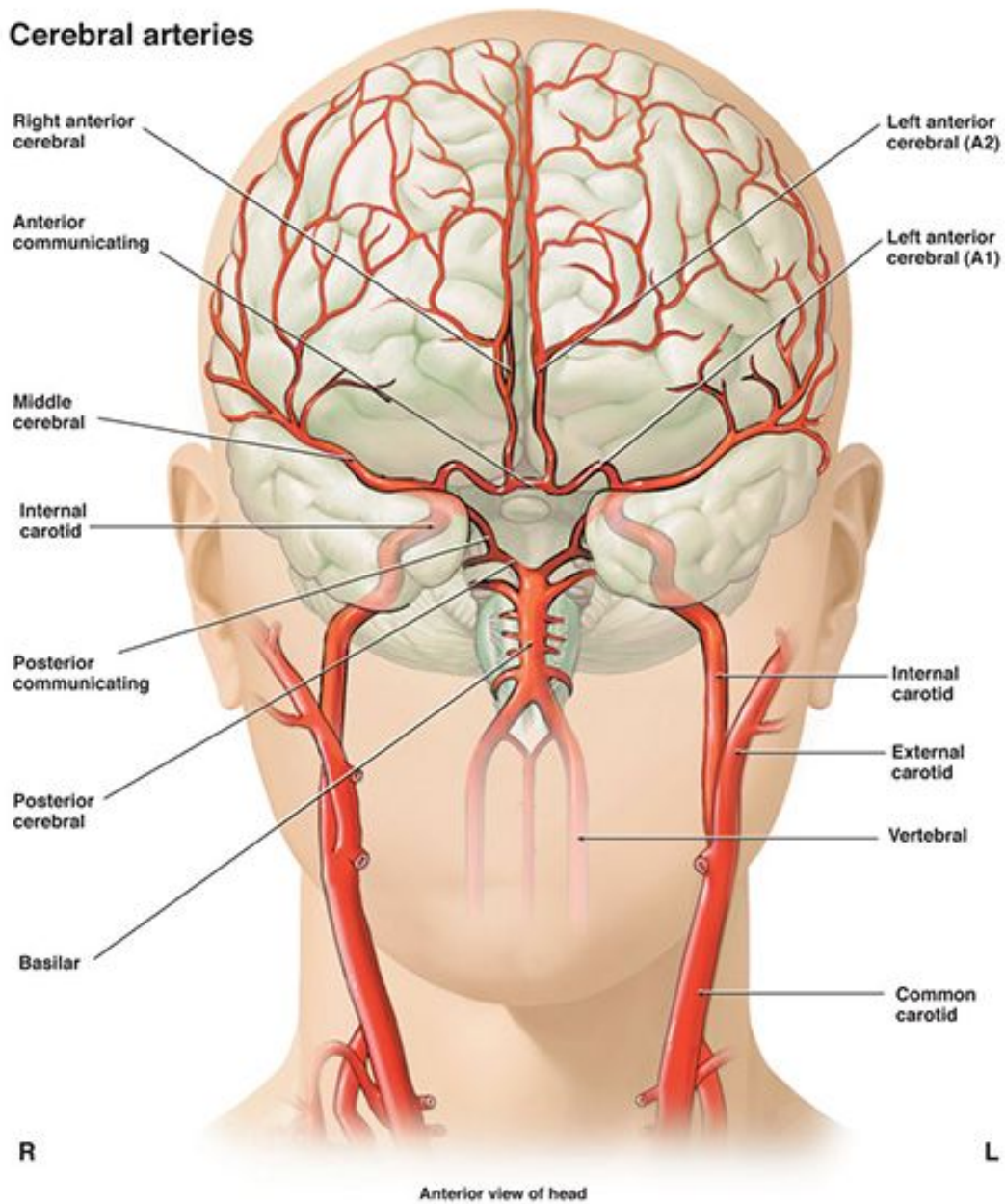


Figure 3: Anatomy of Cerebrovascular system (poster cedars-sinai-edu)

Additional to its biological structure – brain tissue, the brain poses a volumetric volume of 1400cm^3 and a surface area of 2000cm^2 (a ball of the same volume is only 600cm^2 in size). The cerebral cortex covering an average thickness of about 3mm, containing 10^{10} nerve cells and 10^{12} glial cells is essential for the intellectual functions of the brain. The number of connections between cells is estimated at 10^{15} with an average distance of 0.01mm to 1m. The nerve cells

send and receive pulses at frequencies from 1Hz to 100Hz, the duration of the pulse is 1-2ms at a voltage of 100mV. The pulse propagation rate is 1-100m/s. The total speed of the brain can be estimated for 10^{15} synapses * 100Hz = 10^{18} (ca. 1 EOPS) Exa operations per second. Curiously, by the way, it can be stated that the brain is 100,000 times more efficient than a PC considering the consumed energy [12] [13]. To perform a typical reaction, the brain performs no more than 100 elementary steps, this is dictated by the fact, that the measured average response time on a stimulus is less than 300ms. The refraction time of a single neuron is 3ms. This point is very important in the monitoring application. Assuming, that the electrical brain activities influence the brain tissue, e.g. the compression modulus (K) (Eq.7) through the stiffens and the molecular density changing of the brain cell, it means that the ultrasound data acquisition should be about 10 times higher as the brain average response time on a stimulus. This imply, that roughly every 30ms an ultrasound measurement must be conduct, which gives a requirement of approx. 30 measurements per second (MPS) for the designed system.

2 Chapter 2

2.1 General characteristics of the brain anatomical and physiological environment.

The cerebrum is divided in the middle by an incision in two hemispheres. Between these there is a broad compound of a thick nerve cord, also called corpus callosum or bar, and other smaller connections. Beneath the bark the nerve fibres and on the bark, the so-called bark fields are located.

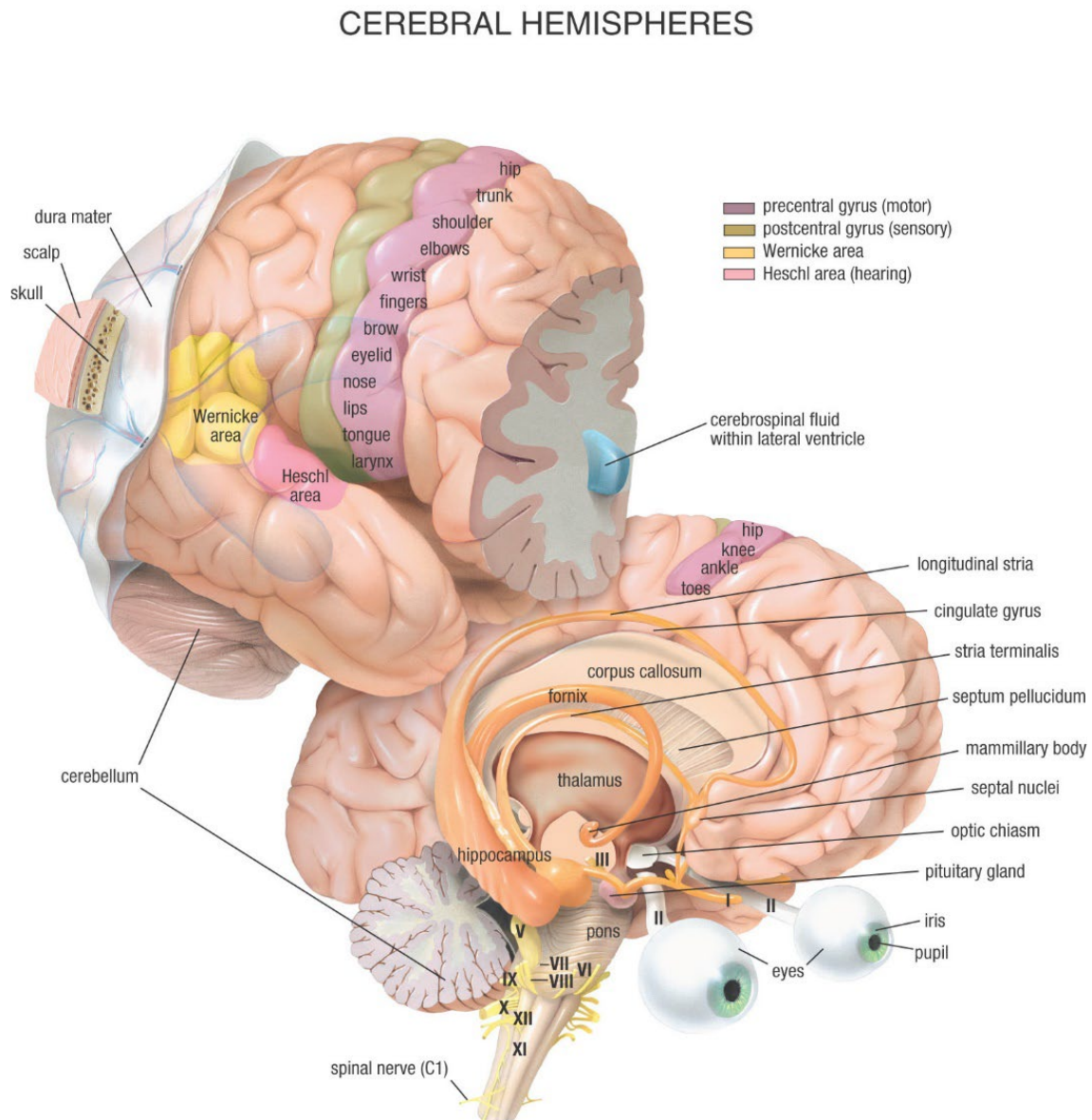


Figure 4: Anatomy of the brain (Anatomical Chart Company, Illinois)

Modern medicine differentiates between primary fields and association fields. The primary fields process only information of a certain quality, namely those about perceptions (sensation, for example, seeing, smelling, touching, etc.) or about simple movements. The association fields match different other functions. The assignment of a cortex field to a certain function is

defined again and then relativized: Only the correct interaction of different fields enables a function. The primary fields include, for example, the visual cortex, which lies at the posterior pole of the brain and on which the projections of the visual path open, and the auditory cortex, which serves to process acoustic stimuli and lies laterally in the temporal lobe. Associative fields can be found in the front part of the brain. Their tasks are, for example, memory and higher thinking processes. The bark fields and their functions can be distinguished from each other by examining the patient's activity after failing (for example, following a stroke) or by examining the healthy brain by electrical stimulation and other techniques. In addition to the cerebral cortex but usually other brain regions are involved in a particular function.

2.2 Brain vascular system

2.2.1 The Arteries

The adult human brain represents approximately 2% of total body weight and yet receives nearly 15% of total resting cardiac output. Under normal conditions, the brain is highly perfused and is very sensitive to any change or interruption in its blood supply. If the circulation to the brain is completely blocked, loss of consciousness occurs within seconds [14] and irreversible pathological changes happen within minutes. For example, in cardiac arrest, the extent of injury of the central nervous system is the critical factor which determines the degree of recovery. It is, therefore, not surprising that the physiological mechanism which regulates cerebral circulation is designed to ensure the maintenance of blood flow to the brain over a very broad range of external and internal conditions. This may even be at the expense of adequate blood supply to the other organs.

The arterial supply to the human brain mainly consists of two pairs of arteries, the right and left internal carotid and the right and left vertebral arteries. The vertebral arteries join to form the basilar artery, which then unites with the two internal carotids to form a complete anastomotic ring at the base of the brain (Fig. 5) known as the Circle of Willis. This ring then gives right to three pairs of arteries, the anterior, middle, and posterior cerebral arteries which cover the external surface of the corresponding regions of the cerebral cortex. These arteries divide into progressively smaller arteries, penetrating the brain tissue and supplying blood to specific regions. Branches of the vertebral and basilar arteries form the blood supply for the cerebellum and the brain stem. Under normal conditions, vertebral-basilar arterial blood is mainly to the tissues in the posterior fossa while the internal carotids supply the remainder of the brain. In addition, there is relatively little bilateral crossing, presumably again due to the similarity in blood pressure. Normally, the Circle of Willis functions primarily as an anterior-posterior shunt than as a side-to-side shunt. However, under pathological conditions, especially those which involve focal obstructions in arterial feeders to the Circle, the balance of pressures may change, and the Circle of Willis can then serve either as an anterior-posterior or as a side-to-side shunt.

- arteries (current direction from the heart)
- arterioles ($Q = 20-100 \mu\text{m}$)
- capillaries ($Q = 5-20 \mu\text{m}$)

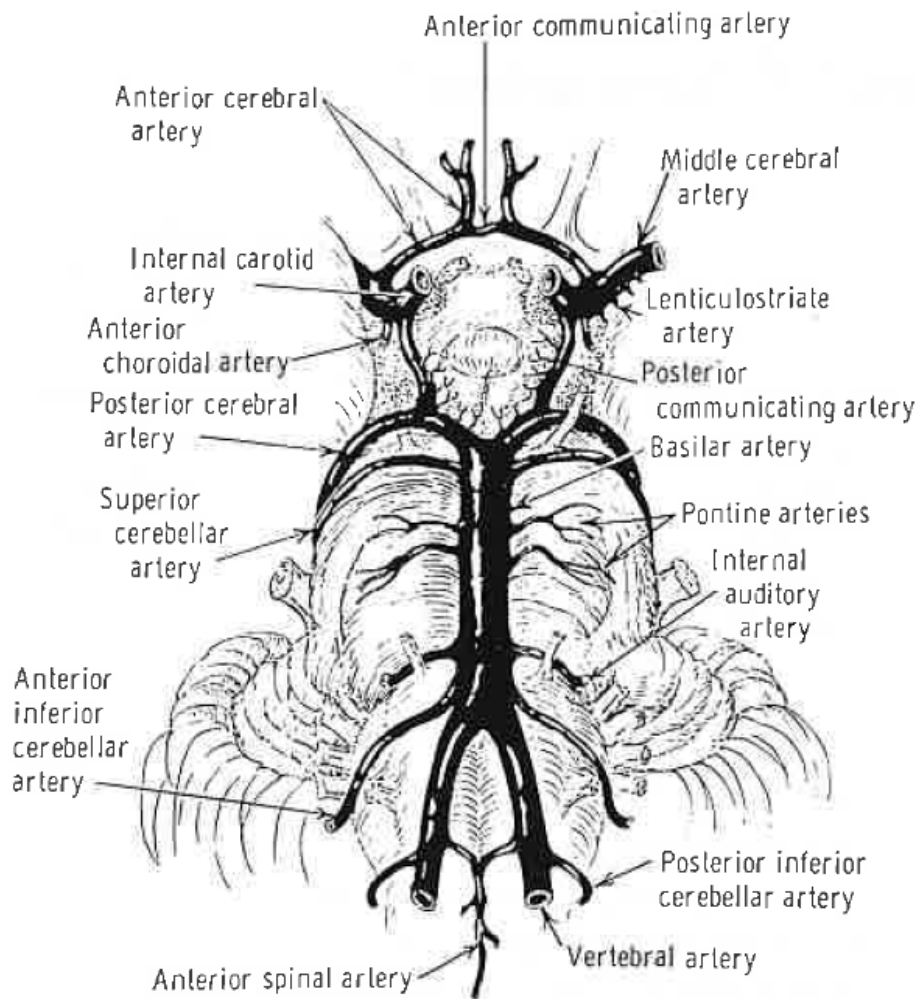


Figure 5: Major cerebral arteries and the Circle of Willis [15]

2.2.2 The Veins

The configuration of the brain venous system is even more complex and provides many opportunities for mixing of blood which drains the various regions (Fig. 6). There are three groups of valveless vessels which allow for the drainage. These are the superficial cortical veins located in the pia mater on the surface of the cortex; the deep or central veins, draining the brain's interior; and the venous sinuses within the dura. While the cerebral cortex is drained mainly by the superficial cortical veins, drainage of the deeper cerebral structures can occur by anastomoses with the deep cerebral veins. The deep cerebral veins traverse the medial and convex surfaces of the brain, emptying into the superior sagittal sinus.

- Two large middle cerebral veins (one on each side of the cortex) start on the lateral surfaces of the hemispheres and run along the lateral fissures. They drain into the sphenoparietal or cavernous sinuses.

- Two deep or central veins, again, one on each side of the cortex, and their tributaries drain the deep regions of the brain.
- The two central cerebral veins run posteriorly and join together to form the great cerebral vein of Galen, then draining into the straight sinus.

Most of the cerebral venous blood eventually drains into the dural sinuses.

- Vein (current direction to the heart).
- Venole (small vein)

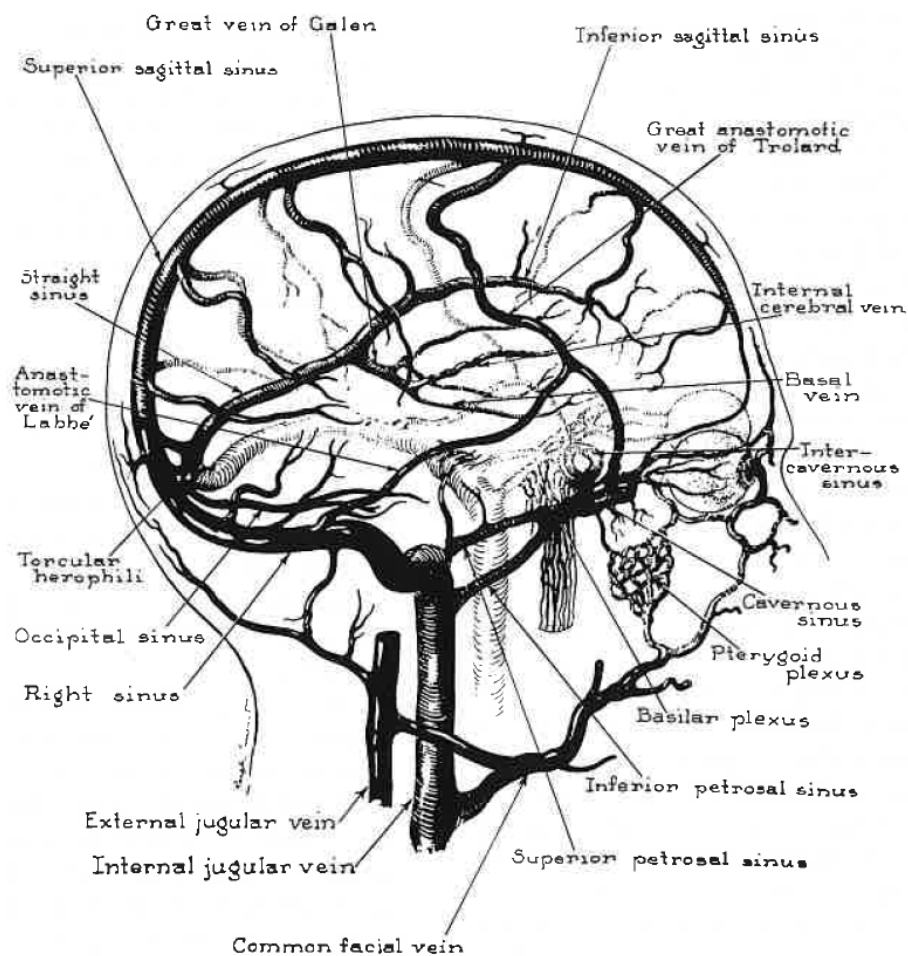


Figure 6: The brain venous system [16]

The construction of the blood vessels corresponds to their physiological tasks and burdens. Depending on the pressure load, they are provided with more or less elastic fibers. Vessels that interfere with the perfusion control have smooth, autonomous muscles that can change their width, cross-section and blood demand accordingly. These muscles are innervated by the autonomic nervous system. A mass transfer in aqueous solution (cell-free blood plasma) takes place through the wall of the capillaries. Blood vessels, except the capillaries, are made up of 3 layers:

- Inner layer (tunica interna or intima), a flat, single-layered epithelium (endothelium), the basal membrane and connective tissue
- middle layer (tunica media or media), a muscle layer corresponding to the myocardium of the heart
- outer layer (tunica externa or adventitia), predominantly connective tissue, corresponding to the epicardium of the heart

A network of over 100 billion capillaries, the total length of which is approximately 600km in an adult, runs through the entire brain. The average distance between these blood vessels is 40 μ m. The various brain regions are supplied differently. The density of capillaries is highest in the cerebral cortex (cerebral cortex) with 300 to 800 capillary cross sections per mm² of brain tissue. The total area of blood vessels in the brain is between 12 and 20m². Approximately 610-690mL of blood flow through these vessels per minute, with an average flow velocity of 1mm/s. The mean blood pressure is in the range of 15 to 35mmHg. The mean transit time (MTT) is 4 to 5 seconds (gray matter: 4s, white matter: 4.8s). In comparison, it lies in the intestine, whose blood vessels have a surface area of 180m², at about 40 hours and in the liver - at 70m² - at 30 seconds. Mean Transit Time (MTT) corresponds to the average time, in seconds, that red blood cells spend within a determinate volume of capillary circulation. It is assessed as part of the CT perfusion protocol which is basically used in the context of ischemic stroke diagnosis and management as well as MRI perfusion which has a broader applicability [17]

2.3 Intracranial pressure ICP

Intracranial pressure (ICP) is the pressure inside the skull and thus in the brain tissue and cerebrospinal fluid. Intracranial pressure is crucial for the brain tissue perfusion and for the brain function at all. It counteracts the pressure with which the blood is pumped into the brain. When intracranial pressure and mean arterial blood pressure are the same, the brain is no longer perfused. Within seconds it will stop functioning and will die within a short time. The ICP was described at first time in 1783, by the Scottish anatomist Alexander Monro, [18] [19]. His hypothesis was:

- (1) the brain is encased in a rigid structure;
- (2) the brain is incompressible;
- (3) the volume of the blood in the cranial cavity must therefore be constant;
- (4) a constant drainage of venous blood is necessary to make room for the arterial supply.

With this knowledge in mind, the English physician George Burrows proposed in 1846 the idea of a reciprocal relationship between the volumes of CSF and blood, that is, an increase in one causes a decrease in the other and introduced CSF as a factor in the Monro-Kellie doctrine [19].

In 1926, Harvey Cushing, American neurosurgeon, formulated the doctrine as we know it today [20], namely, that with an intact skull, the volume of the brain, blood, and CSF is constant. An increase in one component will cause a decrease in one or both of the other components. This relationship provides a compensatory reserve, also called spatial compensation. It is 60–80mL in young persons and 100–140mL in the elderly, mainly due to cerebral atrophy [21]. The volume/pressure curve is shown in fig.7.

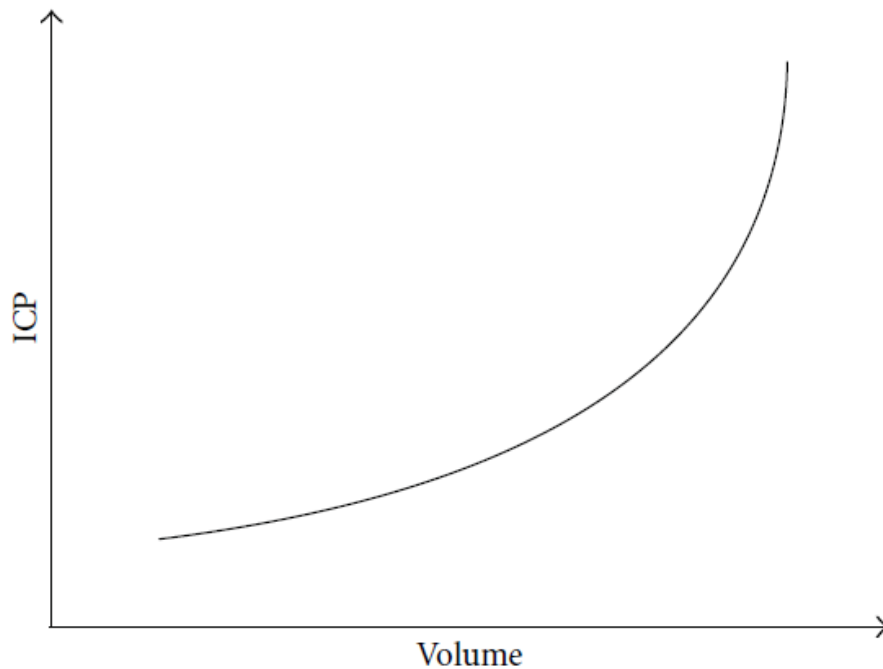


Figure 7: The relationship between intracranial pressure and volume

The first part of the curve is characterised by a very limited increase in pressure due to the compensatory reserve being large enough to accommodate the extra volume. By increasing volume, the compensatory reserve is eventually exceeded, causing a rapid increase in pressure. Normal ICP varies with age and body posture but is generally considered to be 5–15mmHg in healthy supine adults. Under normal physiological conditions, the cerebral autoregulation maintains a constant flow of blood to the brain by dilating or constricting the arterioles. However, this autoregulation is only effective with a mean artery pressure (MAP) between 50 and 150mmHg. Pressure above the upper limit of autoregulation will cause hyperemia and cerebral edema. Pressures below the limit lead to insufficient blood flow and cerebral ischemia, thereby promoting edema formation which is ultimately associated with a poor patient prognosis. In a clinical practice use of ICP monitoring, it is very important to determine the validity of the obtained pressure value. Access to a high-resolution view of the intracranial pressure waveform enables more accurate analysis of the obtained ICP. In performing basic checks of whether the ICP signal is truly representative of the intracranial pressure, the clinician should ensure that there is in fact an oscillating pressure curve with the progressively decreasing P1, P2, and P3 notches present, indicating propagation of the cardiac pulse pressure signal as

in Fig.8. Further information is found in the pulse pressure signal, with reversal of the P1 and P2 notches reflecting a state of disturbed autoregulation [22].

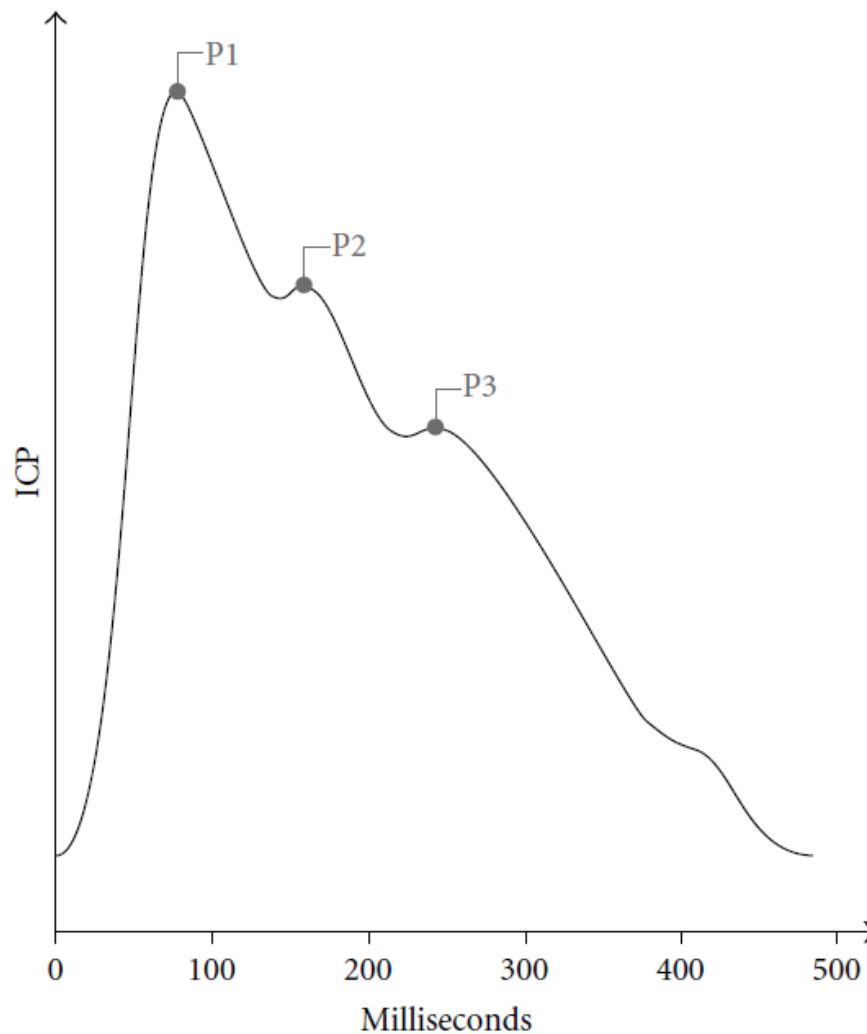


Figure 8: Propagation of the cardiac pulse pressure signal

Increases in intracranial pressure are normally buffered by the displacement of blood and cerebrospinal fluid from the cranium when there is an increase in intracranial volume (ICV). It has been recognized for quite some time, that pressure and flow pulsatility can change with disease; this has been used as a diagnostic tool in a number of areas. How much pressure increases with an increase in ICV is expressed in the calculation of cranial compliance, which can fully describe the pressure-volume curve (see fig.7), it is a very important concept. The compliance (C), is the ratio of volume (V) change to pressure (P) change, $C = \Delta V / \Delta P$ or directly (DICV/DP), where DP is change in pressure and (DP/DICV) is change elastance [23]. In a high compliance system, a large increase in volume will only result in a small increase in pressure. Data reported here indicate that the movement of the cranial bones at their sutures is an additional factor defining total cranial compliance. Although it has been shown that the cranium contains brain tissue and a volume of blood as different compartments, an early concept, the

Monro-Kellie hypothesis, considered the skull to be rigid and proposed that the cranium contained a constant volume of blood. This view had to be modified when the dynamic interactions of intracranial CSF and blood volumes were recognized and more precisely described. Volume and pressure relationships for the contents of the skull are commonly evaluated by the measurement of its hydraulic compliance (the ratio between an instantaneous change in intracranial volume and a corresponding change in intracranial pressure) or its elastance (the reciprocal of compliance). Many data show that intracranial pressure increases nonlinearly with increases in intracranial volume, as described by the pressure-volume index [24].

2.4 Cerebrospinal fluid CSF

The liquor cerebrospinalis or cerebrospinal fluid (CSF) [25], is commonly called cerebral water. The cerebro-spinal fluid, or nerve water, is a normally a clear and colourless bodily fluid that is associated with the tissue fluid of the brain. The cerebrospinal fluid is formed by specially differentiated epithelial cells of the plexuses of the cerebral chambers. Normal CSF is clear like water, colourless and contains only a very few cells. Most of them are lymphocytes (up to 3 per μl CSF) and in rare cases also monocytes. The protein content of the liquor, at about 0.15 to 0.45 grams per liter of liquor, is well below the average protein content of the serum (75 grams per liter). This feature can be used to diagnose CSF disruption by using parallel albumin measurement in CSF and serum. The normal sugar content is 50 to 70 percent of the serum blood glucose value. The CSF pressure, reclined, using the “riser principle” measurement by means of lumbar puncture on the cross is physiologically typical by 70 to 220mmH₂O (= about 690-2160Pa) and fluctuates rhythmically by up to 20mmH₂O (about 200Pa), depending on heartbeat, respiratory type (pressed or relaxed) and the type of lying [26]. A reduced pressure is called hypoliquorrhoea (1 mmHg = 13.595060494664 mmH₂O).

Creation of liquor: Adult people have about 120 to 200mL of CSF according to the volume of the CSF space. These are formed largely in the ventricles of the specifically differentiated epithelial cells of the choroid plexus at a rate of about 0.3 to 0.4mL per minute, mainly by an ultrafiltration of the blood. About 500 to 700mL of CSF are produced per day.

Liquor resorption: Since about 500-700mL of CSF are formed daily, it must be resorbed again, otherwise the intracranial pressure would increase continuously and a hydrocephalus ("water head") would arise. The liquor passes from the lateral ventricles via the interventricular foramen to the third ventricle, then via the aqueduct to the fourth ventricle and from there to the central canal of the spinal cord and via the lateral openings (Foramina Luschkae) and the lower opening (Foramen Magendii) into the outer CSF space corresponding to the subarachnoid space. The resorption is caused by protuberances of the arachnoid which protrude into the venous blood vessels of the dura mater in the skull and are called arachnoid villi (Pacchioni granulations, Granulationes arachnoideae). Similarly, in the root pockets that surround the spinal nerve roots, there are small protuberances through which the cerebrospinal fluid is filtered into veins. In the area of the root pockets the arachnoidian changes into the perineurium. Through this

connection, a few millilitres of the cerebrospinal fluid and spinal nerves per hour flow to the periphery where it is absorbed by the lymphatic system. The purely physical functions of the liquor consist in the neutralisation of gravity and blood pressure, linked to the heart beat cycles, (avoidance of pressure damage by floating in liquid) and padding of the brain and spinal cord. Possible nutritional functions and involvement in signaling cascades are the subject of research [27] [28].

3 Chapter 3

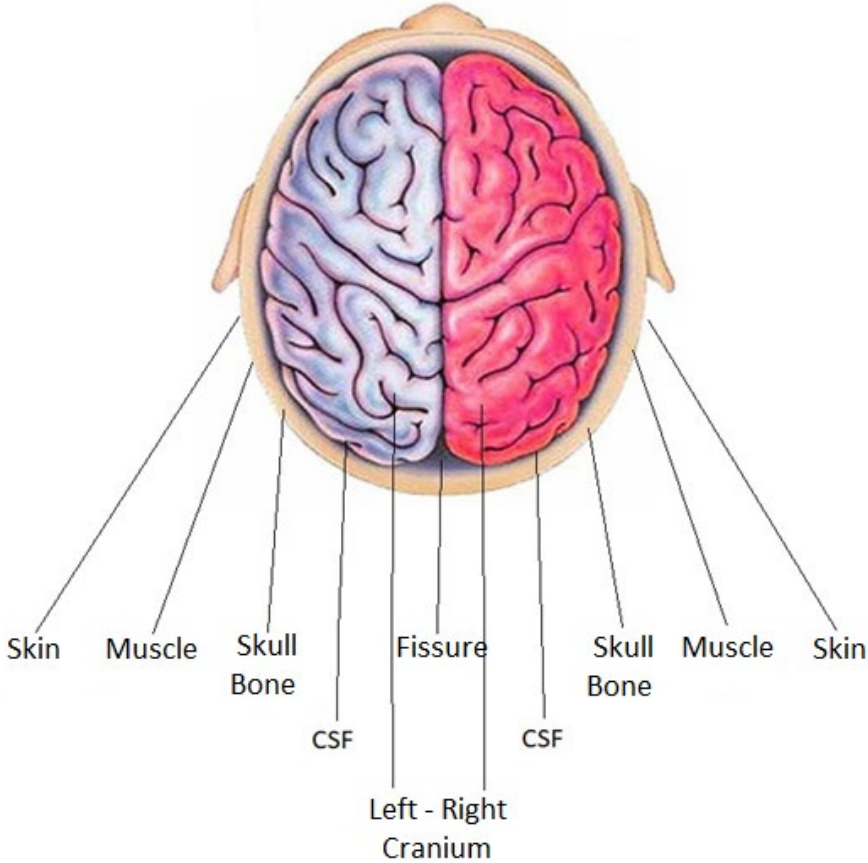
3.1 The basics configuration of ACG measurement

Within cases of cerebrovascular diseases, the under-perfusion is with more than 80% the main cause of sudden onset of death. Parenchymal cerebral hemorrhages, subarachnoid haemorrhages and venous and sinus thrombosis make up the remaining percentages [29]. The surveillance of extracranial neck vessels in the shape of the A.Carotis and A.Vertebrae using artery duplex ultrasound is already an accepted diagnostic technique that can provide valuable information on calcification and associated blood turbulence or shortfall. Unfortunately, the thickness of the skull and the associated attenuation of the sound prevented a similarly detailed imaging examination of the intracranial vessels [30]. Ultrasound imaging technique is already an important and proven tool for diagnosis and therapy in medicine but these systems, based on Pulse-Echo method, return only information about the internal structure of a target as a 2D or 3D picture, but not about object's composition. The Acousto-Cerebro-Graphy concept, or ACG for short, follows another possible ultrasound application. This work demonstrates that using multiple frequencies, the dispersive character of the brain tissue will be shown and provide some interpretation of the signal changes. Dispersion is an effect in which the non-linear, frequency dependent compression modulus of the medium, results in different propagation speeds for different sound frequencies. In non-linear material, as for example biological tissue and especially human brain tissue, an effect of longitudinal wave dispersion can be clearly observed and measured. It is the effect, in which the non-linear frequency-dependent mediums compression modulus result in different propagation speeds for different ultrasound frequencies. Since the properties of the compression modulus depend on the specific characteristics of the medium, such as density, composition, mixture concentration, distribution and in some situations chemical composition, the pattern of frequency dependent propagation speeds can be used to identify the medium. In other words, it can be seen in (Eq.13) and (Eq.14) that the propagation speed $c(f)$ is a function of frequency or the wave length. It depends on compression or elasticity modulus K_v for liquid media and the bulk modulus K_B for solid media.

$$c = \sqrt{\frac{K}{\rho}} = \sqrt{V \cdot \frac{dp}{dV \cdot \frac{m}{V}}} = V \cdot \sqrt{\frac{dp}{dV \cdot m}}$$
$$c_{ad}(f) = \sqrt{\frac{K(f)}{\rho \cdot \beta_{ad}}} \quad (14)$$

The compression modulus K can be split into the volume V , the volume change dV and the associated pressure change dp . In analogy to this, the given density ρ , can be split in mass m and the volume. In order to apply this formula beneficially to the human body, first of all, the structure of the human head must be considered. In fig.9 it is roughly shown. Skin, muscle,

skull bones and cerebrospinal fluid, in some kind, can be neglected in their effects on the ultrasound and can therefore be regarded as constants. The next part is the left and right cerebrum as well as the longitudinal cerebral fissure. However, these parts of the brain, including also the part of CSF, depend very strongly on the cardiac cycle and the blood circulation in the brain tissue, as was previously shown. This zone is therefore the “Point of Interest” for the investigation.



No.	tissue structure	size	impact on thy tissue changes
1	Skin + Muscle	approx. 2,5mm	No
2	Skull bone	approx. 2.5mm	No
3	CSF	approx. 25 mm*	Partially - Yes
4	Cranium	approx. 67-69mm	Yes
5	Cerebral fissure	approx. 1.5mm	No

Figure 9: Layers model of the human head (*with ventricles)

The data should be gathered with the time of flight method. If we have a set of tissue layers L, then the total propagation time is obtained by adding up the propagation time for each tissue in the set

$$t(f) = \sum_{i \in L} t_i(f)$$

The model can be conveniently upgraded or modified. For example, at the user's discretion, the model can be supplemented with additional tissue layers. In addition, if precise and detailed dispersion data are available, the dispersion for a given tissue can be modeled as a non-linear function of frequency. For a given tissue i , the propagation time for frequency f , $t_i(f)$, can be calculated according to the relation

$$t_i(f) = \frac{d_i}{c_i(f)} = \frac{d_i}{c_{0i} + (f - f_{0i})\Delta_i}$$

where d_i is the depth of the tissue traversed by the acoustic wave, c_{0i} is the base speed defined at a base frequency f_{0i} , and Δ_i is the tissue's dispersion trend, which characterises the frequency dependence of the propagation speed [31]. The signal is transmitted by an ultrasound probe and recorded either by another (transmission) or by the same (reflection). The speed of a transmitted signal depends on the medium, as already described. Based on the anatomical analyses of the human skull-brain-system it can be demonstrated that depending on the region, there are very diverse conditions for the propagation of acoustic waves. Taking into account the previously addressed points, to optimize the direction of the tissue examination, the frontal plane (coronal) direction fig.10, should be chosen for transmission or reflecting measurements. Limitations related to the minimization of ultrasonic waves' intensity has induced the search for such areas in the cranial system which are characterised by the smallest acoustic wave suppression. The analysis shows that the most suitable areas for the implementation of this measurement method are the surfaces located slightly above the outer ear channel, please see fig.11. The choosing of such measuring direction means, with the greatest probability, we can get a full echo from the opposite skull bone. Based on the analyses above, a simplified a layered structure of the cranial system can be adopted.

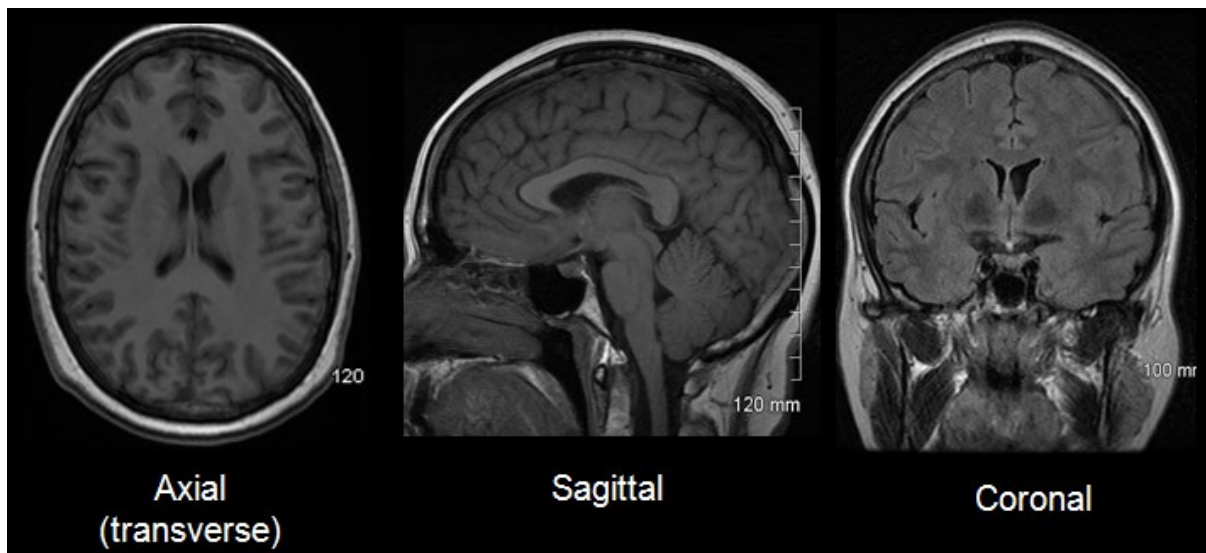


Figure 10: Imaging plane of the human head

By adopting the aforementioned layer model of the human cranium as an input - together with the physical values of the different cranial tissues, see table 1 - the propagation times of the acoustic signal as well as the signal attenuation along the flight path through these structures can be determined, see table 2. Considering a transmission method, the measurement process involves the “insertion” of an acoustic wave to the central cerebral system at the selected location and the subsequent reception in the opposite position according to the direction of the acoustic beam propagation. This method requires the use of two ultrasonic probes – one for transmitting and one for receiving of the acoustic signal [32] [33] [34] [35].

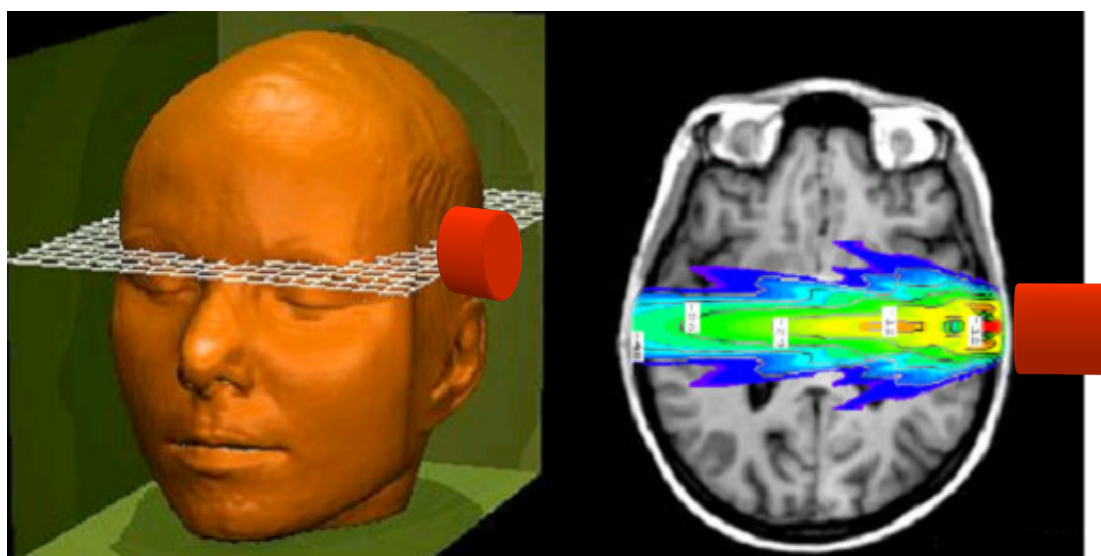


Figure 11: Axial (transversal) plane view of the brain (ultrasound probe position) with possible acoustical field coverage

The basic parameters of the human skull-brain model

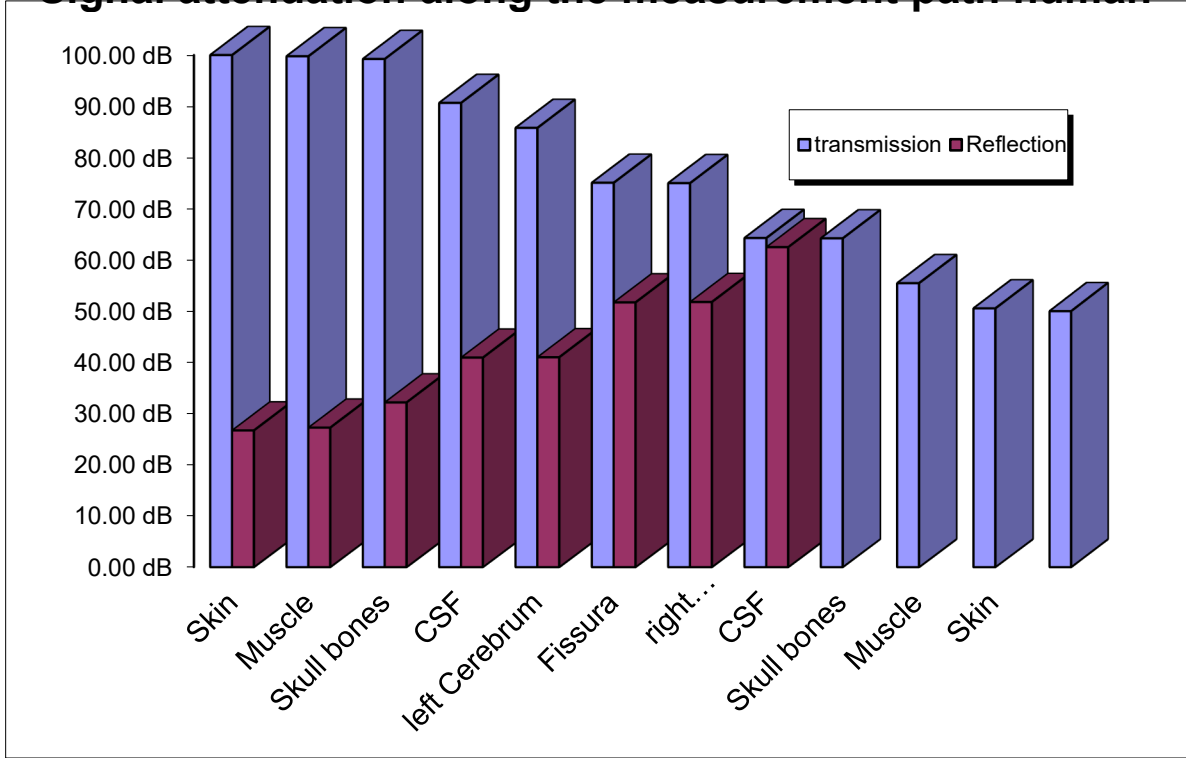
	Density ρ kg/m ³	c in m/s	Z in kg/(m ² *s)	attn. coefficient in dB/(cm*MHz)	
				1MHz /	10MHz
Cerebrum tissue	1030	1515	1560450,000	1	8
Skull bones	1900	4080	7752000,000	10	60
CSF	1007,5	1498	1509235,000	0,003	0,22
Water	997	1483	1478551,000	0,003	0,22
Blood	1057	1580	1670060,000	0,2	3,8
Skin + Fat	930	1480	1376400,000	1,5	
Muscle	1002	1580	1583160,000	0,7	

Table 1: The basic parameters assumptions for the human skull-brain model [34]

As already described in Chapter 1.3, “General characteristics of the brain anatomical and physiological environment”, the cerebrovascular system is very complex and therefore the state of the brain blood supply is very dependent on its physical and chemical parameters. The internal pressure depends on intracranial fluid and tissue volumes and the pulsatile volumes induced by the arterial blood pulsation within the skull [36]. By knowing normal brain blood circulation or cerebral blood flow (CBF) e.g. of 50mL/100g/min, we will have for an average brain weight of 1,375g, the mean CBF something around ~ 690mL per minute, this gives a value of blood around 11,6mL per second (estimated as the volume per heartbeat).

To conform with Chapter 2.3 “Intracranial pressure ICP”, the forces applied either internally or externally to the skull cause lateral and rotational movements of the parietal bones around the sagittal suture that joins them [37] [38] as well as with the knowledge, that expansion and contraction of the skull are generated through changes in internal pressure and are counterbalanced by the stiffness of the surrounding skull, we can try to calculate ToF and the speed of sound changes based on a standard cranial tissue perfusion CBF.

Signal attenuation along the measurement path human



	Skin	Muscle	Skull bones	CSF	Left Cerebrum	Fissure	right Cerebrum	CSF	Skull bones	Muscle	Skin	Total:
Time	0,533	1,251	0,613	6,476	42,384	1,669	42,384	6,476	0,613	1,251	0,533	104,183 μ s

Table 2: Human head model of the ultrasonic signal attenuation and expected time of flight along the measurement path [34]

An intracranial pulsation measurement, acquired from normal volunteers, demonstrate detectable bone movements on the order of several microns – up to 20 μ m during the bed rest [39].

$$c_{path}^2 = \frac{(K_{norm}(1-x) + K_{path} \cdot x)}{(\rho_{norm}(1-x) + \rho_{path} \cdot x)} \quad (15)$$

Let's take a very simplified model. A standard CBF with 50mL/100g/min means, that with every heart rate e.g. 60 beats per minute (bpm), between diastole and systole approx. 8% to 10% of the mass will be exchange.

$$\frac{CBF}{bpm} \cdot \rho_{blood} \Rightarrow \frac{50mL}{60 bpm} \cdot 1.057g/cm^3 = 0.88g$$

Farther, using the Eq.15 we can try to estimate the acoustic wave speed changing. When we assume that approx.10% of CSF are periodically exchange with the blood according to the normal perfusion values, we can try to calculate the acoustical wave's time of flight changes.

The corresponding K values of CSF and Blood can be calculated from the known c and ρ according to the Eq.7.

$$K_{CSF} = c_{CSF}^2 \cdot \rho_{CSF} = 1498^2 \cdot 1007.5 = 2.2608 \cdot 10^9 [Pa]$$

$$K_{Blood} = c_{Blood}^2 \cdot \rho_{Blood} = 1580^2 \cdot 1057 = 2.6386 \cdot 10^9 [Pa]$$

$$c_{sys}^2 = \frac{(K_{CSF}(1-x) + K_{Blood} \cdot x)}{(\rho_{CSF}(1-x) + \rho_{Blood} \cdot x)}$$

$$c_{sys} = \sqrt{\frac{(2.2608 \cdot (1-0.1) + 2.6386 \cdot 0.1) \cdot 10^9}{(1007.5 \cdot (1-0.1) + 1057 \cdot 0.1)}} = 1506.7563 \left[\frac{m}{s} \right] \quad (16)$$

When we take the CSF area as 1 cm overall (this is the area where the brain tissue expansion due to the pulsation take place we will have according to the Eq.8 and the following explanation: Diastolic travel time is:

$$t_{dia} = \frac{l}{c_{CSF}} = \frac{0.01}{1498} = 6.67556 \mu s$$

conform with the Eq.16 and adding the overall skull expansion of 20 μ m for the systolic moment the ToF for the pulsating region is [23]

$$t_{sys} = \frac{l}{c_{sys}} = \frac{0.0102}{1506.75} = 6.76953 \mu s$$

This shows that even when the speed of sound increases due to CSF v. Blood exchange for the particular region of interest for more than 8,75m/s of the overall acoustic package travel time increase as well due to the longer path. When we now subtract from t_{dia} , the time changes caused by the systolic blood perfusion and the tissue expansion t_{sys} we get:

$$t_{dia} - t_{sys} = |6.67556 \mu s - 6.76953 \mu s| = 0.09396 \mu s \text{ or } 93.96 ns$$

We must achieve a simple definition of this benchmark with our system if we want to use it for medical diagnostics. Time around $\pm 45 ns$ should be measured with the adequate resolution, means better then 100 times (around 400ps step) and faster then 30 measurements per second. At the same time, we have to notice that the traveling time difference (increasing/decreasing) can reduce when the skull expansion will reduce or even sweep to negative when the skull will not expand due to increase ICP. This can be a very useful information for emergency medical aid personal, where the development of increased intracranial pressure (ICP) is a major

complication of many cerebral diseases and has a significant impact on morbidity and mortality, as well as further prognosis. Data from the UK show that 18% of all patients with Severe Traumatic Brain Injury (SHT) have permanent functional damage requiring long-term occupational and social rehabilitation. The extent of this damage is determined not only by the primary severity of the trauma but influenced to a significant extent by secondary brain damage. An increased intracranial pressure which has not been recognised in time and adequately treated, has an important pathogenetic significance [40].

3.2 Dispersive Ultrasound as Non-Invasive Diagnostic System

The ACG utilises ultrasound quasi constant wave packages of different frequencies to interrogate a medium in order to provide propagation times for each of the transmitted frequencies. This process provides estimation of the dispersion patterns $c(f)$ for a specific contained medium. The observed changes to the propagation speed are usually very small and require a very precise measurement of the propagation speed. Instead of measuring the speed of sound in the media it is easier to accurately measure the propagation time of ultrasound signals that travel along a known distance from a transmitter T to a receiver R, as depicted in fig.12.

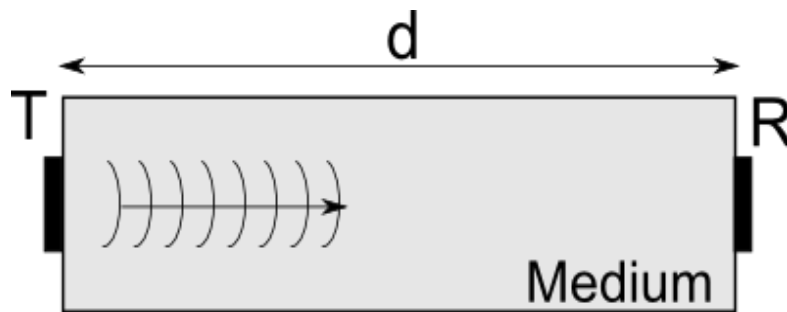


Figure 12: Oversimplified layers model of the human head. Ultrasound signal traveling from transmitter T to receiver R in a Medium with dimension d

As shown by (Eq.17), the propagation speed $c(f)$ can be estimated very precisely from the propagation time $t(f)$ by assuming, that the constant dimension d, is known.

$$c(f) = \frac{d}{t(f)} \quad (17)$$

Using a modern method, a very high sampling frequency for the received signal to accurately measure the propagation time $t(f)$ will be required. To achieve the necessary accuracy, a sampling frequency in the GHz range (exactly 2,5GHz by 400ps resolution) is necessary because the signal travelling from the transmitter to the receiver when the time resolution in the range of sub-Nano second is required. Such a system would be formidably expensive and have unacceptable power requirements for a portable device. Instead, it is well known that an ultrasound signal is not only described by its frequency but also by phase information:

$$g(t) = S + A \sin(\omega t + \varphi) \quad (18)$$

Therefore, to overcome the requirement for a high sampling frequency, the phase information of the ultrasound wave can be used along with its amplitude to provide accurate estimates of propagation times. It is commonly known, that the phase information only covers a range from $-\pi$ to $+\pi$. Hence, it can only be used to get additional information about one period of the signal. Beyond that, this information keeps repeating itself. Using a phenomenon from wave theory called beat-note¹, which is the result of the combination of two continuous wave signals that are close in pitch but yet not identical. The difference in frequency generates the beating. The frequency of the beat-note is given by

$$f_{beat} = f_1 - f_2$$

The closer f_1 and f_2 are, the lower is the resulting frequency beat f_{beat} and the longer is the period of the resulting beat phase $T_{beat} = 1/f_{beat}$. The use of this beat-note approach allows for the unique identification of a certain point in the signal. Once this unique point has been found, the phase information of the individual frequency, in certain situations, can be used to accurately calculate propagation times. In addition to the observed changes in propagation speed, different attenuation profiles can also be observed. Interdependence between wave speed and attenuation is in accordance with Kramers-Kronig relations (19) where it is shown amongst others that

$$\frac{1}{c_2} - \frac{1}{c_1} = -\frac{2}{\pi} \cdot \int_{\omega_1}^{\omega_2} \frac{\alpha(\omega)}{\omega^2} d\omega \quad (19)$$

where c_1, c_2 are propagation velocities (speed of sound) for waves with circular frequencies ω_1 and ω_2 , respectively, and $\alpha(\omega)$ is the attenuation for wave with circular frequency ω . The above, after introducing $\omega = 2\pi f$, $\omega_1 = 2\pi f_1$ and $\omega_2 = 2\pi f_2$, takes the form of:

$$\frac{1}{c_2} - \frac{1}{c_1} = -\frac{1}{\pi^2} \cdot \int_{f_1}^{f_2} \frac{\alpha(f)}{f^2} df \quad (20)$$

As will be presented further in this work, such patterns of frequency-dependent attenuations and the corresponding propagation speeds can be used to identify the state of a medium or to track possible changes to the brain tissue in real time.

In order to achieve the requested time resolution for a useful medical diagnostic picture, as shown on fig.13, some essential requirements on the phase determination have to be made.

¹ In acoustics, a beat is an interference effect between two sounds of slightly different frequencies, perceived as periodic variations in volume whose rate is the difference between the two frequencies.

Supposing, that the interesting acoustic measurement band for ACG is between 0.7MHz and 2.7MHz, this will set a following expectation on the signal phase resolution.

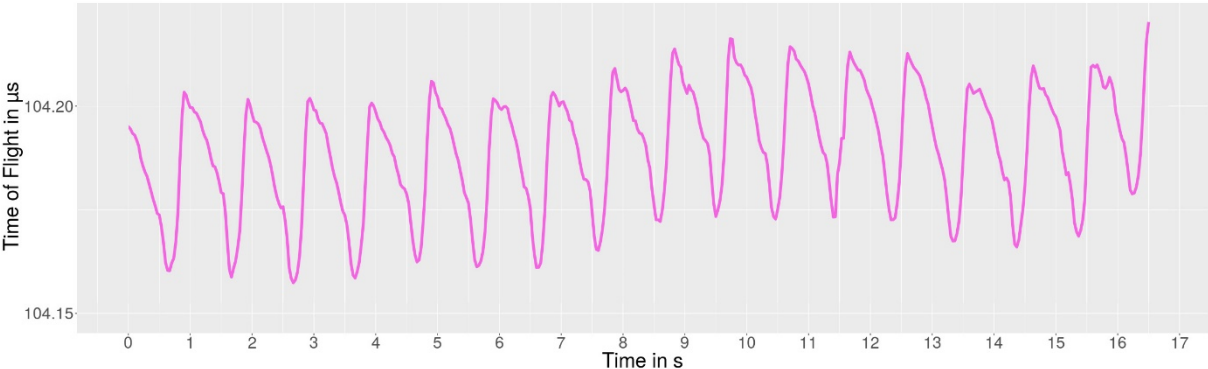


Figure 13: ToF to heartbeat curve of a 72 years old male, taken with ACG system – please take a closer look on the reversal P1 and P2 notches reflecting a state of disturbed autoregulation as described in Ch.2.3 – Intracranial pressure ICP

We need a phase resolution better than 400ps by a frequency of 0.7MHz – each higher frequency will give higher time resolution while the wave length will be shorter – means time resolution will be greater. Just assuming that, the average speed of an acoustic quasi constant wave package in cranium as 1540 m/s, according to the Eq.8 and the following explanation we will get

$$\lambda = \frac{c}{f} = \frac{1540}{0.7e6} = 2.2[mm]$$

This 2.2mm is the length of exactly one period (360° or 2π phase) with the time duration of 1.4285714μs. A simple three pack bill shows, that the required phase resolution needs to be in the range of 0.1° or better.

4 Chapter 4

4.1 Dispersive Ultrasound as Non-Invasive Diagnostic System

When waves propagate through a medium, different frequencies propagate at different speeds. This phenomenon is called dispersion. The propagation times for a set of frequencies are referred to collectively as the dispersion spectrum. The amount of dispersion, and, therefore, the form of the dispersion spectrum, depends upon the physical properties of the medium. As such, dispersion can be used as a finger print of those properties.

In a medical context, ultrasonic waves travelling through biological tissue exhibit dispersion, and, consequently, the resulting dispersion pattern contains information about the properties of the tissue. For this reason, ultrasonic dispersion has the potential for use as a medical diagnostic tool. Unlike most medical diagnostics based on ultrasound, dispersive ultrasound does not attempt to image the tissues. Rather, the tissue characterisation is based simply on the observed dispersion spectrum. The principal medical use envisaged for the ACG is as a diagnostic tool for internal, non-visible injuries of the head, such as mild Traumatic Brain Injury (mTBI) or intracranial hemorrhage or even chronic diseases as white matter hyperintensities (WML). The changes to the intracranial tissues that occur as a result of these injuries are likely to produce changes in the observed dispersion spectrum. This is the key to the diagnostic capabilities of the ACG.

4.2 Phase estimation for dispersive ultrasound

The core innovation for the present ACG method is the signal processing configuration that provides an estimation of the propagation time for signals of different frequencies. This implies that some simple phase estimation techniques must be found and it should be sufficient to provide a necessary phase resolution better than 0.1° . *The phase method* is based on the analysis of the phase relations R between transmitted and received signals for one probing frequency f . *The time method* based on phase method employs in measurement process two suitably selected frequencies which makes it possible to determine the run time of the probing signal T_p . The kernel of both methods is an elementary phase determination procedure. It is possible to determine the signal parameters including the phase value φ using some digital solutions to the problem of n samples approximation by performing an equation of harmonic wave in a general form. Using wave packets and analysis of the phase dependencies R between transmitted and received waves gives solution easy to perform in practice, and moreover it ensures the required higher resolution of time measurements [41].

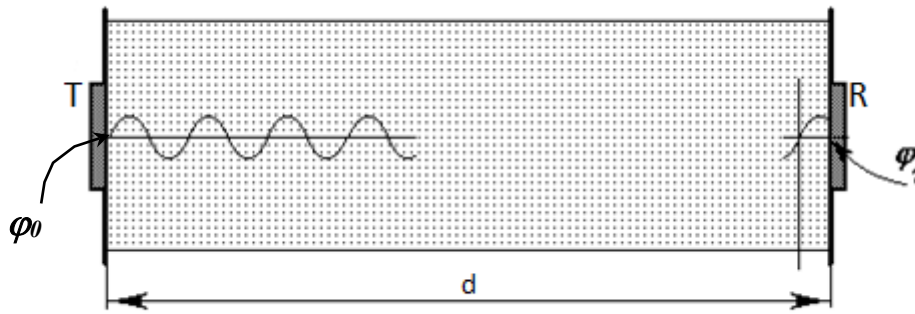


Figure 14: Scheme of a system for measurement of phase relations of acoustic wave packets

Similar to the arrangement shown previously on fig.12, the system consists of a measurement vessel of unknown length d as well as transmitter and receiver of ultrasonic waves. As shown in fig.14 at the given transmitter frequency within a vessel length, a certain number of the oscillation periods P and "a part of period" expressed as phase difference $\varphi_1 - \varphi_0$ will occur.

$$\Phi = 2\pi f T_p = 2\pi f P + (\varphi_1 + \varphi_0) \quad (21)$$

Depending on the specific character of investigations (changes detection in a phase method or parameter determination in a time method) the problem is always reduced to the determination of phase relations $R = \varphi_1 - \varphi_0$ with the lowest experimental error. For the run time measurement T_p , an additional determination of absolute number of the wave length P within the probing distance d is necessary. A very simple method for door-to-door (or lead) time T_p estimation, by using of two different quasi-constant wave packages with two different f_1 and f_2 frequencies, as used by Jodlowski [42] can be taken. A simple diagram of this method can be outline as follow.

$$g(t) = S + A \sin(\omega t + \varphi)$$

Farther by Jodlowski Szustakowski, and Piszczek [43], similarly in typical pulse technique, the measurement consists of the determination of temporal relations between transmitted and received acoustic signals. The measuring process is based on phase analysis of these signals.

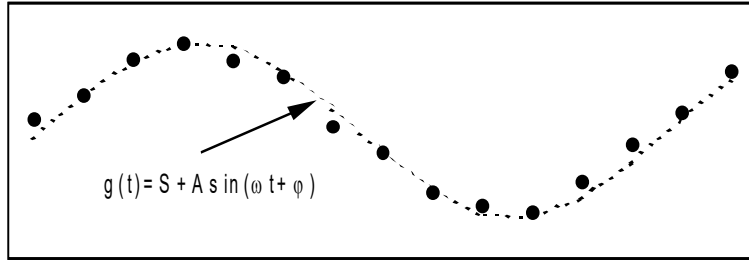


Figure 15: Approximation of sampled signal.

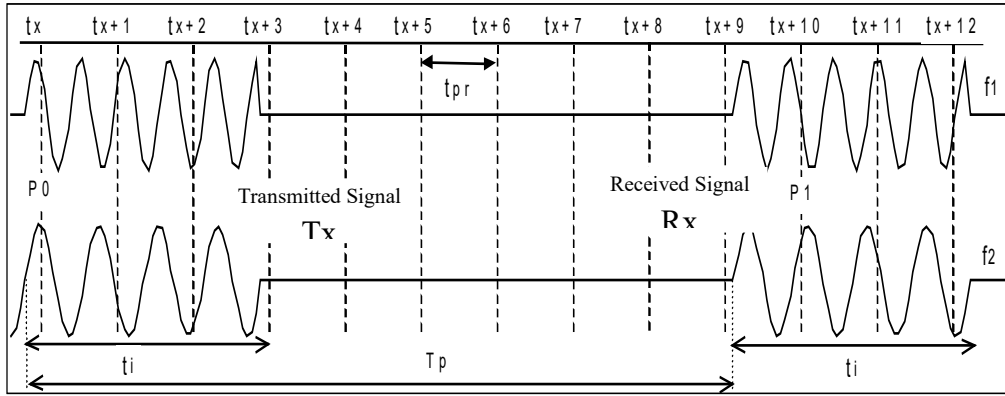


Figure 16: Diagram of time estimation method T_p

The duration of the used wave packets t_i is in strict relation to the signal sampling period t_{pr} and to the frequency for a probing wave. The optimised duration of a wave packets for minimum error of the elementary phase φ_i is described by relationship

$$t_i = (n - 1) \cdot t_{pr} \text{ where } f = \frac{m}{t_{pr} \cdot n} \quad (22)$$

t_x – Signal sampling moments.

P0 (Samples number) – Transmitted signal phase estimation point,

P1 (Samples number) – Received signal phase estimation point,

Primary phase determination

$$D = \frac{(n \cdot y \sin - y \cdot \sin)(\sin \cdot \cos - n \cdot \sin \cos) + (y \cdot \cos - n \cdot y \cos)(\sin^2 - n \cdot \sin \sin)}{(n \cdot \sin \cos - \sin \cdot \cos)(\sin \cdot \cos - n \cdot \sin \cos) + (\cos^2 - n \cdot \cos \cos)(\sin^2 - n \cdot \sin \sin)},$$

$$C = \frac{y \cdot \sin - n \cdot y \sin + n \cdot D \cdot \sin \cos - D \cdot \sin \cdot \cos}{\sin^2 - n \cdot \sin \sin},$$

$$S = \frac{y - C \cdot \sin - D \cdot \cos}{n}, \quad \boxed{\varphi = \arctan \frac{D}{C}}, \quad A = \frac{D}{\sin(\varphi)} = \frac{C}{\cos(\varphi)},$$

C [Sign]	+	-	-	+
D [Sign]	+	+	-	-
φ [Degree]	0-90	90-180	180-270	270-360

$$\text{where: } \sin = \sum_{i=1}^n \sin(\omega t_i), \quad \cos = \sum_{i=1}^n \cos(\omega t_i), \quad y = \sum_{i=1}^n y_i, \quad \sin \cos = \sum_{i=1}^n \sin(\omega t_i) \cos(\omega t_i),$$

$$\cos \cos = \sum_{i=1}^n \cos(\omega t_i) \cos(\omega t_i), \quad \sin \sin = \sum_{i=1}^n \sin(\omega t_i) \sin(\omega t_i), \quad y \sin = \sum_{i=1}^n y_i \sin(\omega t_i),$$

$$y \cos = \sum_{i=1}^n y_i \cos(\omega t_i).$$

When using phase method for a single measurement, there is a possibility to determine the phase relation $R = \varphi(t_1) - \varphi(t_0)$. This value's quantity may change within the range of the round angle $\pm\pi$. It shows that final description of medium properties cannot be made at once. Only a momentary state can be defined as a differential measuring state with no possibility to compare it to the results from various or previous measurements. However, this method is sufficient for media monitoring on the assumption that the phase changes do not exceed the value of $\pm\pi$ in a consecutive measurement (single measuring session).

4.3 Lead time determination T_p

The time method is free of those limitations as given in the previous solution and gives a measurement process the value of passing time of probing signal T_p . The solution has several limitations. Though the conditions that have to be fulfilled are not too excessive, only their strict keeping can bring reliable results. The two-stage measuring procedure makes it possible to determine the rough T_p value with the resolution $\pm t_{pr}$ in a typical way used for pulse methods but the measurement of a precise term of the equation is based on phase analysis for each of the probing frequencies f_1 and f_2 [44].

$$T_p = (t_1 - t_0) + \frac{1}{4\pi} \left(\frac{R_1 + 2\pi P_1}{f_1} + \frac{R_2 + 2\pi P_2}{f_2} \right)$$

$$P_1 = \frac{R_{12} f_1}{2\pi(f_1 - f_2)} - \frac{R_1}{2\pi}; \quad P'_1 = \text{Abs}(P_1) \quad \text{and} \quad P_2 = \frac{R_{12} f_2}{2\pi(f_1 - f_2)} - \frac{R_2}{2\pi}; \quad P'_2 = \text{Abs}(P_2),$$

$$R_1 = \varphi(t_1) - \varphi(t_0) \text{ for } f_1, \quad R_2 = \varphi(t_1) - \varphi(t_0) \text{ for } f_2, \quad R_{12} = R_1 - R_2$$

where: $R_1 = \varphi(t_1) - \varphi(t_0)$, f_1 and $R_2 = \varphi(t_1) - \varphi(t_0)$, f_2

$$R_{12} = R_1 - R_2$$

Abs – means absolute rounded to the next integer value

The first condition that must be fulfilled concerns an acceptable divergence between rough value of acoustic signal run time $(t_1 - t_0) = (l - k)t_{pr}$ and the real value of T_p

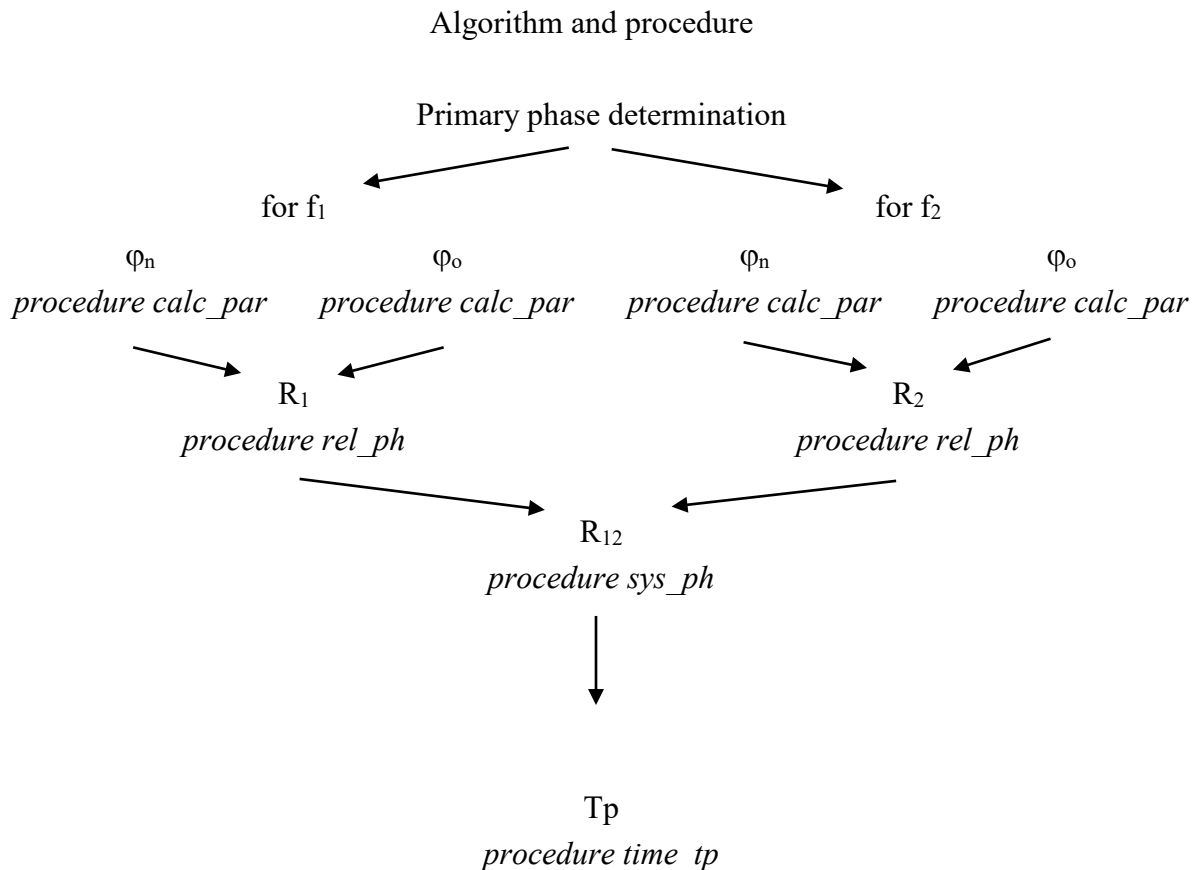
$$|T_p - (t_1 - t_0)| < \frac{1}{2|f_1 - f_2|} \quad (23)$$

The second condition determines the range of accessible probing signal parameters ensuring method correctness within the assumed range of the elementary phase errors φ

$$\Delta\varphi < \frac{\pi(f_1 - f_2)}{4f_2} \quad \text{for } f_2 > f_1 \quad (24)$$

The above limitations connect signal parameters (f_1 and f_2) with properties of a measuring system (t_{pr} , $\Delta\varphi$) determining so-called "range of measuring method applicability". The digital signal conversions for phase analysis are irrespective of the precisely determined times concerning transmitting $t=0$ and receiving $t=T_p$ of acoustic signals. It also required to analyse within the time range of the stabilised harmonic oscillations at the moments of the signal sampling $t_0 = kt_{pr}$, $t_1 = lt_{pr}$.

Using quasi constant wave packets, i.e., longer probing pulses e.g. 50-80 μ s than used for typical pulse technique e.g. 1 μ s. It is very crucial that the same conditions prevail in order to get reliable measurements. The phenomena of overlapping wave packets should not take place. However, the phase analysis allows us to get the higher time resolution T_p taken as ability of precise determination (in a sense of time) of the moments of ultrasound echo signal coming from the structures located in space. The measurements carried out by the proposed method can find applications in monitoring of the phenomena (phase method) as well as in medium state determination (time method). This procedure is exactly enough to calculate the phase and time within the expected range.



For this purpose, a 16-bit A to D Converter we are able to realise the phase resolution on the level of 0.03° - which is sufficient for our purpose. However, due to its complexity and amount of single step calculations – too many loops – this procedure is too time consuming. Matlab™ procedure for the phase calculating

4.4 Matlab™ procedure for the phase calculating

In practical application with a standard high-end PC, or even DSP, it is possible to achieve 0.7 measurements per second (MPS) at the utmost which is highly unsatisfactory for our intention. Beneath is a simple Matlab™ function accommodating the described algorithms with the method shown. Please take a notice that this is a calculation procedure only, without data acquisition and presentation [45].

```

function [phi, dl1, dl2, dm1, dm2, a] = calculate_phase(num_sampling, sample, f, t)

% [phi,dl1,dl2,dm1,dm2,a] = CALCULATE_PHASE(num_sampling, sample, f, t) calculates
% the phase difference PHI of the ...
%
% ... where num_sampling is the number of sampling points, sample is a matrix containing
% the data, f is the origin frequency and t is the sampling step (1/fs)

i1=1:num_sampling;                                % array with size of sampling points
x = 2.*pi.*(f.*t).*(i1-1);                          % argument as help to minimize following formulas
  
```

```

s_y = sum(sample); % Sum of all sample points

s_ysin = sum(sample(1:num_sampling).*sin(x)); % sampling * Sinus
s_ycos = sum(sample(1:num_sampling).*cos(x)); % sampling * Cosine
s_sin = sum(sin(x)); % Sinus
s_cos = sum(cos(x)); % Cosine

s_sin_2 = sum((sin(x)).^2); % SinusSinus
s_cos_2 = sum((cos(x)).^2); % CosineCosine

s_sincos = sum(sin(x).*cos(x)); % SinusCosine

clear x il;

% Calculation of partial equitation's

dl1 = (num_sampling*s_ysin-s_y*s_sin)*(s_sin*s_cos-num_sampling*s_sincos);
dl2 = (s_y*s_cos-num_sampling*s_ycos)*(s_sin*s_sin-num_sampling*s_sin_2);
dm1 = (num_sampling*s_sincos-s_sin*s_cos)*(s_sin*s_cos-num_sampling*s_sincos);
dm2 = (s_cos*s_cos-num_sampling*s_cos_2)*(s_sin*s_sin-num_sampling*s_sin_2);

%%%%%%%%%%%%%%%%%%%%%%%%%%%%%%%%%%%%%%%%%%%%%%%%%%%%%%%%%%%%%%%%%%%%%%%%

d = (dl1+dl2)/(dm1+dm2);
c = (s_y*s_sin-num_sampling*s_ysin+num_sampling*d*s_sincos*s_sin*s_cos)/(s_sin*s_sin-
num_sampling*s_sin_2);

% Phase calculation

phi = atan(d/c); % Four quadrant inverse tangent

if d < 0
    phi = phi + 2*pi;
end
if c < 0
    phi = phi - pi;
end
if ((c < 0)&(d>0))
    phi = phi + 2*pi;
end

if abs(sin(phi))>0.1
    a = d/sin(phi);
else
    a = c/cos(phi);
end

phi = phi / pi * 180;

```

Matlab™ posses an internal profile function which can be using to estimate the calculation time and to improve the code.

This is a static copy of a profile report

calculate_phase (9100 calls, 0.347 sec)

Generated 09-Jan-2019 08:21:31 using cpu time.

function in file C:\MatLAB\MatLABs_Jobs\calculate_phase.m

Copy to new window for comparing multiple runs

Parents (calling functions)

No parent

Lines where the most time was spent

Line Number	Code	Calls	Total Time	% Time	Time Plot
35	clear x, i1;	9100	0.096 s	27.6%	
33	s_sincos = sum(sin(x).*cos(x))...	9100	0.050 s	14.4%	
26	s_ycos = sum(sample(1:num_samp...	9100	0.042 s	12.1%	
25	s_ysin = sum(sample(1:num_samp...	9100	0.028 s	8.0%	
20	i1=1:num_sampling;	9100	0.020 s	5.7%	
All other lines			0.112 s	32.2%	
Totals			0.347 s	100%	

Table 3: Time allocation and consuming table for the phase calculation procedure

Children (called functions)

No children

Coverage results

Show coverage for parent directory

Total lines in function	71
Non-code lines (comments, blank lines)	38

Code lines (lines that can run)	33
Code lines that did run	24
Code lines that did not run	9
Coverage (did run/can run)	72.73 %

Table 4: Optimisation table for the used procedure

Function listing

```

time  calls  line
sample, f, t)
2
3 % [phi,d11,d12,dm1,dm2,a] = CALCULATE_PHASE(num_sampling, sample, f, t)
calculates
4 % the phase difference PHI of the ...
5 %
6 % ... where num_sampling is the number of sampling points, sample is a
matrix containing
7 % the data, f is the origin frequency and t is the sampling step (1/fs).
8 % The function calculates the difference phi, d11 the ???, d12 the ???,
9 % dm1 the ???, dm2 the ??? and a is the??
10 %
11 %
12 %
13 %
14 %
15 %
16 %
17 %
18 %
19
0.02  9100  20  i1=1:num_sampling;
      % array with size of sampling points
< 0.01  9100  21  x = 2.*pi.*(f.*t).*(i1-1);
      % argument as help to minimize following formulas
22
0.01  9100  23  s_y = sum(sample);
      % Sum of all sample points
24
0.03  9100  25  s_ysin = sum(sample(1:num_sampling).*sin(x)); % Samplingpunkte * Sinus
0.04  9100  26  s_ycos = sum(sample(1:num_sampling).*cos(x)); % Samplingpunkte * Cosine
< 0.01  9100  27  s_sin = sum(sin(x)); % Sinus
0.01  9100  28  s_cos = sum(cos(x)); % Cosine
29
0.02  9100  30  s_sin_2 = sum((sin(x)).^2); % SinusSinus
0.02  9100  31  s_cos_2 = sum((cos(x)).^2); % CosineCosine
32
0.05  9100  33  s_sincos = sum(sin(x).*cos(x));
      % SinusCosinus
34
0.10  9100  35  clear x, i1;
36
37 % Calculation of partial equitation's
38
9100  39  d11 = (num_sampling*s_ysin-s_y*s_sin)*(s_sin*s_cos-num_sampling*s_sincos);

```

```

< 0.01    9100    40 dl2 = (s_y*s_cos-num_sampling*s_ycos)*(s_sin*s_sin-num_sampling*s_sin_2);
          9100    41 dm1 = (num_sampling*s_sincos-s_sin*s_cos)*(s_sin*s_cos-
num_sampling*s_sincos);
< 0.01    9100    42 dm2 = (s_cos*s_cos-num_sampling*s_cos_2)*(s_sin*s_sin-
num_sampling*s_sin_2);
          43
          44 %%%%%%%%%%%%%%%%%%%%%%%%%%%%%%%%%%%%%%%%%
          45
          9100    46 d = (dl1+dl2)/(dm1+dm2);
          9100    47 c = (s_y*s_sin-
num_sampling*s_ysin+num_sampling*d*s_sincos*s_sin*s_cos)/(s_sin*s_sin-num_sampling*s_sin_2);
          48
          49 % Phase calculation

          50
          51 %phi = atan2(d,c); % Four quadrant inverse tangent
          52
          9100    53 phi = atan(d/c);
          54
< 0.01    9100    55 if d < 0
          56     phi = phi + 2*pi;
          57 end
          9100    58 if c < 0
          59     phi = phi - pi;
          60 end
          9100    61 if ((c < 0)&(d>0))
          62     phi = phi + 2*pi;
          63 end
          64
          9100    65 if abs(sin(phi))>0.1
          9100    66     a = d/sin(phi);
          67 else
          68     a = c/cos(phi);
          69 end
          70
< 0.01    9100    71 phi = phi / pi * 180;

```

To improve this procedure, the matrix representation of the data representation as well as the calculation procedure can be applied. This is the native environment by Matlab™ and is presented in the next chapter Matrix algorithm for determining the phase and amplitude

4.5 Matrix algorithm for determining the phase and amplitude

As shown in the previous part, the standard “loop” method is simple but extremely time consuming and not optimal for today’s computers or controller systems. Some better and more suitable algorithm for the phase and time calculation should be found and applied.

Based on the same idea for phase and time calculation as presented in the previous chapter, another approach to the solution needed, in the form of a matrix algorithm, is presented here [46]. It is possible to determine, with almost absolute accuracy, the phase and amplitude difference of two ultrasonic signals. It is assumed, that the two ultrasonic input signals have a sinusoidal shape:

$$x_1(t) = A_1 \sin(\omega_1 t + \varphi_1)$$

$$x_2(t) = A_2 \sin(\omega_2 t + \varphi_2)$$

where: $A_1, A_2, \varphi_1, \varphi_2$ represent respectively unknown amplitude and phase, the $\omega_s = 2\pi f_s$ is the known pulsation of the input signal.

After a simple trigonometric conversion of the two signals, they can be stored as follows:

$$\begin{aligned} x_1 &= A_1 \cos \varphi_1 \sin \omega_s t + A_1 \sin \varphi_1 \cos \omega_s t = C_0 \sin \omega_s t + C_1 \cos \omega_s t \\ x_2 &= A_2 \cos \varphi_2 \sin \omega_s t + A_2 \sin \varphi_2 \cos \omega_s t = D_0 \sin \omega_s t + D_1 \cos \omega_s t \end{aligned} \quad (25)$$

in which:

$$\begin{aligned} C_0 &= A_1 \cos \varphi_1 & D_0 &= A_2 \cos \varphi_2 \\ C_1 &= A_1 \sin \varphi_1 & D_1 &= A_2 \sin \varphi_2 \end{aligned} \quad (26)$$

After these transformations, the desired phase and amplitude are determined by means of a simple changeover:

$$\begin{aligned} A_1 &= \sqrt{C_0^2 + C_1^2} & \varphi_1 &= \arctg \left[\frac{C_1}{C_0} \right] + [1 - \text{sgn}(C_0)] \cdot \frac{\pi}{2} \\ A_2 &= \sqrt{D_0^2 + D_1^2} & \varphi_2 &= \arctg \left[\frac{D_1}{D_0} \right] + [1 - \text{sgn}(D_0)] \cdot \frac{\pi}{2} \end{aligned}$$

In order to estimate the values of amplitude and phase, knowledge of the parameters, C_i and D_i is required. These are determined by simply comparing the actual samples $x_i(t_n)$ (for $i = 0,1$) of the samples obtained at a uniform sampling frequency f_p . Best suited for this seems to be the use of the "least squares method". In the first estimation step, this provides the optimal evaluation of the global errors of the individual parameters by requiring only $m = 4 \dots 50$ samples of discrete input signals.

In order to estimate the values of amplitude and phase, knowledge of the parameters, C_i and D_i is required.

$$\begin{aligned} \frac{\partial}{\partial C_i} \left\{ \sum_{n=0}^{m-1} \left[\sum_{k=0}^1 C_k \phi_k(t_n) - x_1(t_n) \right]^2 \right\} &= 0 \\ \frac{\partial}{\partial D_i} \left\{ \sum_{n=0}^{m-1} \left[\sum_{k=0}^1 D_k \phi_k(t_n) - x_2(t_n) \right]^2 \right\} &= 0 \end{aligned} \quad (27)$$

where: $\phi_0(t) = \sin \omega_s t, \phi_1(t) = \cos \omega_s t$

The redesign of the equations above leads to obtaining a linear 2x2 equation system whose solution is the C_i , D_i parameter.

$$\begin{aligned} \sum_n^{m-1} \left[\phi_j(t_n) \sum_{k=0}^1 C_k \phi_k(t_n) \right] &= \sum_n^{m-1} \phi_j(t_n) x_1(t_n) \\ \sum_n^{m-1} \left[\phi_j(t_n) \sum_{k=0}^1 D_k \phi_k(t_n) \right] &= \sum_n^{m-1} \phi_j(t_n) x_2(t_n) \quad j=0,1 \end{aligned}$$

Solutions of this linear system of equations could be represented in the form of a matrix, which is the best form for processing in the Matlab environment

$$\begin{aligned} A^T A C &= A^T X_1 \\ A^T A D &= A^T X_2 \end{aligned} \tag{28}$$

where:

$$A = \begin{vmatrix} \sin \omega_s t_0 & \cos \omega_s t_0 \\ \sin \omega_s t_1 & \cos \omega_s t_1 \\ \dots & \dots \\ \dots & \dots \\ \sin \omega_s t_{m-1} & \cos \omega_s t_{m-1} \end{vmatrix}$$

the input signal vectors are given in the following form

$$X_1 = \begin{vmatrix} x_1(t_0) \\ x_1(t_1) \\ \dots \\ \dots \\ x_1(t_{m-1}) \end{vmatrix} \quad X_2 = \begin{vmatrix} x_2(t_0) \\ x_2(t_1) \\ \dots \\ \dots \\ x_2(t_{m-1}) \end{vmatrix}$$

and the matrix product $A^T A$ could be stored as follows:

$$A^T A = \begin{vmatrix} \sum_{n=0}^{m-1} \sin^2 \omega_s t_n & \frac{1}{2} \sum_{n=0}^{m-1} \sin 2 \omega_s t_n \\ \frac{1}{2} \sum_{n=0}^{m-1} \sin 2 \omega_s t_n & \sum_{n=0}^{m-1} \cos^2 \omega_s t_n \end{vmatrix}$$

the vectors of the searched parameters, then take the following form:

$$C = \begin{bmatrix} C_0 \\ C_1 \end{bmatrix} \quad D = \begin{bmatrix} D_0 \\ D_1 \end{bmatrix}$$

This way of writing allows premature formation of the auxiliary arrays A and $A^T A$ when the input signal frequency f_s , sampling frequency f_p and the amount of samples m are known. This step brings a significant acceleration in the computational speed of the algorithm mentioned above. The solution of the system of equations in the form of a matrix allows us to estimate directly the parameters C_i and D_i :

$$\begin{aligned} C &= A^T X_1 / A^T A \\ D &= A^T X_2 / A^T A \end{aligned} \tag{29}$$

Based on the previously presented formula, the phases and amplitudes of the two ultrasonic signals are now uniquely determined.

$$\Delta\varphi = \varphi_1 - \varphi_2$$

$$\Delta A = A_1 - A_2$$

The algorithm presented above was written and tested as a Matlab script (please see below). For a given number of samples, $m = 5$, ultrasonic signal frequency $f_s = 4.3$ MHz and a sampling frequency $f_p = 50$ MHz (corresponding to the parameters of the ultrasonic signals used), a simulation is started and evaluated. A change of the start phase and the amplitude of the input signal is simulated as follows: every 10° , the phases of the first and second signals varied from 0° to $\pm 720^\circ$.

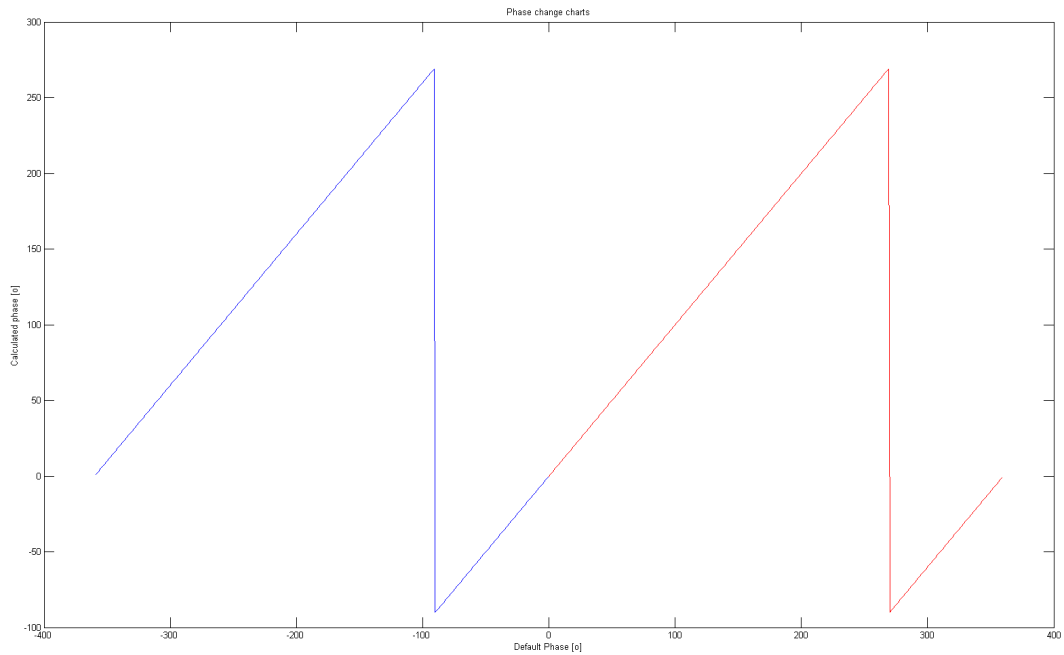


Figure 17: Diagram of time estimation method T_p .

The algorithm correctly reproduces the phases of the test signals within the given range (one full cycle, 2π). In order to determine the angle of the phase shift by more than a full 360° angle (change of more than one ultrasound wavelength), it is necessary to make a further adjustment to the algorithm which provides further processing of the information obtained.

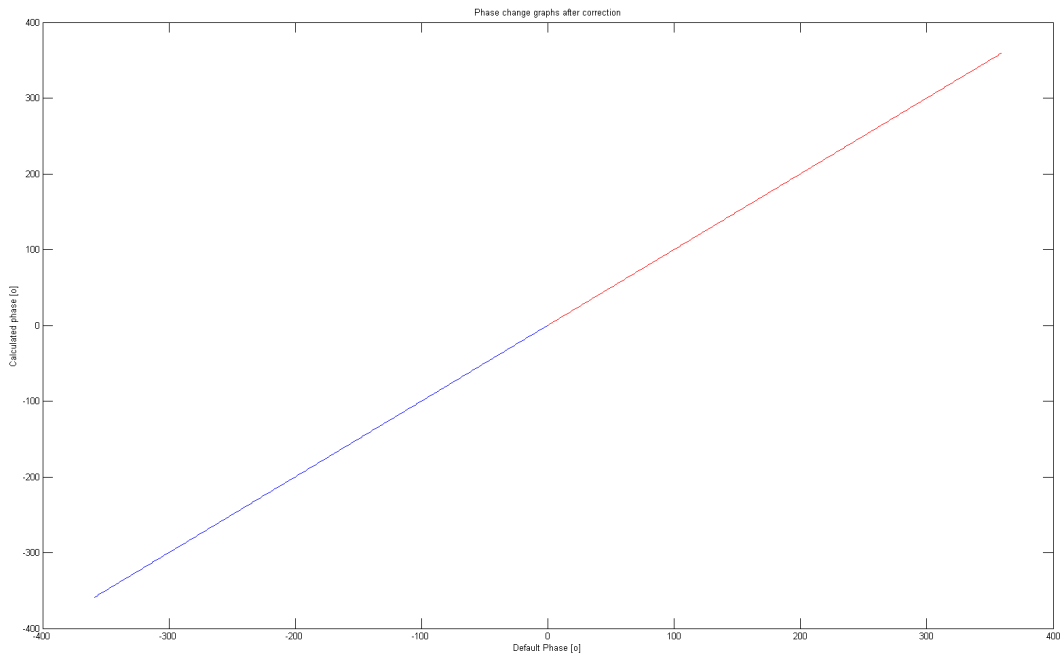


Figure 18: Diagram of time estimation method T_p

For the purpose of error estimation, a direct numerical difference / error between the predefined and the calculated phases is shown in a diagram.

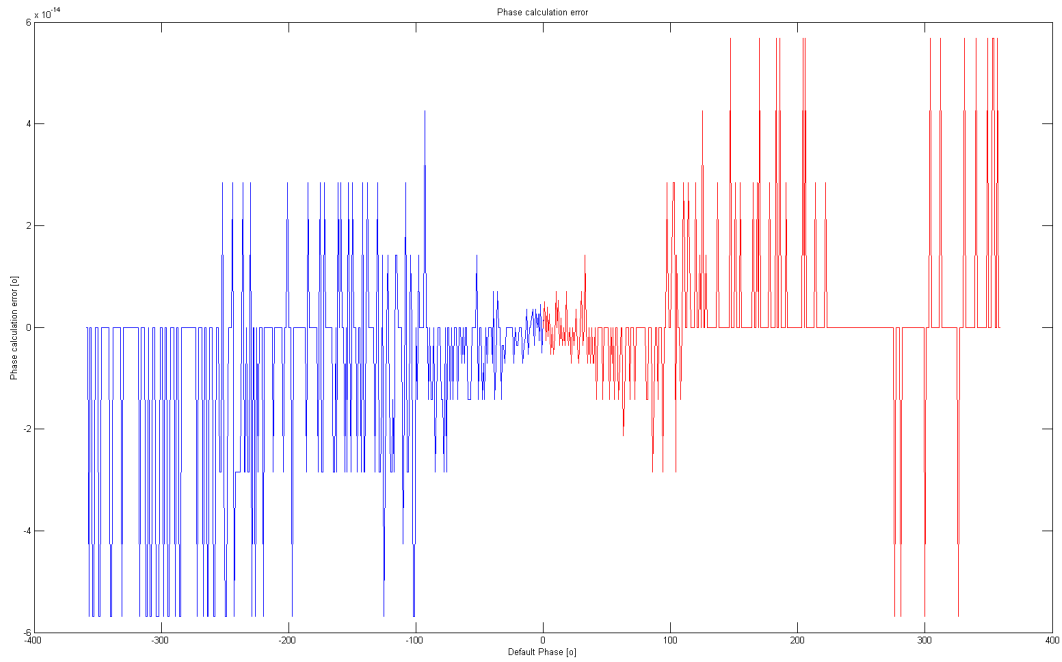


Figure 19: Diagram of time estimation method Tp.

As can be seen in fig.19, this error is very small, its value is in the order of 10^{-13} ° and should not affect the error value of the entire measurement method. It should be noticed that this resolution is based on the Matlab internal variable representation with 128-bit or more for a double float values. In a real word, the input date will be normally 16-bit and has the representation of uint(16) – means a 16-bit Integer without signs. The whole data range is then between 0 and 65,536 of the input values.

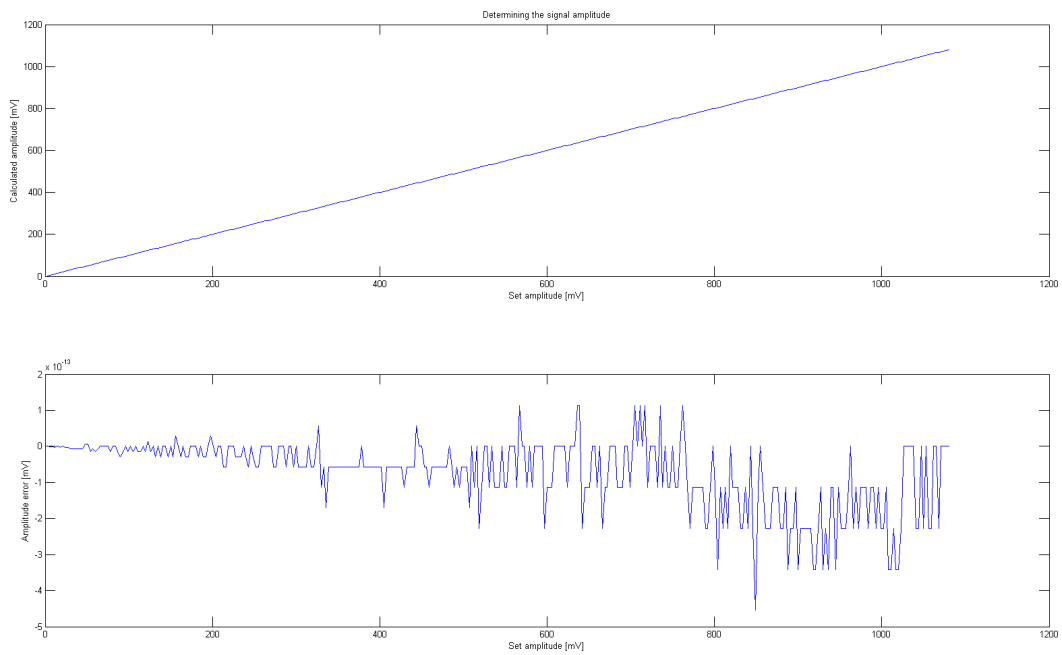


Figure 20: Diagram of time estimation method Tp

The above drawings show the given and reconstructed amplitude and the error between them. The error is calculating as the amplitude determination on the example of the estimation of the

amplitude of the first ultrasonic echo. It shows that the correct calculation of the input signal amplitude with neglectable very small error, the value of the calculating amplitude error is the same as the phase, due to the Matlab variable representation as review before.

4.6 Matlab™ matrix procedure for phase calculation

```

close all;
clear all;
clc;
profile on;

xx = 1;

% Program Start %

FSampl = 96e6; % Sampling Frequency in MHz
Time = 20e-6; % Transmission Time in sec.
freq(1) = 1.9e6; % Transmission Frequency in MHz
Phase(1) = 31.796321; % Phase(1) = random('Normal',30,55,1,1);

res1 = createsinus(1, 0, freq(1), Time, Phase(1), FSampl);
Freq1 = int16(res1); % Build a Signal
Freq = double(Freq1); % Build a Signal

%% Phase Analysis of Transmitted Signal
start = 1; % Start point of the signal calculation
lp = FSampl/gcd(FSampl,freq(1)); % Set of samples for calculation
tp = 1/FSampl; % Sampling period in sec
lp = 481;
t_analyze = (start-1)*tp:tp:(start+lp-2)*tp;

%% Profiler Starts
tic;

num = 1;

% Data samples, Transfer and start of calculations
a_1 = sin(2*pi*freq(num)*t_analyze);
a_2 = cos(2*pi*freq(num)*t_analyze);
A = [a_1' a_2'];
AA = A'*A;
b = Freq(start:start+lp-1)'; % Sample vector of the first signal
g = Freq(start:start+lp-1)'; % Sample vector of the second signal
B1 = A'* b;
B2 = A'* g;
C = AA\B1;
D = AA\B2;

% phase calculation
phi(num) = atan(C(2)/C(1))+(1-sign(C(1)))*(pi/2);
phi(xx,num) = phi(num)/pi*180; % Output in [°] otherwise in [rad]
if D(1) == 0,
    D(1) = 1e-32;
end

% amplitude calculation
ampl(xx,num) = sqrt((C(1)^2)+(C(2)^2));
phi(num) = phi(1,num);

```

```

toc;

%% Display calculated values
Differ(xx,1) = Phase(1) - phi(1);
disp(xx)
disp('Amplitude Freq1')
disp(ampl)
disp('Phase Sim in ° Freq1')
disp(Phase)
disp('Phase in ° Freq1')
disp(phi)
disp('Phase differ in ° Freq1')
disp(Differ)

profile viewer
p = profile('info')

```

Running of those script produce the following results:

Elapsed time is 0.000146 seconds.

Amplitude Freq1

1.1036

Phase Sim in ° Freq1

31.7963

Phase in ° Freq1

31.7646

Phase differ in ° Freq1

0.0317

```

FunctionTable: [2x1 struct]
FunctionHistory: [2x4 double]
ClockPrecision: 1.0000e-03
ClockSpeed: 2.2010e+09
Name: 'MATLAB'
Overhead: 0

```

The function tic and toc can be used to measure the calculations performance, how much time is required to solve a linear system varies with the order of a matrix. The tic starts the stopwatch timer and the toc stops the timer. The performance of above described matrix procedure is 146 μ s for a single cycle. This can be matched to the “loop” procedure with 0.347s, which shows that the matrix procedure is more than 2300 faster than the previous one. The phase calculation

resolution using the 16-bit input data is in a satisfactory range of 0.03° as demanded. The above presented Matlab script used a particular procedure “*createsinus*” in one of the starting lines:

```
res1 = createsinus(1, 0, freq(1), Time, Phase(1), FSamp1);
```

the whole function is presented here.

```
function res = createsinus(A0, t0, f0, t1, ph0, f_s)
%
% res = createsinus(A0, t0, f0, t1, ph1, f_s)
%
% A0   : Signal amplitude
% t0   : Signal starting point [s]
% f0   : Signal frequency [Hz]
% t1   : Frame [s]
% ph0  : Starting phase [°]
% f_s  : Sampling (default: 20MHz)
%
% Argument list check
if (nargin < 5)
    error('Not enough arguments!')
    help createsinus
end

if (nargin > 6)
    error('Too much arguments!')
    help createsinus
end

if (nargin == 5)
    f_s = 20E6;      % Sampling (Default: 20MHz)
end

T_s = 1 / f_s;    % Sampling time [s]

t_vec = (t0:T_s:(t1 - T_s));
res = A0*sin((2*pi*f0*t_vec)+(pi*ph0)/180);
```

it uses only the Matlab internal function and helps to keep the test procedure and script clean.

5 Chapter 5

The invention presented in this chapter relates to phase detection and fast phase processing. Interpreting the signal phase precisely is of the great importance for a number of applications, not only for the ACG. The phase information coding methods in communication engineering can, for example, be used for secure data transmission or expanding the communication channel bandwidth. In the area of material sciences, measuring of an acoustic wave phases provides information on the material composition as its chemical and physical characteristics and structure. The same applies to medical diagnostics as this work demonstrates. The goal of the present innovation and description is to create a concept to easily and precisely determine the phase of the known signal after it passes the examining medium.

5.1 Microchip devices for phase vector and bias block retrieving of the sampled monochromatic signal

Theoretical foundations of the model or even of the future chip or FPGA device are: it is a given vector $Y_0; Y_1; \dots; Y_{N-1}$ of the sampled function values $Y_n = \beta + A \sin\left(2\pi \frac{n \cdot f_p}{f_s} + \varphi\right)$, $n = 0, 1, 2, \dots, N-1$: where f_s is the signal frequency and the f_p the sampling frequency. The approximate values of unknown parameters A , β and φ can be retrieved by the so-called least squares method using the following formulae:

$$\begin{bmatrix} Cov(S, Y) \\ Cov(C, Y) \end{bmatrix} = \begin{bmatrix} Cov(S, S) & Cov(S, C) \\ Cov(C, S) & Cov(C, C) \end{bmatrix} \times \begin{bmatrix} A \cos(\varphi) \\ A \sin(\varphi) \end{bmatrix}$$

$$\beta = \bar{Y} - A \cdot (\bar{C} \sin(\varphi) + \bar{S} \cos(\varphi))$$

Where $Cov(Z, T) = \overline{(Z - \bar{Z}) \cdot (T - \bar{T})} = \overline{ZT} - \bar{Z} \cdot \bar{T}$ is per definition a covariation of the sequences Z and T and the sequences S and C are defined as:

$$S_j \stackrel{\text{def}}{=} \sin\left(2\pi \frac{f_s}{f_p} \cdot j\right), \quad C_j \stackrel{\text{def}}{=} \cos\left(2\pi \frac{f_s}{f_p} \cdot j\right), \quad j = 0, \dots, N-1$$

It is easily to observe that, every N such fulfills $N \cdot \frac{f_s}{f_p} \in \mathbb{Z}$ is a period of the both sequences $\{S_j\}$ and $\{C_j\}$ than also N is a multiplicity of $\hat{f}_p \stackrel{\text{def}}{=} \frac{f_p}{\text{gcd}(f_p, f_s)}$: where $\text{gcd}(f_s, f_p)$ is the greatest common divisor, as per definition.

To fulfill this, phase detection method based on a receiving sequence of sampled values, has to comprise the followings steps:

- Receiving a signal sequence Y_j of values $(Y_0, Y_1, \dots, Y_{N-1})$ having been sampled with a known sampling frequency f_p
- The receiving signal Y is representing a reaction to a transmitting signal having known transmitting frequency f_s – Signal Y can be a direct transmitting or echo signal, depends on the system configuration.
- S_j and C_j is providing a sequence of sinus or cosines values for each index j of the receiving signal Y_j respectively.
- S_j sine sequence comprising sine values of consecutive multiples of known circular frequency, which depends on the transmitting frequency f_s
- C_j cosine sequence comprising cosine values of consecutive multiples of known circular frequency, which depends on the transmitting frequency f_s
- Determining the phase real part U of the receiving signal Y based on the scalar product of the receiving sequence Y_j with the cosine sequence C_j
- Determining the phase imaginary part V of the receiving signal Y based on the scalar product of the receiving sequence Y_j with the sine sequence S_j
- Determining of β (bias) based on the signal Y values

To do the whole calculation in the processor manner, some auxiliary registers are necessary.

$$\bar{S} \stackrel{\text{def}}{=} \frac{1}{N} \sum_{j=0}^{N-1} S_j = 0, \quad \bar{C} \stackrel{\text{def}}{=} \frac{1}{N} \sum_{j=0}^{N-1} C_j = 0, \quad \overline{SC} \stackrel{\text{def}}{=} \frac{1}{N} \sum_{j=0}^{N-1} S_j C_j = 0, \quad \bar{S}^2 \stackrel{\text{def}}{=} \frac{1}{N} \sum_{j=0}^{N-1} S_j^2 = \frac{1}{2}$$

as well as

$$\bar{C}^2 \stackrel{\text{def}}{=} \frac{1}{N} \sum_{j=0}^{N-1} C_j^2 = \frac{1}{2} \quad \text{and} \quad \begin{bmatrix} \overline{S \cdot Y} \\ \overline{C \cdot Y} \end{bmatrix} = \begin{bmatrix} \frac{1}{2} & 0 \\ 0 & \frac{1}{2} \end{bmatrix} \times \begin{bmatrix} A \cos(\varphi) \\ A \sin(\varphi) \end{bmatrix}$$

hence

$$U = A \cos(\varphi) = 2 \cdot \overline{CY}, \quad V = A \sin(\varphi) = 2 \cdot \overline{SY}, \quad \beta = \bar{Y}$$

So, after that the needed values can be also obtained as

$$A = \sqrt{U^2 + V^2} \quad \text{and} \quad \varphi = \left(\arcsin\left(\frac{V}{A}\right) \mathbf{mod} 2\pi \right)$$

The processor consists of timing input **CLK**; reset input **RES**, N-element input buffer Y ; two N-element constant vectors **S** and **C** as well as three output registers U ; V and β . The vectors **S**

and C contain respectively: $\sin(2\pi\sigma \cdot j)$ and $\cos(2\pi\sigma \cdot j)$ where $j = 0, 1, \dots, N - 1$ where σ is a quotient of the signal frequency f_s and the corresponding sampling frequency f_p : $\sigma \stackrel{\text{def}}{=} \frac{f_s}{f_p} = \frac{\hat{f}_s}{\hat{f}_p}$

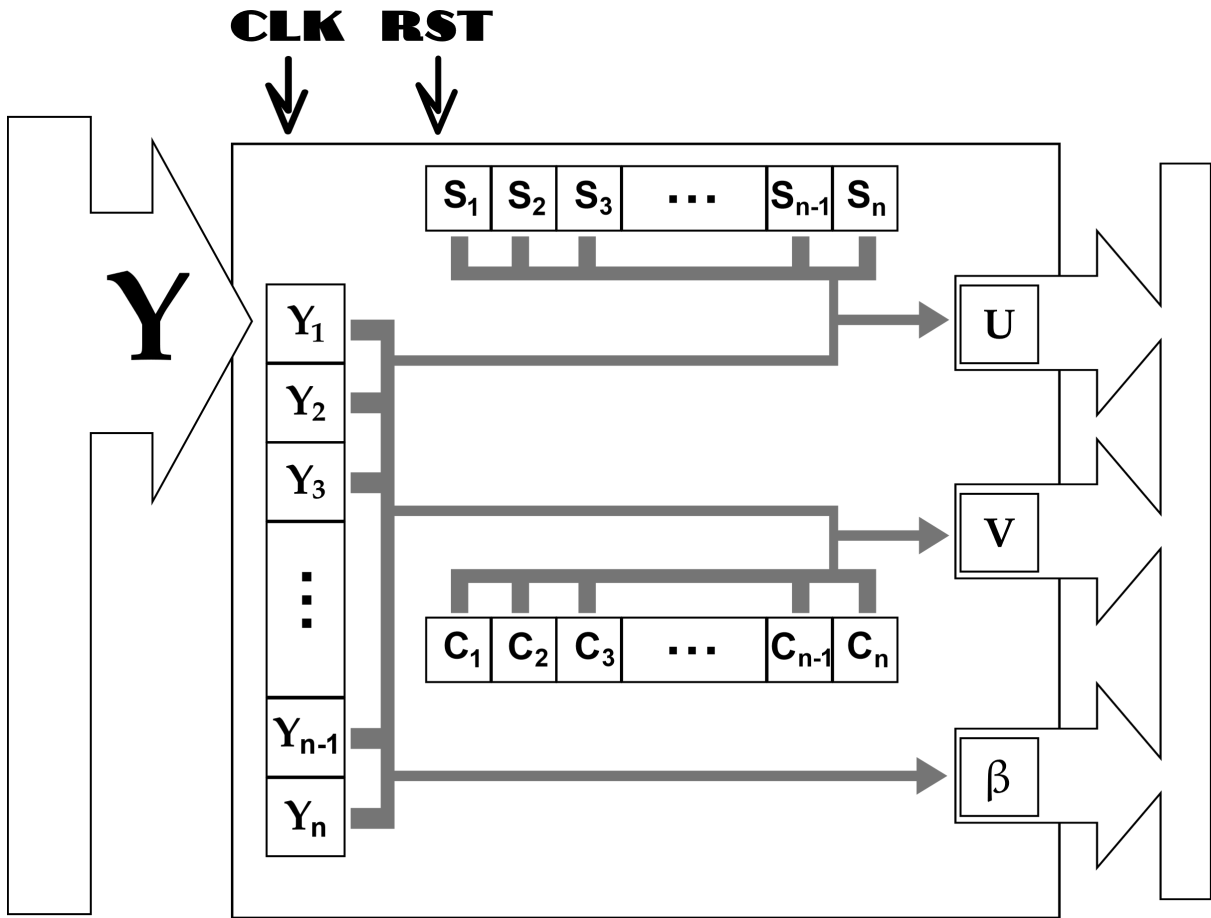


Figure 21: Block processors draft

The operation cycle of such processor is as follow: after having turned on (what is an equivalent to receiving the resetting signal **RES**), data are send from data bus to buffer Y and then the registers U and V are fed up with the values of $\frac{2}{N}Y \circ C$ and $\frac{2}{N}Y \circ S$ where " \circ " is the inner product of this two values. The mean value $\bar{Y} = \frac{1}{N}\sum_{j=1\dots N} Y_j$ is stored in the β register as supposed [47].

5.2 Simulink™ simulator of monochrome Signal Phase Vector Determination Circuit

This chapter describes the Simulink microchips simulators used to determine the phase vector on the basis of a monochromatic (or monochromatic phase processors, abbreviated as MPF). It considering MPF in block and streaming version, streaming processors are shown in two variants: as LSM and TRI processors. In addition, stream processors can (but do not have to) consist the averaging module. First the block processing will be described.

5.3 Simulink™ simulator of a Block Processors

Block processors produce the phase vector elements U and V on the basis consecutive “sequences” of monochrome signal Y_0, \dots, Y_{N-1} ; as shown it is in the following diagram.

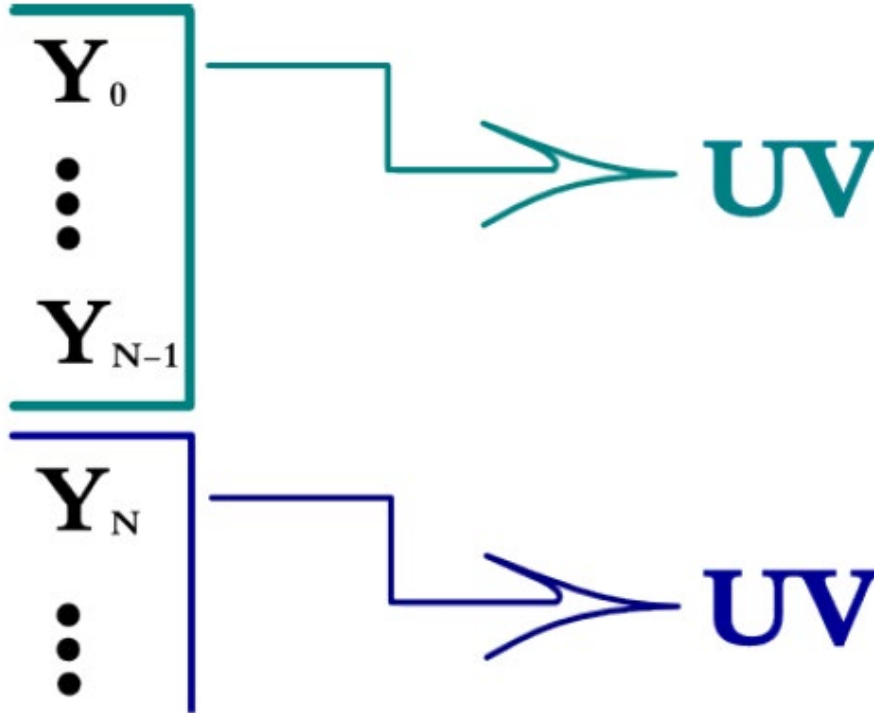


Figure 22: The operation of block processors

5.4 Block processor model

The solution presented here is based on the following formula:

$$\begin{bmatrix} cov(S, Y) \\ cov(C, Y) \end{bmatrix} = \begin{bmatrix} cov(S, S) & cov(S, C) \\ cov(C, S) & cov(C, C) \end{bmatrix} \times \begin{bmatrix} U \\ V \end{bmatrix} \quad (30)$$

Follow by:

$$\begin{bmatrix} U \\ V \end{bmatrix} = \begin{bmatrix} cov(S, S) & cov(S, C) \\ cov(C, S) & cov(C, C) \end{bmatrix}^{-1} \times \begin{bmatrix} cov(S, Y) \\ cov(C, Y) \end{bmatrix} \text{ and finally:}$$

$$\begin{bmatrix} U \\ V \end{bmatrix} = \begin{bmatrix} cov(S, S) & cov(S, C) \\ cov(C, S) & cov(C, C) \end{bmatrix}^{-1} \times \begin{bmatrix} S - \bar{S} \\ C - \bar{C} \end{bmatrix} \times Y \quad (31)$$

where $Y = \begin{bmatrix} Y_0 \\ \dots \\ Y_{N-1} \end{bmatrix}$ are the consecutive signal samples values. The following model produces elements of the complex phase vector based on the above equations.

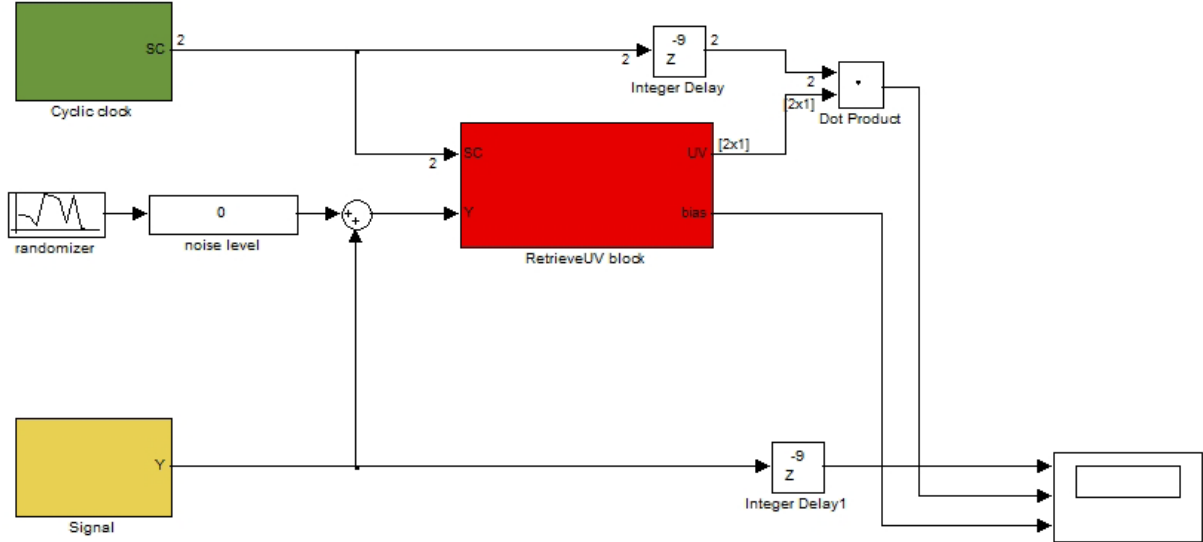


Figure 23: Block processor model

The first segment of the above model - **Cyclic clock**, is marked with dark green color - it produces the SC signal where the known transmitting frequency f_s is now Ω :

$$\begin{bmatrix} 0 \\ 1 \end{bmatrix}, \begin{bmatrix} \sin(\Omega) \\ \cos(\Omega) \end{bmatrix}, \begin{bmatrix} \sin(2\Omega) \\ \cos(2\Omega) \end{bmatrix}, \dots, \begin{bmatrix} \sin((N-1)\Omega) \\ \cos((N-1)\Omega) \end{bmatrix}, \begin{bmatrix} 0 \\ 1 \end{bmatrix}, \dots \quad (32)$$

The following diagram fig.24 shows the construction of this segment. Fragment, shown in the left part, is responsible for the production of signals: 1; 2; ...; N; 1; 2; Next, a vector is constructed, consisting of vector columns determined in this way S and C. Values of S and C vectors have been defined in Model Properties respectively as:

$$[\sin(0), \sin(\Omega), \dots, \sin((N-1)\Omega)], [\cos(0), \cos(\Omega), \dots, \cos((N-1)\Omega),]$$

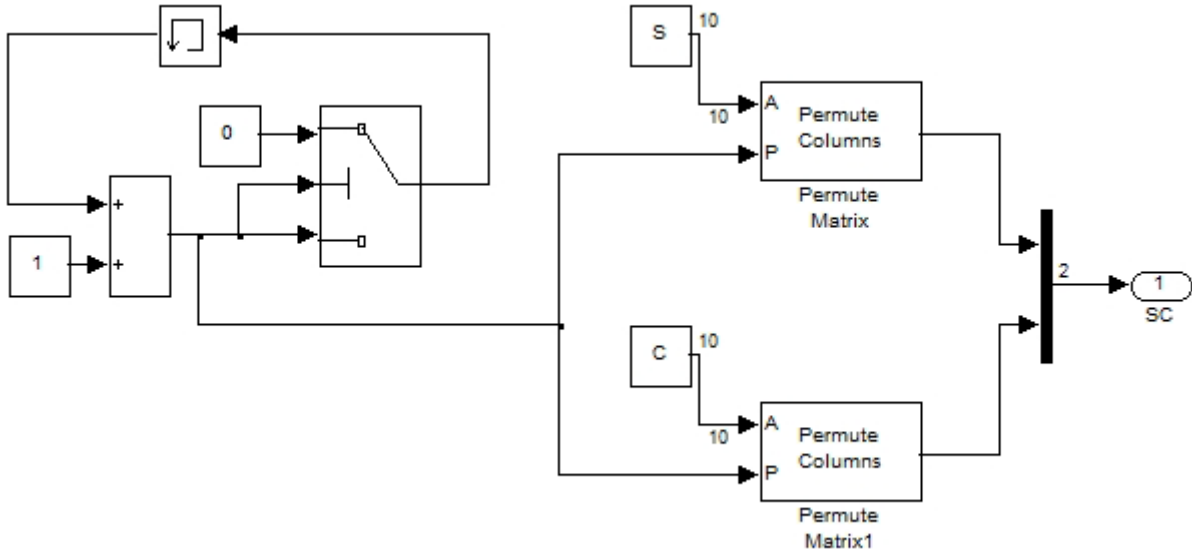


Figure 24: Block processor - **Cyclic clock** (inside view)

Another segment of the model - **Signal**, is marked with yellow colour – it produces the Y signal:

$$\sin(\varphi) + \beta, \sin(\Omega + \varphi) + \beta, \sin(2\Omega + \varphi) + \beta, \dots, \quad (33)$$

where φ is phase and β is bias of the signal. In the diagram below the construction of this segment is presented.

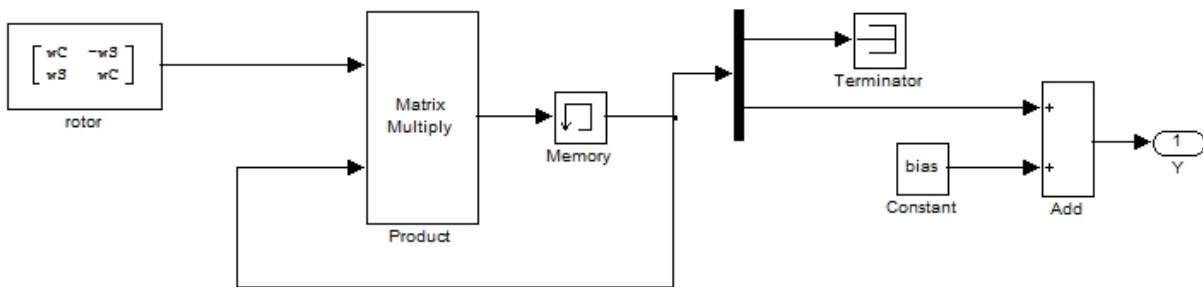


Figure 25: Matrix block processor – **Signal** (inside view)

The last segment - **Retrieve UV block**, is highlighted in red – it receives the Y signal values and returns the phase vector elements U, V values. The next diagram presents the construction of this segment. The fragment, shown in the left part is responsible for the production of signal values “sequence”:

$$[0 \ \dots \ 0]^T, [Y_0 \ \dots \ Y_{N-1}]^T, [Y_1 \ \dots \ Y_N]^T, [Y_N \ \dots \ Y_{2N-1}]^T, \dots \quad (34)$$

The first outcoming value is incorrect due to transient behaviour of the system – it is well known situation of the all digital filters, as the phase retractor is, as well. While created there is another piece (which happens in N steps), the value is passed the previous vector. Therefore, each piece is sent N times.

where constant matrix M

$$M = \begin{bmatrix} cov(S,S) & cov(S,C) \\ cov(C,S) & cov(C,C) \end{bmatrix}^{-1} \times \begin{bmatrix} S - \bar{S} \\ C - \bar{C} \end{bmatrix}$$

is multiplied by subsequent pieces, which gives the $\begin{bmatrix} U \\ V \end{bmatrix}$ phase vector according to formula (2). In addition, this model calculates the value of the scalar product of the $\begin{bmatrix} U \\ V \end{bmatrix}$ vector and the signal taken from the Cyclic clock. Then this value is subtracted on the value of the Y signal, which gives the value of deviation β (bias) according to the following equation:

$$\beta = Y_j - (U \cdot \sin(j\Omega) + V \cdot \cos(j\Omega)) \quad (35)$$

Where $j = 0, \dots, N-1$.

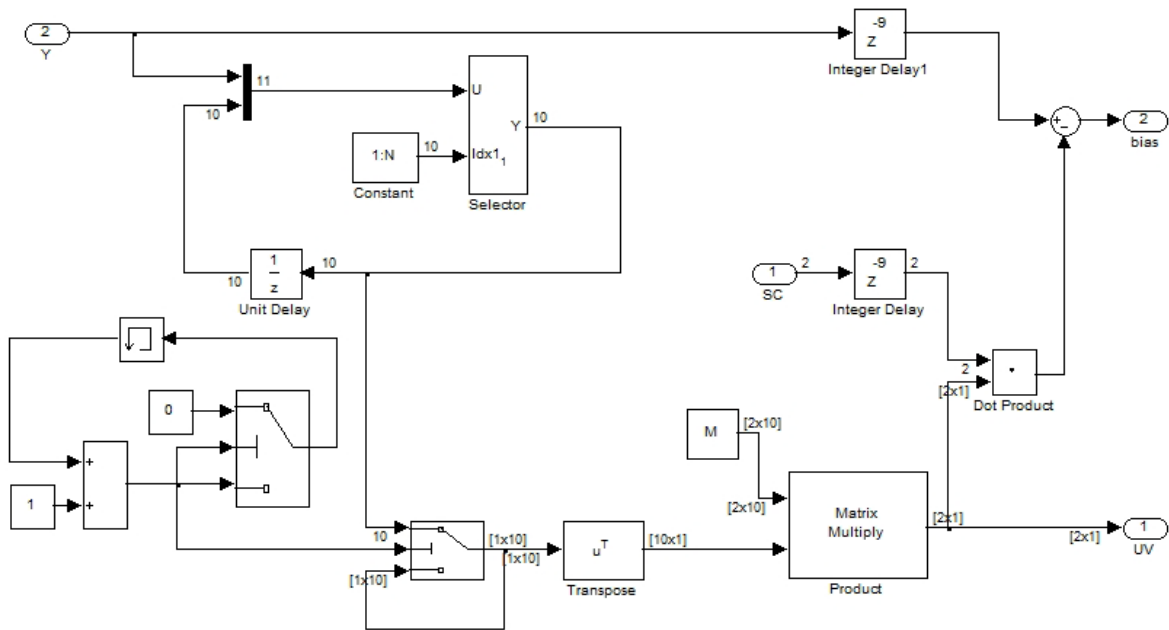


Figure 26: Matrix block processor - **Retrieve UV block** (inside view)

The following is a summary of the data collected from the model in which the following values were accepted: $N = 10$, $f_s = 0:5$, $f_p = 96$, $bias = 0:75$, $phase = 30$. The compatibility of the appropriate values proves the correctness of the model.

			UV			
			0,0000000	0,0000000		
			0,0000000	0,0000000		
			0,0000000	0,0000000		
			0,0000000	0,0000000		
			0,0000000	0,0000000		
			0,0000000	0,0000000		
			0,0000000	0,0000000		
S	C	Y	0,0000000	0,0000000	U·S+V·C	bias
			0,0000000	0,0000000		
0,0000000	1,0000000	1,2500000	~ 0,8660254	0,5000000	0,5000000	0,75
0,0327191	0,9994646	1,2780679	~ 0,8660254	0,5000000	0,5280679	0,75
0,0654031	0,9978589	1,3055702	~ 0,8660254	0,5000000	0,5555702	0,75
0,0980171	0,9951847	1,3324777	~ 0,8660254	0,5000000	0,5824777	0,75
0,1305262	0,9914449	1,3587614	~ 0,8660254	0,5000000	0,6087614	0,75
0,1628955	0,9866433	1,3843933	~ 0,8660254	0,5000000	0,6343933	0,75
0,1950903	0,9807853	1,4093458	~ 0,8660254	0,5000000	0,6593458	0,75
0,2270763	0,9738770	1,4335923	~ 0,8660254	0,5000000	0,6835923	0,75
0,2588190	0,9659258	1,4571068	~ 0,8660254	0,5000000	0,7071068	0,75
0,2902847	0,9569403	1,4798641	~ 0,8660254	0,5000000	0,7298641	0,75
0,0000000	1,0000000	1,5018398	~ 0,6593458	0,7518398	0,7518398	0,75
0,0327191	0,9994646	1,5230105	~ 0,6593458	0,7518398	0,7730105	0,75
0,0654031	0,9978589	1,5433533	~ 0,6593458	0,7518398	0,7933533	0,75
0,0980171	0,9951847	1,5628467	~ 0,6593458	0,7518398	0,8128467	0,75
0,1305262	0,9914449	1,5814696	~ 0,6593458	0,7518398	0,8314696	0,75
0,1628955	0,9866433	1,5992022	~ 0,6593458	0,7518398	0,8492022	0,75
0,1950903	0,9807853	1,6160254	~ 0,6593458	0,7518398	0,8660254	0,75
0,2270763	0,9738770	1,6319213	~ 0,6593458	0,7518398	0,8819213	0,75
0,2588190	0,9659258	1,6468727	~ 0,6593458	0,7518398	0,8968727	0,75
0,2902847	0,9569403	1,6608638	~ 0,6593458	0,7518398	0,9108638	0,75
0,0000000	1,0000000	1,6738795	~ 0,3826834	0,9238795	0,9238795	0,75
0,0327191	0,9994646	1,6859059	~ 0,3826834	0,9238795	0,9359059	0,75
0,0654031	0,9978589	1,6969301	~ 0,3826834	0,9238795	0,9469301	0,75
0,0980171	0,9951847	1,7069403	~ 0,3826834	0,9238795	0,9569403	0,75
0,1305262	0,9914449	1,7159258	~ 0,3826834	0,9238795	0,9659258	0,75
0,1628955	0,9866433	1,7238770	~ 0,3826834	0,9238795	0,9738770	0,75

Table 5: Matrix block processor - Value summary

Additionally, this model compares the values on the oscilloscope ($U \cdot \sin(j\Omega) + V \cdot \cos(j\Omega)$), where $j = 0; \dots; N-1$, with the values of Y taken from Signal and the values of deviation β (bias), the result of which is shown below.

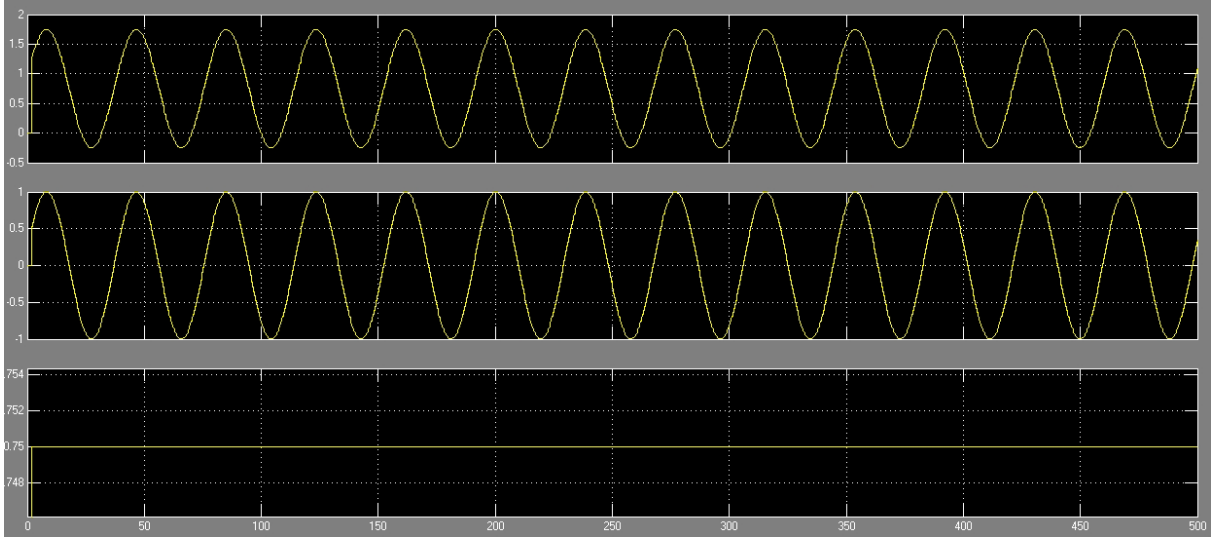


Figure 27: Matrix block processor – Oscilloscope. No transient values are observed on the left side of the target-performance comparison curves – top diagram is the target curve; the middle is the performance curve with NO transient behavior and the lower curve is the bias with NO transient behavior also (details in text)

5.5 Stream processors

Theoretical foundations of the stream processor is a given as: for a three given values of the signal vector $Y_1; Y_2; Y_3$ of the sampled function $Y_n = \beta + A \sin\left(2\pi \frac{n \cdot f_p}{f_s} + \varphi\right)$, $n = 0, 1, 2, \dots, N-1$: where f_s is the signal frequency and the f_p the sampling frequency. The approximate values of unknown parameters A, β and φ can be retrieved by so called least squares method using the following formulas. In case of simplicity we assume that $Y_1; Y_2; Y_3$ are measured in three equidistant time points with e.g. sampling frequency f_p

$$\Delta\tau = \tau_2 - \tau_1 = \tau_3 - \tau_2 < \frac{1}{2 \cdot f_p}$$

This condition guaranties exact restoring the phase values of the signal Y_j where $j=1, 2, 3$ and

$$U \stackrel{\text{def}}{=} A \cdot \cos(\varphi) \quad \text{and} \quad V \stackrel{\text{def}}{=} A \cdot \sin(\varphi)$$

Additionally, we have a following dependencies:

$$A = \sqrt{U^2 + V^2} \quad \text{and} \quad \varphi \equiv \left(\arcsin\left(\frac{V}{A}\right) \bmod 2\pi\right)$$

The U and V values satisfy a following linear equitation system:

$$\begin{cases} Y_1 = U \cdot S_1 + V \cdot C_1 + \beta \\ Y_2 = U \cdot S_2 + V \cdot C_2 + \beta \\ Y_3 = U \cdot S_3 + V \cdot C_3 + \beta \end{cases}$$

where $S_j = \sin(2\pi \cdot f_s \cdot \tau_j)$, $C_j = \cos(2\pi \cdot f_s \cdot \tau_j)$, $j \in \{1, 2, 3\}$

the linear equation system can be transformed into following construct

$$\begin{cases} Y_2 - Y_1 = U \cdot (S_2 - S_1) + V \cdot (C_2 - C_1) = 2 \sin\left(\frac{\Omega}{2}\right) (U \cdot \widehat{C}_1 - V \cdot \widehat{S}_1) \\ Y_3 - Y_2 = U \cdot (S_3 - S_2) + V \cdot (C_3 - C_2) = 2 \sin\left(\frac{\Omega}{2}\right) (U \cdot \widehat{C}_2 - V \cdot \widehat{S}_2) \end{cases}$$

where

$$\begin{aligned} \Omega &\stackrel{\text{def}}{=} 2\pi f_s \cdot \Delta\tau \quad \text{and} \quad \widehat{S}_j = \sin\left(\Omega \cdot \left(j + \frac{1}{2}\right)\right) \quad \text{and} \quad \widehat{C}_j \\ &= \cos\left(\Omega \cdot \left(j + \frac{1}{2}\right)\right) \quad , \quad j = 1, 2 \end{aligned}$$

For the simplicity we can denote $\Delta Y_j \stackrel{\text{def}}{=} Y_{j+1} - Y_j$, $j = 1, 2$ that the solution from above will take a such form

$$U = \frac{\Delta Y_1 \cdot \widehat{S}_2 - \Delta Y_2 \cdot \widehat{S}_1}{2 \sin\left(\frac{\Omega}{2}\right) \sin(\Omega)} \quad , \quad V = \frac{\Delta Y_1 \cdot \widehat{C}_2 - \Delta Y_2 \cdot \widehat{C}_1}{2 \sin\left(\frac{\Omega}{2}\right) \sin(\Omega)}$$

after the reduction of involved variables, the equation will take the following form

$$\widehat{S}_2 = \widehat{C}_1 \sin \Omega + \widehat{S}_1 \cos \Omega \quad , \quad \widehat{C}_2 = \widehat{C}_1 \cos \Omega + \widehat{S}_1 \sin \Omega$$

$$\text{and} \quad \sin \Omega = 2 \sin\left(\frac{\Omega}{2}\right) \cos\left(\frac{\Omega}{2}\right) \quad \text{and} \quad \cos \Omega = 1 - 2 \sin^2\left(\frac{\Omega}{2}\right)$$

As the last determining part of the signal, beside the U and V , the bias β hast to be calculated. The value of β can be obtained from any of this equation:

$$\beta = Y_j - (U \cdot S_j + V \cdot C_j) \quad \text{or even better from}$$

$$\beta = Y_j - \left[U \cdot \left(\widehat{S}_{j-1} \cos\left(\frac{\Omega}{2}\right) + \widehat{C}_{j-1} \sin\left(\frac{\Omega}{2}\right) \right) + V \cdot \left(\widehat{C}_{j-1} \cos\left(\frac{\Omega}{2}\right) - \widehat{S}_{j-1} \sin\left(\frac{\Omega}{2}\right) \right) \right] \quad ,$$

$$j = 2, 3$$

Basic version of the system consists of timing input **CLK**, reset input **RES**, four auxiliary registers: S_1, S_2, C_1, C_2 , three output registers U, V, β and three element input queue **FIFO Y**.

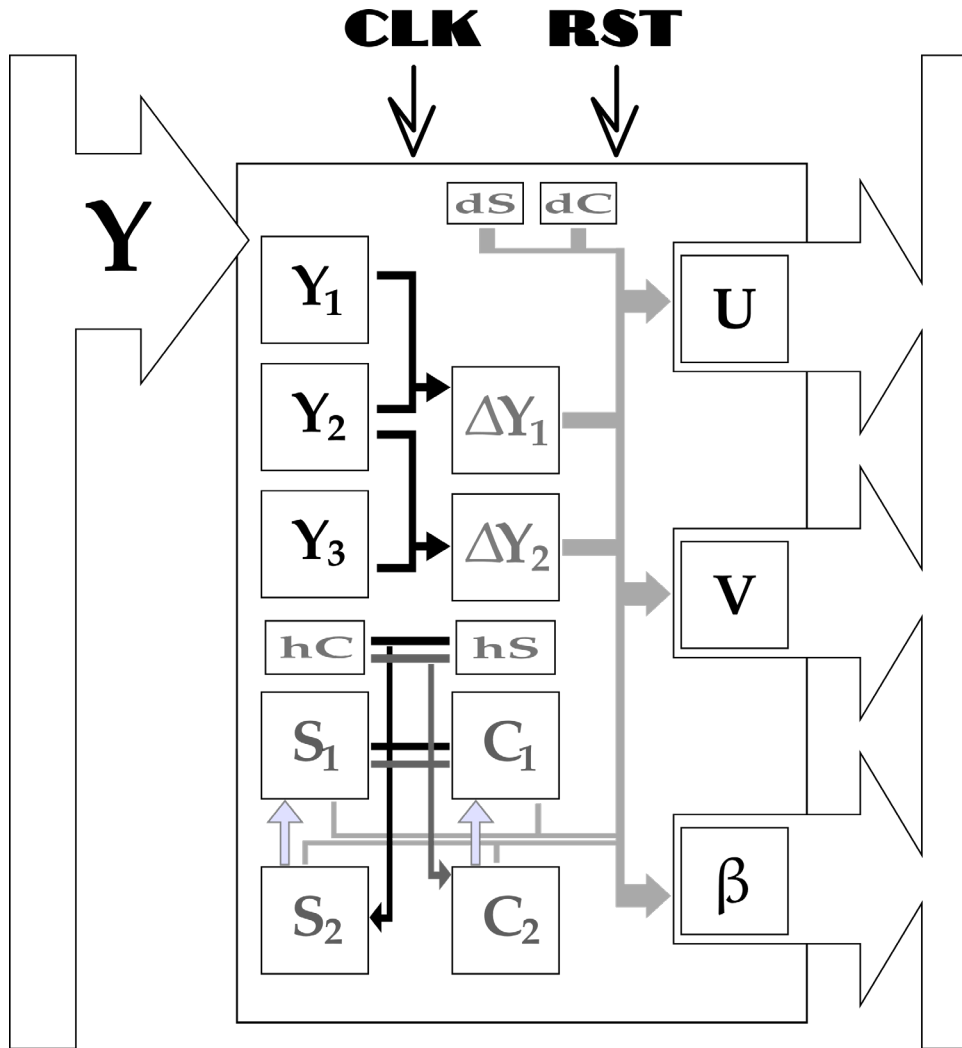


Figure 28: Stream processors draft

The operation cycle of such device can be described as follows: having turned on (what is an equivalent to receiving the resetting signal **RES**), three consecutive values are retrieved from the data bus and loaded into processor register Y_1, Y_2, Y_3 [48]. After them register C_2 and S_2 are cleared and register C_1 and S_1 are set with following values respectively.

$$dC \stackrel{\text{def}}{=} \cos\left(\frac{\Omega}{2}\right) \quad \text{and} \quad dS \stackrel{\text{def}}{=} \sin\left(\frac{\Omega}{2}\right)$$

After them, with every single operation cycle, register S_2 and C_2 will be set with following values

$$\hat{C}_1 hS + \hat{S}_1 hC \quad \text{and} \quad \hat{C}_1 hC - \hat{S}_1 hS \quad \text{where} \quad hS \stackrel{\text{def}}{=} \sin(\Omega) \quad \text{and} \quad hC \stackrel{\text{def}}{=} \cos(\Omega)$$

To complete the operation register U is loaded with $\frac{\Delta Y_1 \cdot \hat{S}_2 - \Delta Y_2 \cdot \hat{S}_1}{4dS \cdot dS \cdot dC}$ and the register V with $\frac{\Delta Y_1 \cdot \hat{C}_2 - \Delta Y_2 \cdot \hat{C}_1}{4dS \cdot dS \cdot dC}$

The β is than $Y_3 - (U \cdot (S_1 dC + C_1 dS) + V \cdot (C_1 dC - S_1 dS))$. With the next operation register S_1 and C_1 are loaded with the values S_2 and C_2 respectively. The Y signal queue is taken the next Y value from the data bus. The values of calculated real and imaginary part of the signal phase U and V as well as β are push out to the output register.

5.6 Simulink™ simulator of the stream processor

Stream phase processors in this work are considered in two variants: TRI processors and LSM processors.

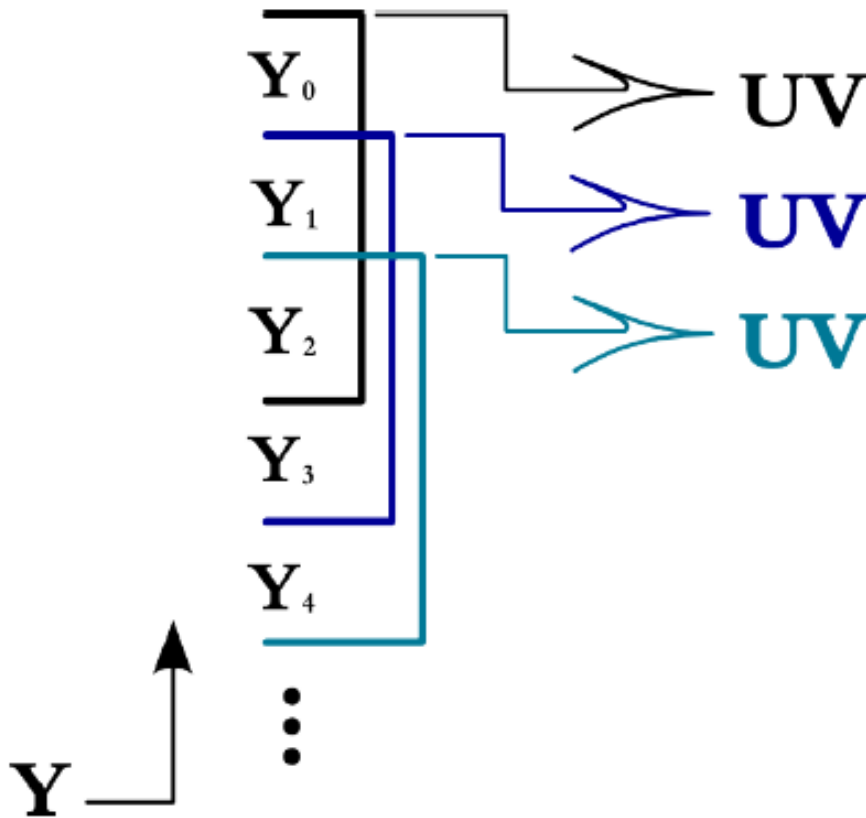


Figure 29: The operation of stream processors

In contrast to the block processor solution, streaming processors download the input data stream and produce U , V phase vector components at once based on several values taken from the data bus (three by TRI type processor and any arbitrary amount in case of LSM). The operation of stream phase processors presents following diagram.

5.7 TRI stream processors

TRI variant is described here and means that, the phase processor needs only to collect three consecutive signal values to calculate the full phase vector values based on three data values as e.g. $Y_1; Y_2; Y_3$. TRI processor solves the task in following form:

$$U = \frac{\Delta Y_1 \cdot \hat{S}_2 - \Delta Y_2 \cdot \hat{S}_1}{2 \sin\left(\frac{\Omega}{2}\right) \sin(\Omega)} \quad (36)$$

$$V = \frac{\Delta Y_1 \cdot \hat{C}_2 - \Delta Y_2 \cdot \hat{C}_1}{2 \sin\left(\frac{\Omega}{2}\right) \sin(\Omega)} \quad (37)$$

where $\Omega = 2\pi \frac{f_w}{f_s}$, $\hat{S}_j = \sin\left(\Omega \cdot \left(j + \frac{1}{2}\right)\right)$, $\hat{C}_j = \cos\left(\Omega \cdot \left(j + \frac{1}{2}\right)\right)$, $\Delta Y_j = Y_{j+1} - Y_j, j = 1, 2$.

The succeeding model produces elements of the phase vector based on the above equations. In addition, this model calculates the value of the expression $U \cdot \sin(\Omega) + V \cdot \cos(\Omega)$ and sets it on the oscilloscope with the value of Y taken from **Signal** together with the deviation value β (bias), as shown in fig.33.

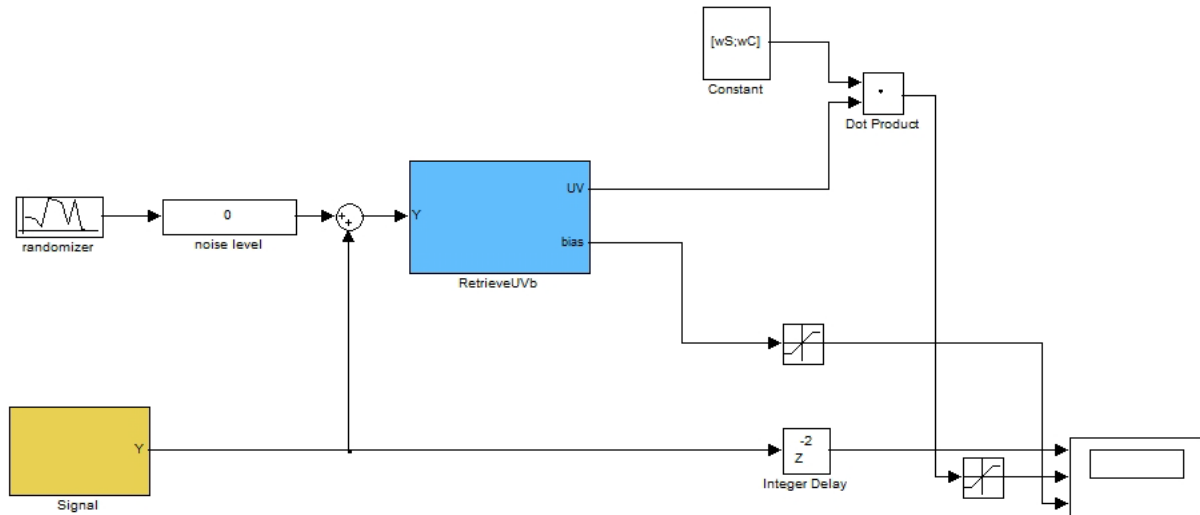


Figure 30: TRI stream processor model

The first segment of the above model - **Signal**, is marked with yellow color – it produces the following Y signature:

$$\sin(\varphi) + \beta, \sin(\Omega + \varphi) + \beta, \sin(2\Omega + \varphi) + \beta, \dots,$$

where φ is the phase. The following diagram shows the construction of this segment.

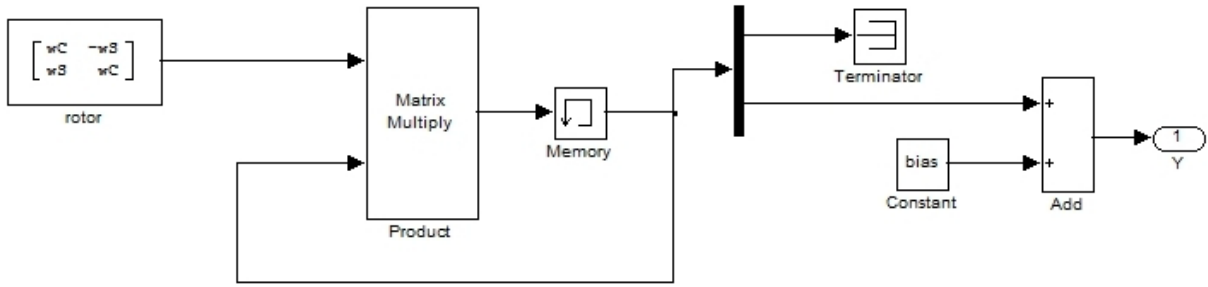


Figure 31: Stream processor TRI – **Signal** (inside view)

The next segment of the model is - **Retrieve UVb**. It is marked in blue. **Retrieve UVb** block gets signal Y values and produces, based on each of its three consecutive values, a phase vector U and V coefficients. Beyond that, it calculates the bias β value, where fig.32 shows the construction of this block. First, the $[DY1 \ DY2]^T = [\Delta Y_1 \ \Delta Y_2]^T$ vectors are constructed based on three consecutive values $Y_1; Y_2; Y_3$ of the signal Y . Next the constant M is multiplied by these vectors, which gives the new $\begin{bmatrix} U \\ V \end{bmatrix}$ vector according to the above models. Constant M was defined in Model Properties as:

$$M = \begin{bmatrix} \frac{\sin(2.5 \cdot \Omega)}{2 \cdot \sin(0.5 \cdot \Omega) \sin(\Omega)} & \frac{-\sin(1.5 \cdot \Omega)}{2 \cdot \sin(0.5 \cdot \Omega) \sin(\Omega)} \\ \frac{\cos(2.5 \cdot \Omega)}{2 \cdot \sin(0.5 \cdot \Omega) \sin(\Omega)} & \frac{-\cos(1.5 \cdot \Omega)}{2 \cdot \sin(0.5 \cdot \Omega) \sin(\Omega)} \end{bmatrix}$$

It should be noted, that the first two values of the vector $[\Delta Y_1 \ \Delta Y_2]^T$ are steady incorrect (these are the transient values), and this involves also the fact, that the first two values of the phase vector real part U and imaginary part V are also incorrect. This are the transient values of the data stream.

In addition, this model calculates the deviation β (bias) according to the formula (35). This equation takes the presented form, because in each step, the calculation of the β value only based on the first three data values of Y is required. The values in the formula are $\sin(\Omega)$ and $\cos(\Omega)$.

$$\beta = Y_1 - (U \cdot \sin(\Omega) + V \cdot \cos(\Omega)) \quad (38)$$

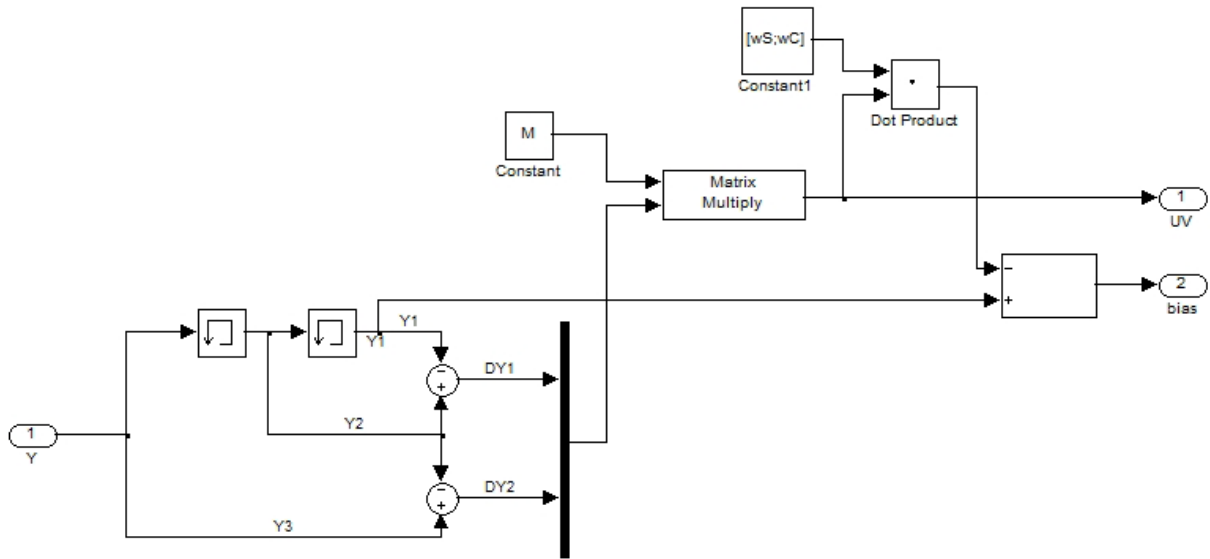


Figure 32: Stream processor TRI – **RetrieveUVb** (inside view)

The result of this model's operation with given $f_s = 1:700$, $f_p = 96$, $\text{bias} = 0:75$, $\text{phase} = 45$, are shown on the oscilloscope diagram fig.33.

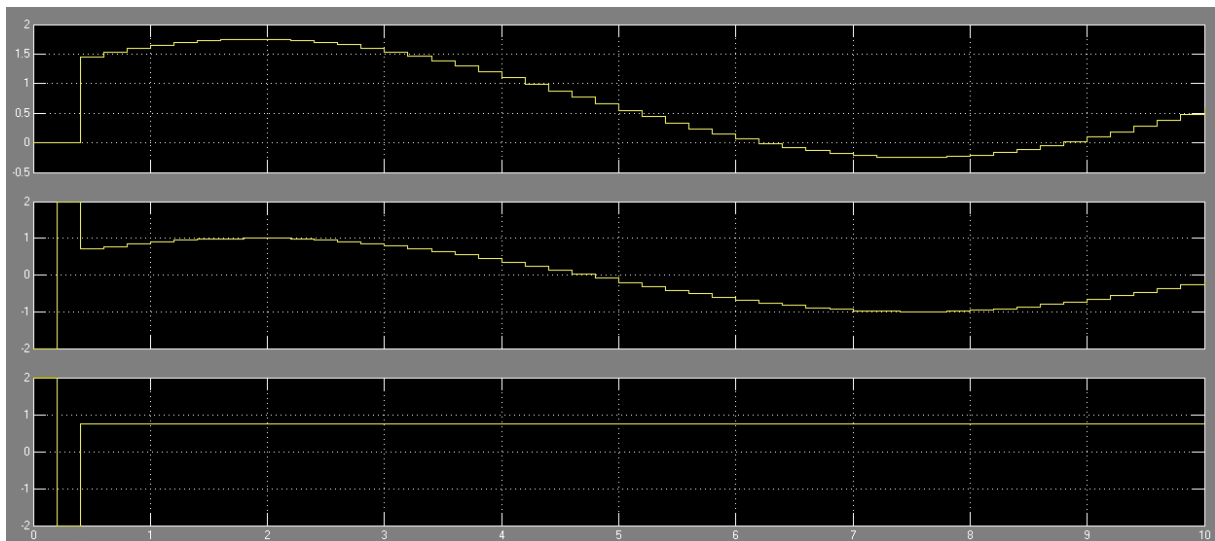


Figure 33: TRI stream processor – Oscilloscope. The transient values are well observed on the left side of the target-performance comparison curves – top diagram is the target curve the middle is the performance curve with the transient behavior and the lower curve is the bias with similar transient behavior (details in text)

5.8 LSM stream processors

The LSM solution, as in the Block Processor case is based on the following formula:

$$\begin{bmatrix} cov(S, Y) \\ cov(C, Y) \end{bmatrix} = \begin{bmatrix} cov(S, S) & cov(S, C) \\ cov(C, S) & cov(C, C) \end{bmatrix} \times \begin{bmatrix} U \\ V \end{bmatrix} \quad (39)$$

Which, after simple mathematical operation, gives:

$$\begin{bmatrix} U \\ V \end{bmatrix} = \begin{bmatrix} cov(S, S) & cov(S, C) \\ cov(C, S) & cov(C, C) \end{bmatrix}^{-1} \times \begin{bmatrix} cov(S, Y) \\ cov(C, Y) \end{bmatrix}$$

$$\begin{bmatrix} U \\ V \end{bmatrix} = \begin{bmatrix} cov(S, S) & cov(S, C) \\ cov(C, S) & cov(C, C) \end{bmatrix}^{-1} \times \begin{bmatrix} S - \bar{S} \\ C - \bar{C} \end{bmatrix} \times Y \quad (40)$$

where $Y = \begin{bmatrix} Y_0 \\ \dots \\ Y_{N-1} \end{bmatrix}$ The following model calculates the values of vector elements phase based on the above equation.

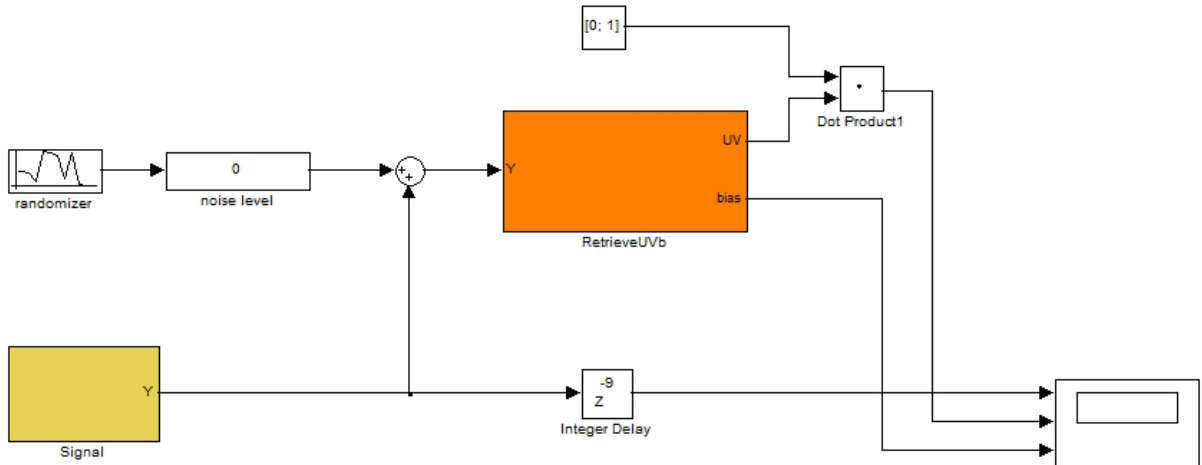


Figure 34: LSM stream processor model

The first segment of this model – named **Signal**, is marked with yellow color – it produces a following Y signal, as already previously mentioned:

$$\sin(\varphi) + \beta, \sin(\Omega + \varphi) + \beta, \sin(2\Omega + \varphi) + \beta, \dots, \quad (41)$$

where φ means the signal phase. The following diagram shows the construction of this block [49].

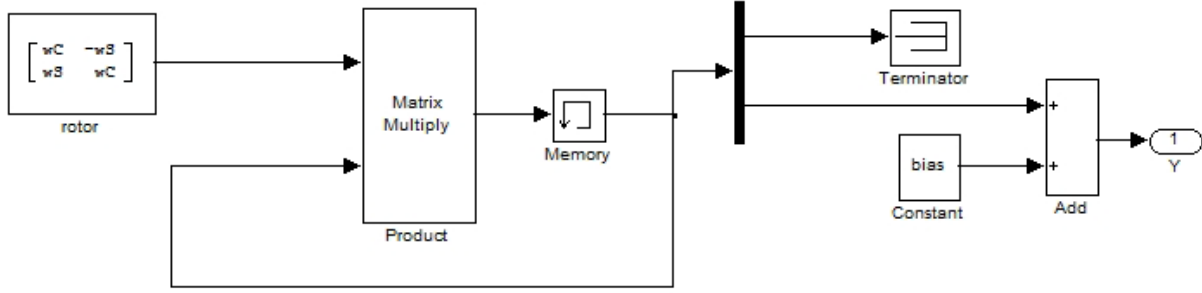


Figure 35: LSM Streamer – Signal (is identical as on fig.21)

Another segment of this model - **RetrieveUVb**, is highlighted in orange color. It gets the Y signal values and returns the U, V elements values of the phase vector. Fig.36 shows the construction of this block. The part **Buffersize**, shown in the left part, is responsible for the production of signal Y “pieces”:

$$[0 \quad \dots \quad 0]^T, [Y_0 \quad \dots \quad Y_{N-1}]^T, [Y_1 \quad \dots \quad Y_N]^T, [Y_{02} \quad \dots \quad Y_{N+1}]^T, \dots$$

The main difference between the **LSM processors** and **Block LSM processors** lies exactly in the way, how the signal fragments (“pieces”) are built.

$$M = \begin{bmatrix} cov(S, S) & cov(S, C) \\ cov(C, S) & cov(C, C) \end{bmatrix}^{-1} \times \begin{bmatrix} S - \bar{S} \\ C - \bar{C} \end{bmatrix}$$

Next the constant M is multiplied by these pieces which gives direct the value of the phase vector $\begin{bmatrix} U \\ V \end{bmatrix}$ according to formula (40). In addition, this model calculates the scalar product value of $\begin{bmatrix} U \\ V \end{bmatrix}$ and $\begin{bmatrix} 0 \\ 1 \end{bmatrix}$ vector.

At each step, it is required to calculate the β (bias) value only for the first signal fragments value (“signal piece”). The scalar product always takes the first **Cyclic clock** value. Then the model calculates the difference between the Y signal value and the calculated scalar product value. This gives the value of the β (bias) deviation for the consecutive signal values Y according to the following formula:

$$\beta = Y_0 - (U \cdot \sin(0) + V \cdot \cos(0))$$

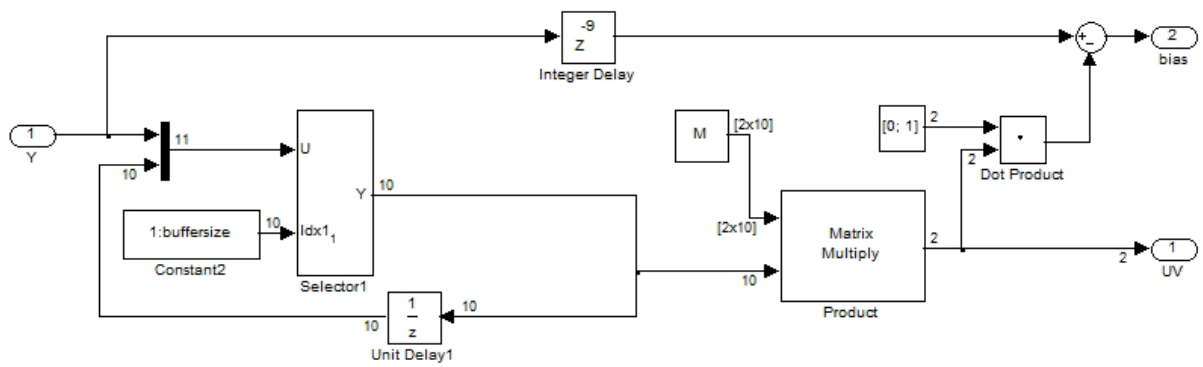


Figure 36: Stream LSM processor – **RetrieveUVb**

Finally, the values of $U \cdot \sin(0) + V \cdot \cos(0)$ are compared to the Y values of the **Signal** and the values of deviation β (bias), which is shown on the oscilloscope figure below for the followed values ($f_s = 1: 700$, $f_p = 96$, bias = 0: 75, phase = 45, $N = 10$).

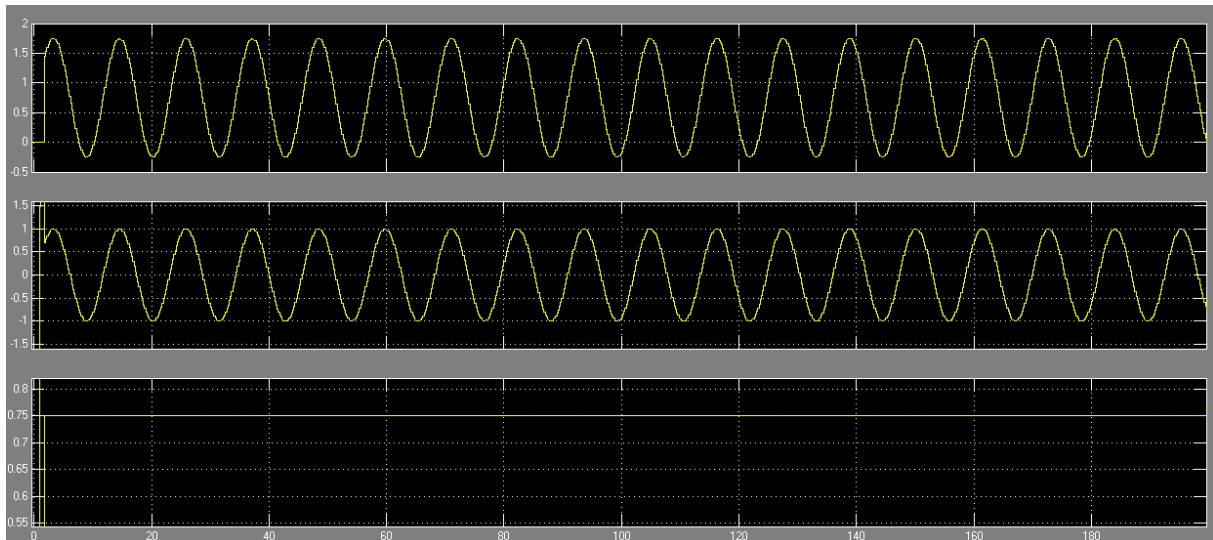


Figure 37: Stream LSM processor – Scope. Some transient values can still be observed on the left side of the signal curves – top diagram is the target curve; the middle is the performance curve with very minor transient behavior and the lower curve is the bias curve with also very minor transient behavior (details in text).

5.9 Averaging module

Both stream processor versions TRI & LSM, can additionally contain an averaging module - **Running average**, marked in gray color on the following block diagrams.

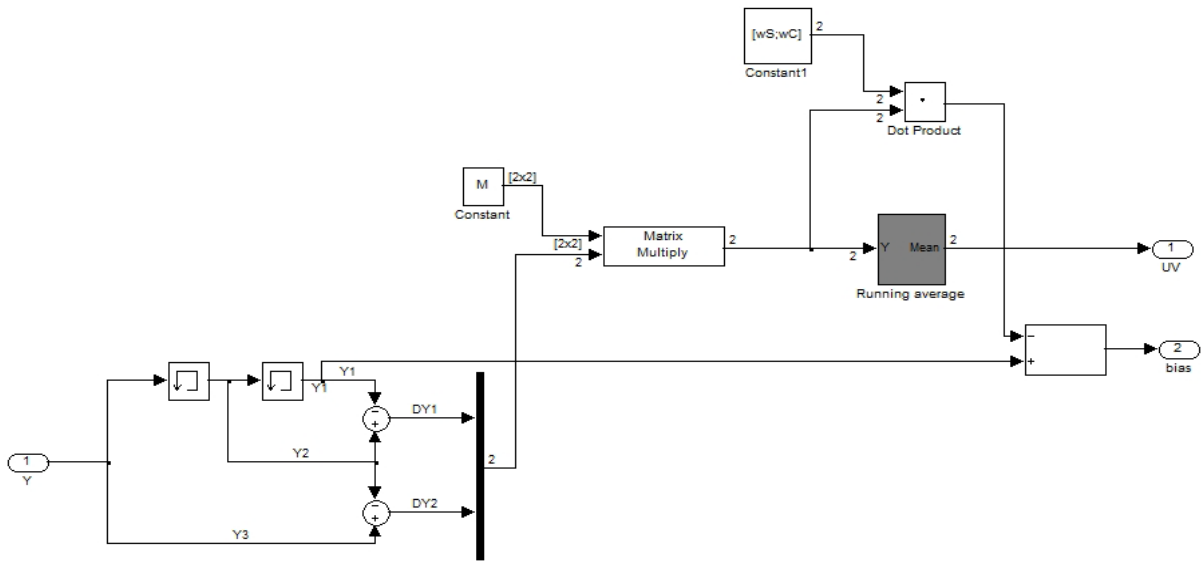


Figure 38: Stream processor TRI (RetrieveUVb) with averaging block

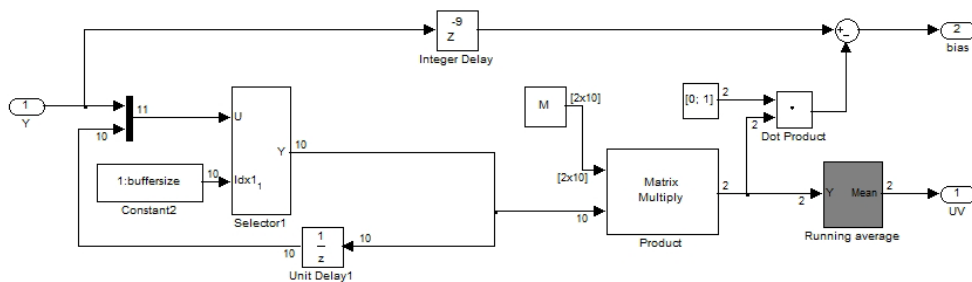


Figure 39: Stream LSM processor (RetrieveUVb) with averaging block

The diagram below shows the construction of the **Running average** module. This module sums n successive elements of the signal Y , and then divides the obtained sum by n . As a result, we obtain an average value of the UV phase vector.

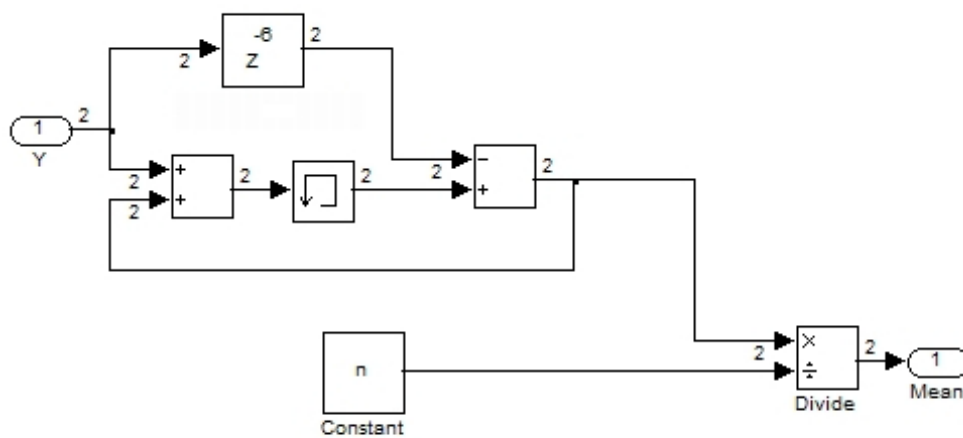


Figure 40: Running average (n=5) - (inside view)

The operation result of the above models, with following input data: $f_s = 1: 700$, $f_p = 96$, bias = 0:75, phase = 45, $n = 5$, can observe on the oscilloscope.

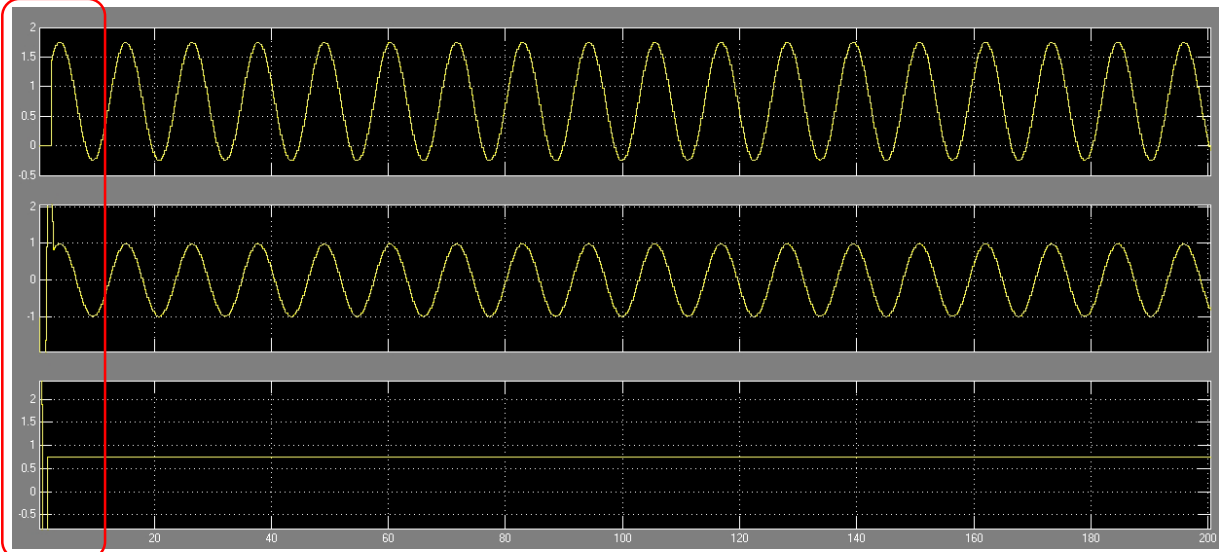


Figure 41: LSM stream processor with $n=5$ averaging – Oscilloscope. The subplots follow the same structure as before. Top diagram is the target curve, the middle is the performance curve and the lower curve is the bias – please take a closer look on the transient response of the system. Next figure shows a zoom look on this behavior.

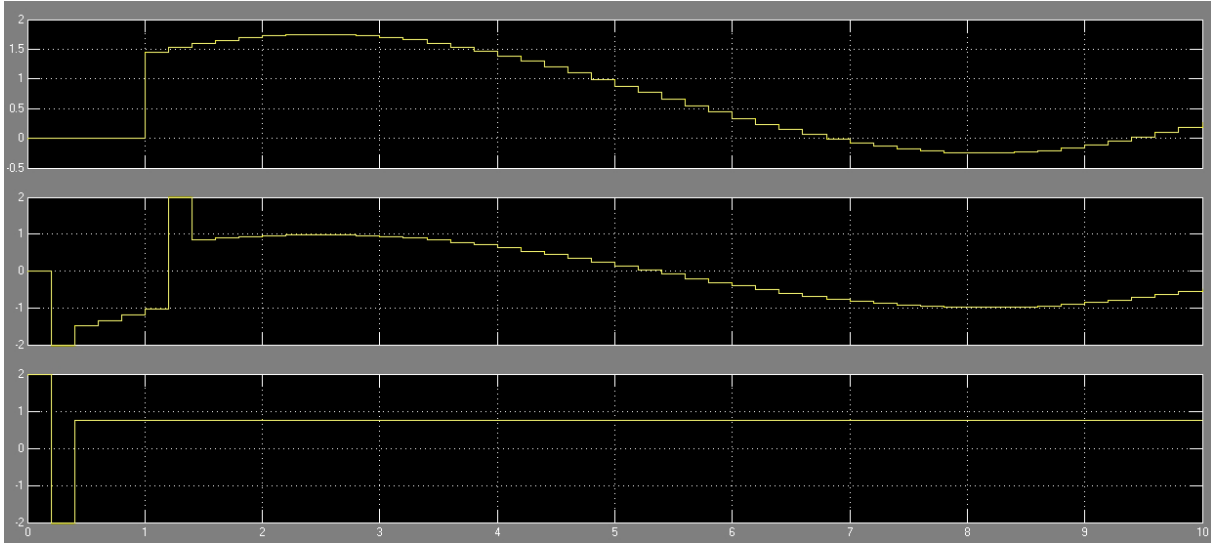


Figure 42: Stream processor TRI with $n=5$ averaging and oscilloscope zoom on the first data points. On the left side of the signal the transient values can be observed. The subplots follow the same structure as before. Top diagram is the target curve, the middle is the performance curve and the lower curve is the bias

6 Chapter 6

6.1 Multispectral – phase vector estimation from polychromatic signal [1]

There is an important relationship between dispersion and attenuation of acoustic waves propagating through a medium which permits dispersion to be calculated from attenuation in cases where direct dispersion measures are not available Eq.45. Propagation speed or, equivalently, times of arriving for an ultrasound pulse or wave packages, can be inferred from phase relations for various frequencies [50] [51]. Since, due to Kramers-Kronig relations, the propagation speeds depend significantly on the frequency of investigated waves, we consider multispectral wave packages of the form $W(n) = \sum_{h=1}^H A_h \cdot \sin\left(2\pi \cdot \frac{n \cdot f_h}{f_p} + \psi_h\right)$, $n = 0, \dots, N - 1$, with appropriately chosen frequencies $f_h, h = 1, \dots, H$, amplifications $A_h, h = 1, \dots, H$, start phases $\psi_h, h = 1, \dots, H$, and sampling frequency f_p . In order to estimate the speed of a sound wave traveling through the human's brain tissue we use two piezoelectric transducers placed at opposite locations of a human skull fig.43, emit a short (approx.100 μ s) ultrasound sampled wave packages by one of them and receive it by the other one, please see fig.43.

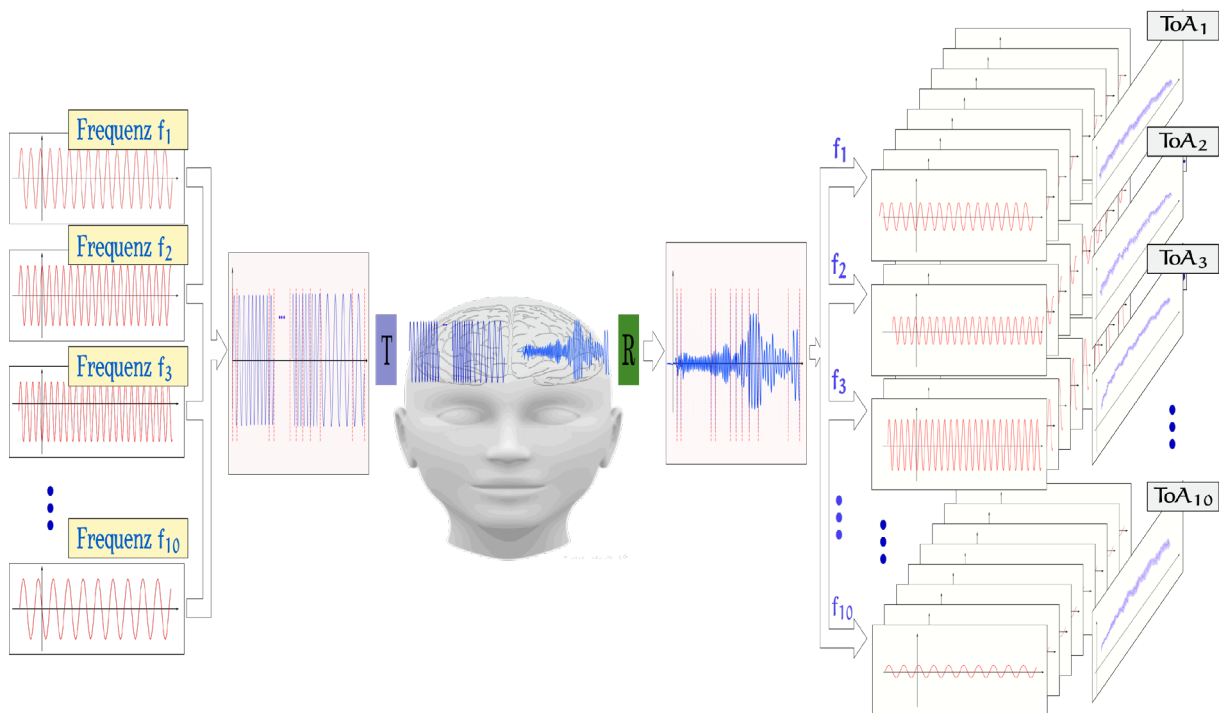


Figure 43: Position of transducers and the shapes of the sent signal and a received one

Given a distance (d) which a wave has to propagate and the time ($T^{(Arr)}$) a wave forehead needs to arrive to the receiver, one could easily compute the velocity as $c = \frac{d}{T^{(Arr)}}$. The problem however is that the time $T^{(Arr)}$ and the distance (d) cannot be properly estimated from just observing the received values because of their severe distortions. Hence one of the possibilities is to fix a time position ($T_X > T^{(Arr)}$) in the observed signal and try to find the best fitting sinus-

like curve in its neighborhood (see fig.44) which can be done with the previously described standard **Least Square Method**.

As a matter of fact, knowing the phase (φ) does not determine the time $T^{(Arr)}$ without knowing the number of wavelengths (K) which fit into d (which in turn depend on the velocity) and inspecting the fig.42 and performing some simple trigonometric transformations, it obtains only that:

$$2\pi \cdot f \cdot (T_X - T^{(Arr)}) \equiv \varphi + 2\pi \cdot K \quad (42)$$

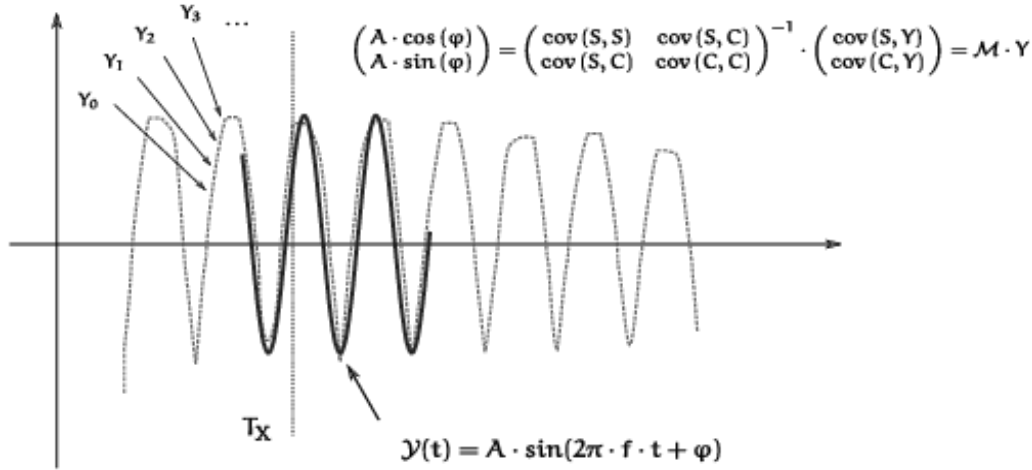


Figure 44: Finding the best fitting sine-like curve

but if we use the equation 42 simultaneously for two frequencies f_1 and f_2 satisfying $T_X \leq \frac{1}{f_2 - f_1}$ (which is a quite reasonable condition) then we get:

$$\begin{aligned} (T_X - T^{(Arr)}) \cdot (f_2 - f_1) &= \frac{\varphi_2 - \varphi_1}{2\pi} + (K_2 - K_1) = \\ &= \left(\left\lfloor \frac{\varphi_2 - \varphi_1}{2\pi} \right\rfloor + \text{mod} \left(\frac{\varphi_2 - \varphi_1}{2\pi}, 1 \right) \right) - \left\lfloor \frac{\varphi_2 - \varphi_1}{2\pi} \right\rfloor = \\ &= \text{mod} \left(\frac{\varphi_2 - \varphi_1}{2\pi}, 1 \right) = \frac{\text{mod}(\varphi_2 - \varphi_1, 2\pi)}{2\pi} \end{aligned}$$

Hence

$$T^{(Arr)} = T_X - \frac{\text{mod}(\varphi_2 - \varphi_1, 2\pi)}{2\pi \cdot (f_2 - f_1)} \quad (43)$$

This attempt, however, requires either sending two pulses with two close frequencies f_1 and f_2 simultaneously or one after another with a delay between them short enough, so that no biologically essential changes could take place in the meantime. The first attempt actually means that the both pulses sum up into one compound wave of the form:

$$W(t) = A_1 \cdot \sin(2\pi \cdot f_1 \cdot t + \psi_1) + A_2 \cdot \sin(2\pi \cdot f_2 \cdot t + \psi_2) \quad (44)$$

with appropriately chosen amplifications A_1 and A_2 . Then, however estimating the required phases may be burdened with quite big inaccuracy since the underlying projection matrix can be poorly conditioned (for details see 6.2). In the other case it can turn out that inaccuracies stemming from rounding projection matrices to the resolution used in the computing software may be essential in relation to the difference $f_2 - f_1$.

Thus, one possible solution for observing the evolution/changes of brain tissue properties is to measure phases (and attenuation) many times in a row and trying to recover a possible evolution of times of arriving due to the Eq.42 with use a kind of ‘unwinding’ procedure see fig.47 and Chapter 4 for more details.

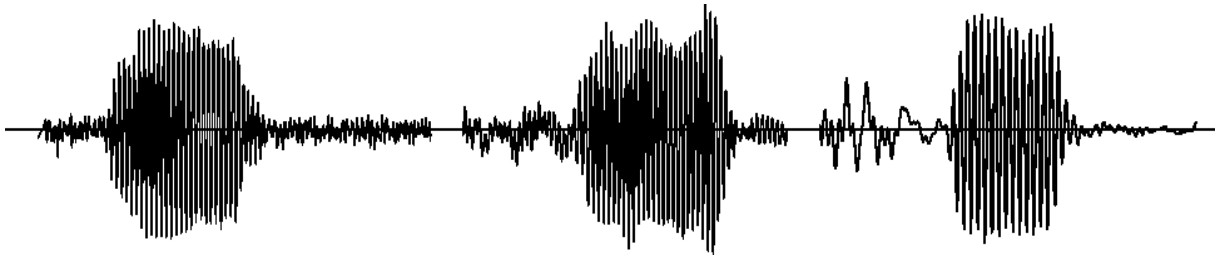


Figure 45: Distortions at beginnings of pulses

According to the Kramers-Kronig relations the velocity of an ultrasound wave changes with frequency (f) according to the attenuation ($\alpha = \alpha(f)$):

$$\frac{1}{c_2} - \frac{1}{c_1} = -\frac{1}{\pi^2} \cdot \int_{f_1}^{f_2} \frac{\alpha(f)df}{f^2} \quad (45)$$

That in particular means that the equality 45 (Eq.20) is not generally valid in a wide range of frequencies and instead we get its generalization²:

$$(f_2 - f_1) \cdot \left(T_X - \frac{f_2 c_2 - f_1 c_1}{f_2 - f_1} \cdot d \right) \equiv \frac{\varphi_2 - \varphi_1}{2\pi} \pmod{1} \quad (46)$$

for any two frequencies f_1, f_2 with $f_1 < f_2$. Moreover, the dependency of wave velocity and frequency suggests that the interrelations between phases for various frequencies may indicate some alarming or at least interesting changes in the investigated tissue.

The above suggests, that we should use many frequencies at once composed in one signal: $W(t) = \sum_{h=1}^H A_h \cdot \sin(2\pi \cdot f_h \cdot t + \psi_h)$. The number H of frequencies which are to be used, their values with relation to the sampling frequency and the values of initial amplifications A_1, \dots, A_H and phases ψ_1, \dots, ψ_H will be discussed later.

² d is the length of acoustic trace here. That is the distance the wave forehead makes between being sent and being received. In the case of standard positions of transducers, it is the human’s head width.

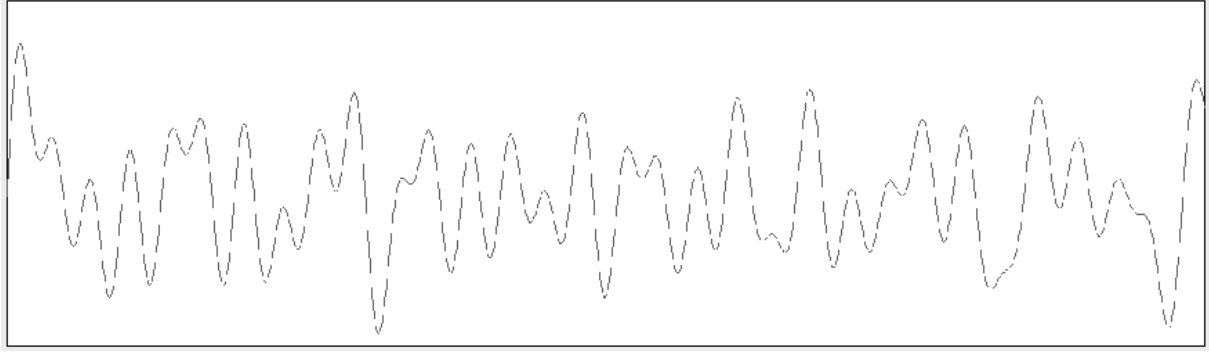


Figure 46: Multispectral signal with H=10 frequencies

6.2 Phase estimating and minimizing the errors

Let $H > 1$ be an integer, $1 \ll F \leq 100$ a rational number (the *sampling frequency*) and $0 < f_1, \dots, f_H \ll \frac{F}{2}$ be rational numbers (*base frequencies*). Let, moreover, $Y = \langle Y_0, \dots, Y_{N-1} \rangle$ be a sequence of reals (*measured signal*). We are concerned with finding such values of $A_1, \dots, A_H \geq 0$, $\beta \in \mathbb{R}$ and $\varphi_1, \dots, \varphi_H \in [0, 2\pi)$ so that the square of the residuum³:

$$\varepsilon^2 = \sum_{n=0}^{N-1} \left[Y_n - \left(\beta + \sum_{h=1}^H A_h \cdot \sin \left(2\pi \cdot f_h \cdot \frac{n}{F} + \varphi_h \right) \right) \right]^2 \quad (47)$$

is as small as possible. This problem can be reformulated as the problem of finding the coordinates $\mathfrak{z}_{-H}, \mathfrak{z}_{-H+1}, \dots, \mathfrak{z}_0, \dots, \mathfrak{z}_{H-1}, \mathfrak{z}_H \in \mathbb{C}$ of projection of $Y \in \mathbb{R}^N$ onto $2H + 1$ - dimensional space generated by vectors

$$\mathbf{e}_{-H}, \mathbf{e}_{-H+1}, \dots, \mathbf{e}_0, \dots, \mathbf{e}_{H-1}, \mathbf{e}_H \quad (48)$$

where

$$\mathbf{e}_h = \langle 1, e^{-2i\pi \cdot \text{sgn}(h) \cdot f_{|h|} \cdot 1F}, \dots, e^{-2i\pi \cdot \text{sgn}(h) \cdot f_{|h|} \cdot (N-1)F} \rangle, \quad (49)$$

$$h = -H, \dots, 0, \dots, H$$

and $f_0 = 0$. That is such $\mathfrak{z}_{-H}, \mathfrak{z}_{-H+1}, \dots, \mathfrak{z}_0, \dots, \mathfrak{z}_{H-1}, \mathfrak{z}_H \in \mathbb{C}$ that

³ technically it is the power of the «noise» in the signal

$$\begin{bmatrix} Y_0 \\ Y_1 \\ \vdots \\ \vdots \\ Y_{N-2} \\ Y_{N-1} \end{bmatrix} = \begin{bmatrix} 1 & \dots & 1 & \dots & 1 \\ e^{+i \cdot 2\pi \cdot f_H \cdot 1F} & \dots & 1 & \dots & e^{+i \cdot 2\pi \cdot f_{-H} \cdot 1F} \\ \vdots & \vdots & \vdots & \vdots & \vdots \\ \vdots & \vdots & \vdots & \vdots & \vdots \\ e^{+i \cdot 2\pi \cdot f_H \cdot (N-2)F} & \dots & 1 & \dots & e^{+i \cdot 2\pi \cdot f_{-H} \cdot (N-2)F} \\ e^{+i \cdot 2\pi \cdot f_H \cdot (N-1)F} & \dots & 1 & \dots & e^{+i \cdot 2\pi \cdot f_{-H} \cdot (N-1)F} \end{bmatrix} \cdot \begin{bmatrix} \mathfrak{Z}_{-H} \\ \mathfrak{Z}_{-H+1} \\ \vdots \\ \mathfrak{Z}_0 \\ \vdots \\ \mathfrak{Z}_{H-1} \\ \mathfrak{Z}_H \end{bmatrix} \quad (50)$$

where $f_0 = 0$ and $f_{-h} = -f_h$, $h = 1, \dots, H$.

Then

$$A_h = 2 \cdot |\mathfrak{Z}_h|, \quad \varphi_h = \text{Arg}(i\mathfrak{Z}_h) \in \langle 0, 2\pi \rangle, \quad h = 1, \dots, H, \quad \text{and} \quad \beta = 2 \cdot \mathfrak{Z}_0 \quad (51)$$

as it is known, the coordinates

$$\mathfrak{Z} = [\mathfrak{Z}_{-H}, \mathfrak{Z}_{-H+1}, \dots, \mathfrak{Z}_0, \dots, \mathfrak{Z}_{H-1}, \mathfrak{Z}_H]^T \quad (52)$$

can be obtained as

$$\mathfrak{Z} = (BB^*)^{-1}B \cdot Y \quad (53)$$

where B is the conjugate transpose of the matrix to the left hand side of the formula 50. Let us also notice that the matrix $M = (BB^*)^{-1}B$ is the Moore-Penrose pseudo-inverse $(B^*)^+$ of B^* [52]. Then also

$$M^+ = (B^*)^{++} = B^* \quad (54)$$

The main problem which we come across here are that the measured values Y are not the signal exact values, which can be for two reasons. The first one is random noise and rounding errors due to amplitude digitalizing. The other can result from frequencies jitter (mostly the sampling frequency) which may occur in the measured signal for unknown reasons.

6.3 Unwinding

As mentioned in the introduction, one possible way of recovering the evolution of phases is a suitable unwinding procedure which adjusts the observed sequence by an appropriate shift in order to avoid jumps which origin from periodical nature of phase. From the theoretical point of view the solution is quite easy. We have the following:

Definition 3

- The residual sequence for $\alpha \in \mathbb{N}_0\mathbb{R}$ is the sequence $\{\alpha\} \in \mathbb{N}_0\mathbb{R}$ such that

$$\{\alpha\}_n = (\alpha_n \bmod 1), \quad n \in \mathbb{N}_0 \quad (55)$$

• The unfolding of α is a sequence $\hat{\alpha}$ defined as

$$(\hat{\alpha})_n = \begin{cases} \alpha_0 & n = 0 \\ \alpha_n - \text{round}(\alpha_n - (\hat{\alpha})_{n-1}) & n > 0, \quad n \in \mathbb{N}_0 \end{cases} \quad (56)$$

Claim 4

1. If $\alpha_n \in \langle 0, 1 \rangle$, $n \in \mathbb{N}$, then $\{\hat{\alpha}\} = \alpha$.
2. If $|(\Delta\alpha)_n| < \frac{1}{2}$, $n \in \mathbb{N}$, then $\Delta(\{\hat{\alpha}\} - \alpha) = 0$.

Proof.

1. Let us first notice, that if $a \in \langle 0, 1 \rangle$ and $N \in \mathbb{N}$ then

$$a - N = [a - N] + \{a - N\} = [a] - N + \{a - N\} = -N + \{a - N\}$$

hence $a = \{a - N\}$. Then also $\{\hat{\alpha}\}_0 = \{(\hat{\alpha})_0\} = \{\alpha_0\} = \alpha_0$ and

$$\{\hat{\alpha}\}_n = \{(\hat{\alpha})_n\} = \{\alpha_n - \text{round}(\alpha_n - (\hat{\alpha})_{n-1})\} = \alpha_n$$

for $n > 0$,

2. We have:

$$\begin{aligned} \left(\Delta(\{\hat{\alpha}\} - \alpha)\right)_n &= (\{\hat{\alpha}\} - \alpha)_{n+1} - (\{\hat{\alpha}\} - \alpha)_n = \\ &= (\{\hat{\alpha}\})_{n+1} - \alpha_{n+1} - (\{\hat{\alpha}\})_n + \alpha_n = \\ &= \{\alpha\}_{n+1} - \text{round}(\{\alpha\}_{n+1} - (\{\hat{\alpha}\})_n) - \alpha_{n+1} - \{\alpha\}_n + \alpha_n = \\ &= \{\alpha\}_{n+1} - \text{round}(\{\alpha\}_{n+1} - \{\alpha\}_n - ([\alpha_{n+1}] + \{\alpha_{n+1}\}) - \\ &\quad - \{\alpha\}_n + ([\alpha_n] + \{\alpha_n\})) = \\ &= -\text{round}(\{\alpha\}_{n+1} - \{\alpha\}_n) - [\alpha_{n+1}] + [\alpha_n] = \\ &= -\text{round}(\{\alpha\}_{n+1} - \{\alpha\}_n + [\alpha_{n+1}] - [\alpha_n]) = \\ &= -\text{round}(\alpha_{n+1} - \alpha_n) = -\text{round}((\Delta\alpha)_n) = 0 \end{aligned}$$

That works perfectly for sequences without or with minor random distortions but for real process sequences, there are sometimes unexpected results (phase jumps). This can be improved by the changing the signal amplitude or the adjusting the gain of the transmitting or receiving channel.

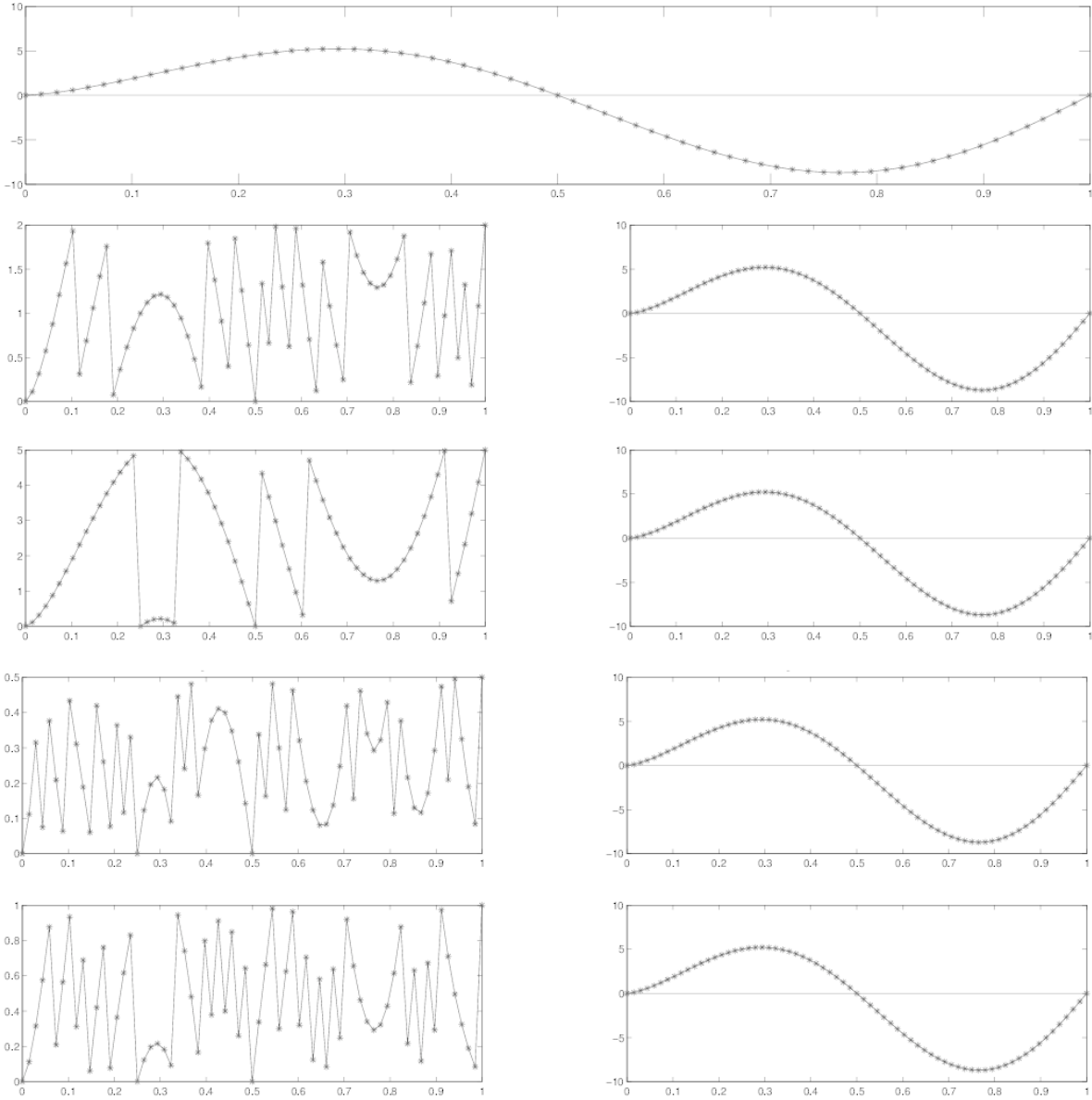


Figure 47: At the top a sample sequence - below to the left, the same sequence taken modulo 2.0, 5.0, 0.5 and 1.0, respectively. To the right there are the results of unwinding the sequence to the left

6.4 Choice of Initial phases

Because of the digital nature of signals used in practice – normally an arbitrary signal made by composition (superposition) of several sinusoid signals is used. This superposition signal is converted with the DAC (digital analog converter) to an analog one before sending. In such a system we have to avoid situations where there are too many regions in a signal with values significantly smaller than the values in other of them. In order to formalise the problem properly, we must introduce some notation first.

Let $A = \{ A_1, \dots, A_H \}$, $A_1, \dots, A_H \in [0, 1]$ be a set of amplitudes, $F = \{ F_1, \dots, F_H \}$ a set of frequencies ($0 < F_h < \frac{1}{2}$, $h = 1, \dots, H$) and $\Psi = \{ \psi_1, \dots, \psi_H \}$ a set of unknown angles ($\psi_h \in (0, 2\pi)$, $h = 1, \dots, H$). We consider a sequence $Y^{[A,F,\Psi]} = \langle Y_n \rangle_{n=0, \dots, N-1}$ given as

$$Y_n = \sum_{h=1}^H A_h \cdot \sin(2\pi F_h \cdot n + \psi_h), \quad n = 0, \dots, N-1. \quad (57)$$

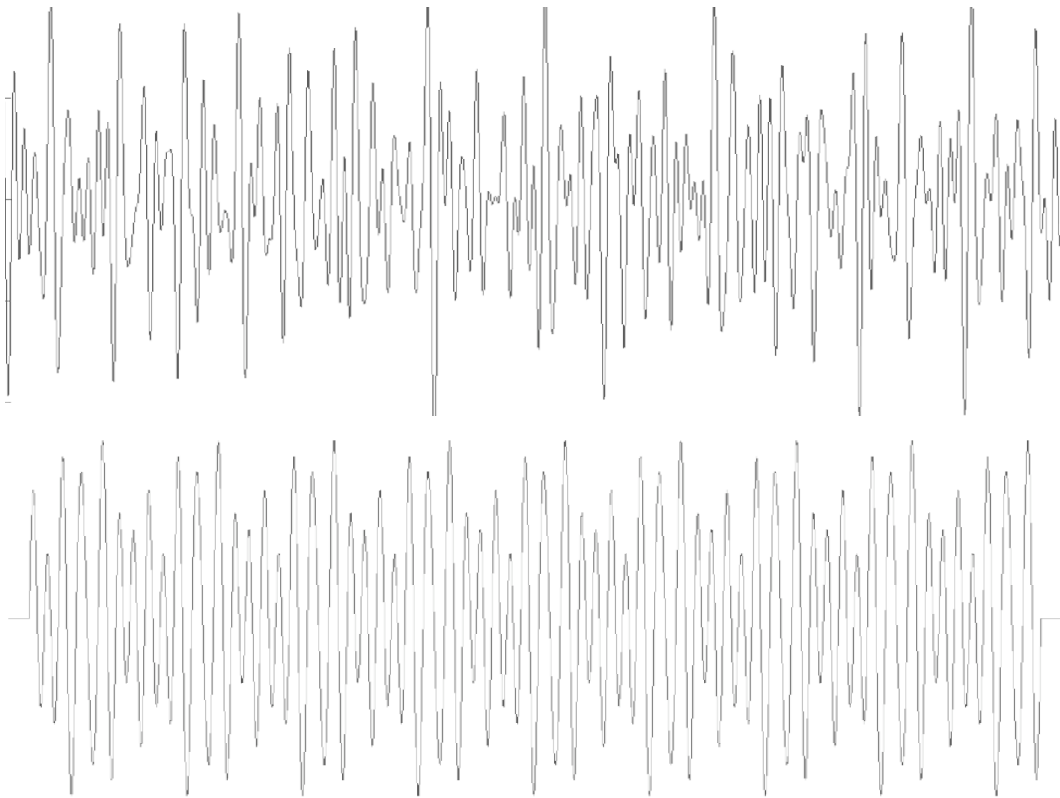


Figure 48: Signals with improperly (top) and with properly distributed peaks (bottom)

Since what is described above has to be physically realisable, it must start from naught, which means that $\sum_{h=1}^H A_h \cdot \sin(\psi_h) = 0$. On the other hand if Ψ is not enough carefully chosen high peaks can appear in the signal (see fig. 48 top) which after setting the signal to e.g. **int16**

numeric type cause frequencies with smaller amplitudes become to much rasterized which in turn may result in huge phase accuracy loss. That way of thinking leads to the following. We need to find such a set Ψ^{ini} of initial phases which produces either:

- The least possible heights of peaks in the signal. That is:

$$\sup_n |Y_n^{[A,F,\Psi^{ini}]}| = \inf_{\Psi} \sup_n |Y_n^{[A,F,\Psi]}| \quad (58)$$

- The least possible distance between maximal and minimal absolute values of local extremes in the signal:

$$\frac{\min_s |\mu_s^{[A,F,\Psi^{ini}]}|}{\max_s |\mu_s^{[A,F,\Psi^{ini}]}|} = \inf_{\Phi} \left(\frac{\min_s |\mu_s^{[A,F,\Psi]}|}{\max_s |\mu_s^{[A,F,\Psi]}|} \right) \quad (59)$$

where $\mu_s^{[A,F,\Psi^{ini}]}$ is the absolute value of the s^{th} peak of $Y^{[A,F,\Psi]}$.

In the restricted case $\psi_h \in \{0, \pi\}$, $h = 1, \dots, H$, the best «brute force» method requires 2^H steps. So even at least approximate solutions of the problem above are of interest in the real system application [50].

7 Chapter 7

7.1 Portable ACG system for animal and human trials

For practical investigation of the method and to fulfill previously described requirements, a portable ultrasound system was designed - transcranial transmission ultrasound (TUS). The system is able to send and receive ultrasonic signal in a wide range of frequencies between 500kHz and 7MHz. One of the very important aspects of this design was to build in automatic signal conditioning and measuring process controls. The external interface provides communication between the TUS electronic module and the host PC (laptop). An insulating transformer separates the electronic module and the host from the external power line 110–240V / \sim 50–60Hz. A dedicated PC application enables the user to carry out measurements, control the parameters of generated signal and save the measurement results. Calculated parameters of ultrasonic signal passing through the medium e.g. brain can be used to evaluate and monitor the physical properties of the brain tissue. The system description below should be interpreted as one of many possible system interpretations and realisation. In this particular system we have successively implemented and tested all previously described signal processing methods.

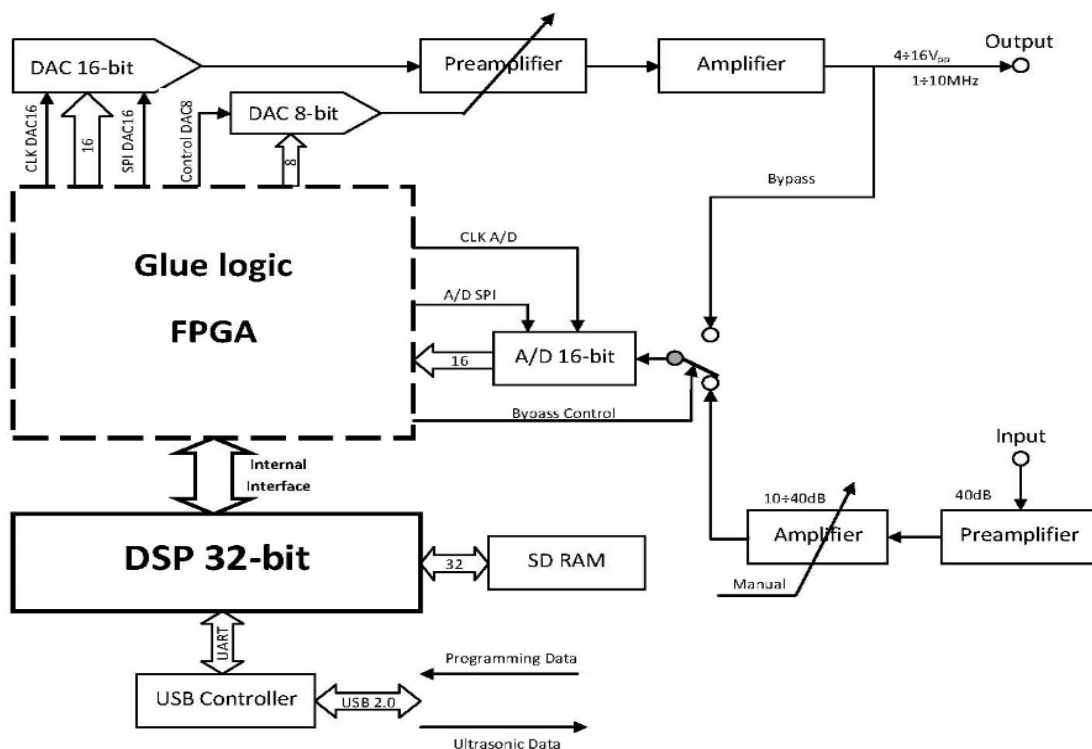


Figure 49: A block diagram of a TUS System. The ultrasound probes are not depicted in this diagram

7.2 System configuration and technical parameters

In its main operating mode, where user defines the shape and duration of the transmitted signal, the conversion between the digital and the analogue domain is realised at a sampling frequency of 96MHz. The circuits control amplification as well the timing of all the necessary operations – it works independently from the host PC. Both the analogue/digital (ADC) and digital/analogue (DAC) converters are working with 16-bit resolution and up to 120MSPS – the dedicated operation frequency is 96MHz. The signal on the receiving side is stored in up to 1M×16bits RAM and after data collection is processed by the connected 32-bit DSP – using the stream processing method, the FPGA processes the data directly, but the amount of the usable frequencies is limited to the used FPGA configuration – Altera, the Cyclone Family. In this work mode, it allows the user to download the raw signal samples into host PC from the module. This depth of storage allows the generating of an arbitrary signal of a length up to 10ms. In a standard application on the human head, signals up to 100 μ s, in a direct transmitting, and up to 180 μ s in reflecting mode can be used. The system we have used in medical experiments has the following parameters:

- Transmitter circuit
 - Output signal type:
 - superposition of up to 16 harmonic sinusoidal components,
 - sweep of up to 3 harmonic components,
 - user-defined (arbitrary mode)
 - Output voltage range: 2–18V_{pp} typical
 - Output voltage adjustment: digital
 - Generation band: 0.5–7MHz
 - Output impedance: < 10 Ω

- Receiver circuit
 - Sensitivity: 1.5mV_{pp} (70 μ V_{pp} with preamplifier)
 - Input impedance: < 10 Ω
 - Maximum amplification: 56dB (83dB with preamplifier)
 - Bandwidth: 0.1–10MHz (0.1–5MHz with preamplifier)
 - Sampling rate: 100MHz – variable setting
 - Amplitude resolution: 16-bits

- Processing
 - Method: digital signal processing
 - Arithmetic type: double precision floating point
 - Measured parameters: β , U, V, bias, cross-correlation

- Work control
 - Control interface: USB 2.0 High Speed
 - Trigger mode: single, continuous
 - Number of frequencies in the measurement profile: 2–16

- Power requirements
 - Power supply: AC 110–240V / 50–60Hz
 - Maximum power consumption: 45W

7.3 System structure and the main board parameters

The main function of the system boards is to run the measurement algorithms and to communicate with the host computer. The main board is assembled on a 6-layer PCB of size 100mm × 160mm. It is equipped with following circuits (according to the block diagram Fig.49):

- analogue front-end circuit,
- FPGA SoC,
- signal DAC (SDAC),
- amplification control DAC (VDAC),
- ADC,
- the DSP subsystem,
- switching regulators.
- Analogue front–end circuits

The systems work in a deep embedded system mode and do not need, during the measurement cycles, any intervention from the host PC. This configuration is the guarantee that the system can operate with stable 30MPS (measurements per second) and can be used in a medical monitoring regime to survey the patient with possible acute cerebral pathologies. To achieve this performance, the internal parts have to be adapted to each other and be fully programmable. The analogue interface circuit consists of transmitting and receiving blocks. The bypass circuit is built in the front module to allow an internal check of all system components before the operation. This circuit consists an attenuator and a reed relay which switches the ADC input to the board output. In standard operation mode, the signal from the analogue to digital converter (ADC) is amplified and its volume is adjusted to fill up the whole bandwidth of the used ADC. The analogue track consists a smoothing and antialiasing filter.

- FPGA system on chip

The FPGA is storing configuration for the in-system generation and processing of the ultrasonic signals. The SoC controls the dedicating received signal samples memory. It is used for storing the transmitting and receiving signals. The dedicating received signal memory is direct accessible to the DSP block. The SoC contains some additional logic to control the functionality of the board.

- Signal DAC

The converter SDAC is used to convert the digital signal generated by the FPGA to the analogue domain. It works in the LVDS standard and has a bit rate of 1920Mbit/s maximum.

- Amplification control DAC

The regulated amplifiers at the transmitting and receiving circuits work on the principle of voltage-controlled amplification. This voltage is controlled by the DAC, called VDAC, with a precision voltage source.

- ADC

The high speed 16-bits / sample ADC converts the analogue signal received from the ultrasonic converter to the digital domain. The digitized signal is transmitted to the FPGA through the DDR bus in the LVDS standard. The bit rate of this bus is up to 1920Mbit/s.

- The DSP subsystem

The computational system of the board is built on TI (Texas Instruments) floating point digital signal processor. The DSP works as the main controller of the system. It initiates and controls the whole measurement process, expect the stream method where the FPGA overdrive the DSP. The cooperation with the SoC is performed using the interrupt system and DMA channels. Data exchange is carried out through 32-bits wide EMIF gate. The gate converts EMIF (External Memory Interface) signals to wishbone bus signals. The main frequency of the EMIF is 75MHz but the transfer is asynchronous which enables a fully embedded measurement process. The signal EMA_WAIT causes the DSP processor to suspend until the gate transfer ends. The DSP used in this configuration has enough calculation capacity to conduct all previously described algorithms in real time.

- Switching regulators

The power supply of the board must provide the all necessary supply to each independent system. It is for very importance that the whole power supply is a medical grade and low EMS radiation.

7.4 Advance TUS system parameters

The advance version of the system presented in fig.49 was used to collect experimental data. A preliminary assessment of the capabilities of the experimental system, to provide diagnostic information relevant to brain injuries, was provided from a set of animal experiments and human studies.

In summary, the results from animal experiments provide a preliminary assessment of the capabilities of a dispersive ultrasound system concept in detecting various cases of brain trauma (i.e. hemorrhage, ischemic stroke) and brain metabolic effects. However, these capabilities need to be demonstrated with clinical trials which may define the most important phase of a development effort in designing a complete dispersive ultrasound system for traumatic brain injury diagnostic applications. In what follows, the signal processing challenges relevant with the dispersive ultrasound system concept of fig.49 are discussed as part of a system development effort.

The biological structures, that are heterogeneous, greatly complicate the measurement process and are described in detail in the previous chapters of this work. But the important parameters affecting the velocity can still be distinguished from precise and sensitive measurements. The elastic constant, the bulk modulus, is frequency dependent and slightly temperature dependent, but the main parameter that changes the velocity of sound is the density, which is also frequency dependent (Kramers–Kronig relation Eq.19, 20 and 45). At this point, it is important to note, that for accurate diagnosis, monitoring of the density fluctuations and their correlation with various conditions of the brain requires estimates of density fluctuations for a wide range of frequencies, to account for dispersive properties. To fulfill these demands, the measurement frequency needs to be increased up to 80MPS as well as the measurement resolution. Fig.50 shows the data stream of such TUS Advance system, where up to 20 frequencies (20 as transmitted profile and 20 received signal – total 40) with the 32-bit phase and 16-bit amplitude resolution can be captured. As it will be presented in detail in chapter 9 of this work, it is enough to record only 3 minutes of the diagnostic session, to capture all the necessary brain tissue alteration – “small acoustic brain map”. At the exact same time, the system can be used for acute monitoring of cerebral pathologies or acute cerebral tissue alteration. For details please see chapter 9. Such advanced systems could easily operate with USB 2.0 interface, with the total data throughput with only $80 \times 40 \times 48$ -bit per second = 154kbit/s, where the USB 2.0 allows for data up to 480Mbit per second.

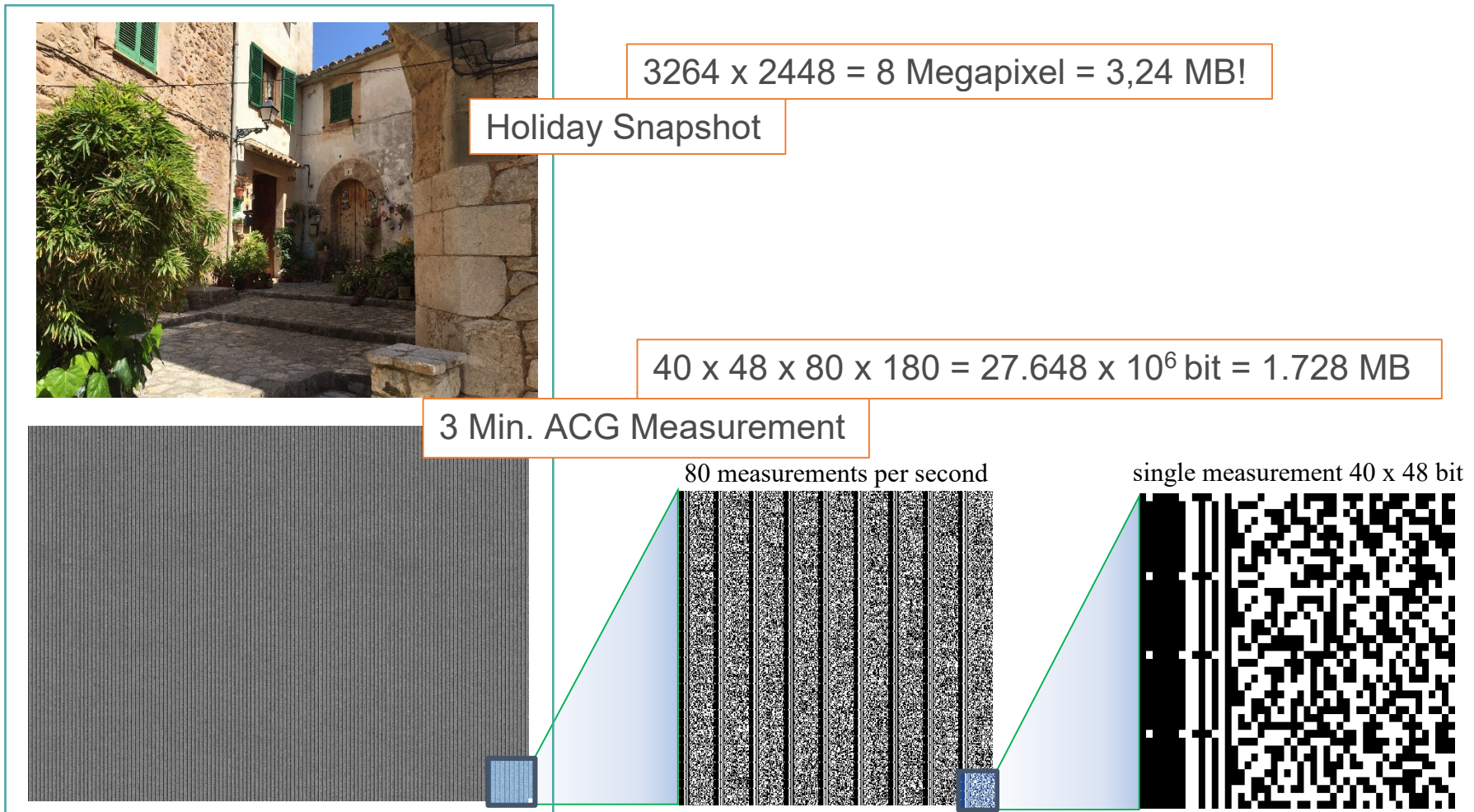


Figure 50: Comparison representation of the total recorded data using the advance TUS system. Considering the value potential, it holds, the data is comparably small in size. The single measurement contains 2x 20 frequencies with recalculated phases (32-bit) and 16-bit amplitude value – 40x 48-bit in total.

8 Chapter 8

8.1 Maximal Stress

A safety study of a novel Transmission Ultrasonic Diagnostic System (TUS) was designed to estimate, “the influence” of TUS on healthy biological tissue in Ovine cranium. In all cases where cardiovascular variations might influence cerebral temperature or the outcome of the TUS recording, animals with high variations ($>$ than 1.5 SDs of the mean) were therefore excluded from the study and replaced. The body temperature was monitored and maintained at $38.9 \pm 0.5^\circ\text{C}$. Experiment: Subsequently the TUS transducer was attached on the temporal bone, once all monitored channels show stable signals, the 6-hour TUS treatment was recorded. The animals are euthanized at the end of the recording period. For those maximum stress experiments a special power TUS was built, where signal parameters overshoot the standard system by more than 10 times. With such configuration the influence, of the new quasi-constant ultrasonic packages on biological cranial tissue was tested [53].

Diagnostic system based on specific, harmonically transmission-ultrasonic signals (TUS)

Acoustic Intensity	$>1120 \text{ mW/cm}^2$
Duration Burst	$600 \mu\text{s} \pm 1\%$
RPF	$>25 \text{ Hz}$
t_delay [μs]	682
Frequency Burst Range:	$0.5 \text{ MHz} < \text{Burst Freq} < 6 \text{ MHz}$

8.2 Summary experimental description

To investigate the influence of the quasi-constant ultrasonic wave on the biological brain tissue, a Maximum Stress experiment was designed, and the necessary local ethical board approval was granted. The experiments were conducted with collaboration with Fraunhofer Institute for Cell Therapy and Immunology IZI in Leipzig, Germany.

Before the experiment, a test plan was prepared in which the experimental conditions were regulated in detail. For diagnostic reasons, a transcranial transmission ultrasound (TUS with $P_0=1.5 \text{ W/cm}^2$ - 10 times higher intensity was used. A blind experiment was made on 10 males and 10 females merino meat sheep which were assigned into 2 groups. The group division took place by computer-generated random numbers (randomization plan) immediately on the day of release. Group 1: control, untreated animals (5 male and 5 female animals each) Group 2: TUS, sonication with new brain diagnostic method based on an ACG (5 male and 5 female animals). After a one-week initiation phase with veterinary supervision an anti-parasitic treatment was released on the animals at least 5 days before the start of the experiment. The clinical neurological examination before the start of the respective experiments showed that no animal has pathological findings and no animals had to be excluded from the experiment. All animal

experiments were conducted in the veterinary faculty in surgical veterinary clinic of the University of Leipzig. After initial anesthesia, intracranial pressure and temperature probe was placed and performed in the animal's brain. Such procedure was used and applied depending on the group for 6 hours ultrasound in-sonification. From all animals the following vital parameters were collected:

- pulse,
- rectal body temperature,
- invasive middle Blood pressure,
- intracerebral temperature and intracerebral pressure.

All measured vital functions parameters were within known reference values (physiological limits). The heart rate and respiratory rate should be considered physiological, taking into account the acute stress during fixation (Table 6).

Subsequently a magnetic resonance tomographic (MRI) examination was performed on the animals. After MRI examination, the animals were euthanised with an intravenous overdose of pentobarbital under general anesthesia. All animals were autopsied - altered organs were preserved when necessary. All brains were preserved and cut in 4 mm slices, from some of them, semi-thin sections were created. Histological staining used conventional staining methods: H & E (Overview), Nissl and Luxol Fast Blue stains was performed. Furthermore, Immunohistochemical method for labeling serum proteins (IgG) was applied too. Using this method, bleeding and cavitation (H & E) can be identified by assessing the incisions as a result. For the analysis of special stains Nissl (neurons) and Luxol (myelin) an added semi-automatic method was used. The analysis of serum protein staining is carried out by Assessment of the incisions (occurrence of positive staining in the brain tissue).

Animal No.	Pulse (/min)	Respiration (/min)	Temperature (°C)	Weight (kg)	OP-Date
1	156	36	38,9	51,3	09.Nov.2012
2	160	48	38,8	41,5	09.Nov.2012
3	88	48	38,9	42,9	23.Nov.2012
4	112	32	38,8	44,4	23.Nov.2012
5	160	48	39,2	51,2	30.Nov.2012
6	152	40	38,6	46,6	06.Dec.2012
7	96	36	38,7	46,0	10.Dec.2012
8	96	36	38,7	42,7	12.Dec.2012
9	168	36	38,8	50,9	17.Dec.2012
10	140	40	38,8	51,4	17.Dec.2012
11	124	52	38,5	35,6	07.Jan.2013

12	116	32	38,4	41,2	07.Jan.2013
13	120	40	38,7	53,8	11.Jan.2013
14	204	44	38,9	49,7	11.Jan.2013
15	144	40	39,0	45,5	28.Jan.2013
16	96	28	37,7	50,0	28.Jan.2013
17	124	36	38,9	69,0	01.Feb.2013
18	100	44	38,7	44,5	01.Feb.2013
19	86	40	39,6	43,6	04.Feb.2013
20	80	32	39,2	48,3	04.Feb.2013

Table 6: Presentation of the release animal clinical parameters

	Pulse (/min)	Respiration (/min)	Temperature (°C)	Weight (kg)
Total Animal Number	20	20	20	20
<i>Minimum</i>	80	28	37,7	35,6
Percentile 25%	96	36	38,7	43,08
Median	122	40	38,8	46,3
Percentile 75%	155	44	39,15	51,13
<i>Maximum</i>	204	52	39,9	69
Mean	126,1	39,4	38,89	47,51
standard Deviation	33,35	6,394	0,448	6,77
<i>standard Error</i>	7,457	1,43	0,1	1,514

Table 7: Statistical data of the clinical parameters listed in Tab.5

8.3 MRI evaluation

After the completion of the treatment phase, all animals were subjected to magnetic resonance imaging Examination (1.5T). The following sequences were acquired: T2_TSE (Turbo-spin echo, anatomical integrity), T2 * (detection of bleeding), T2_Flair (fluid attenuated inversion recovery, differentiation between free and tissue-bound fluid), T1 (Anatomical Integrity), DWI (Diffusion Weighted Imaging, Diffusion Disorders) and PWI (Perfusion weighted imaging, perfusion disorders). The MRI images of the individual sequences were viewed using a DICOM viewer. Possibly occurring damage in the left or right hemisphere was documented by type,

extent and localization. There were no significant differences between the control the TUS treated group and in the group. Fig.51 presents representative MR groups images.

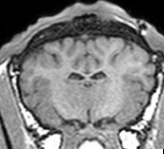
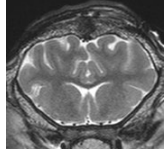
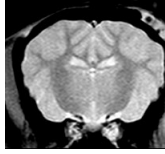
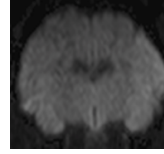
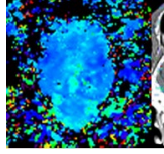
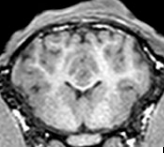
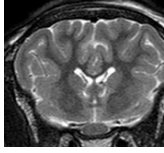
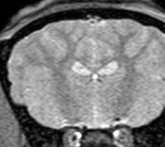
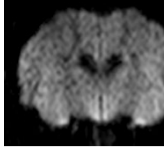
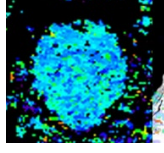
Control					
TUS					
MRI Sequence review	T1: Substance loss or structural changes could not be found in any group	T2_TSE: Water retention or cytotoxic cell edema could not be detected in any group	T2*: no bleeding can be detected in any group	DWI: in no group occurs different diffusion or diffusion disturbances	Left: PWI: (Top view) in no group a reduced perfusion (black) could be detected. Right: PWI overlaid with structural representation of the T1

Figure 51: MRI evaluation, representative data sets, * only the implantation site of the intracranial pressure probe showed locally very limited changes in the T2 * sequence

8.4 Pathological evaluations

Following the MRI examination, the animals were euthanized with an intravenous overdose of pentobarbital under general anesthesia at the Veterinary Anatomical Institute of University of Leipzig. After decapitation and preparation of carotid arteries (arteria carotis communis) on both sides, the head was perfused with 3 litres saline and 15 litres fixing solution. After 24 hours the skullcap was dissected, the brain removed and let free to bond with the fixing solution for another three days. All brains were photographed, weighed and the horizontal and vertical circumference were measured. Subsequently the brains were cut into 4mm thick slats and photographed. Furthermore, the internal organs, were weighed and examined microscopically - in case of changes some samples were collected. The skin was also examined very callously in the TUS probe area.

8.5 Histological evaluation

The prepared brain slices were cut into coded blocks and transferred to paraffin. From the paraffin blocks of the brain lamella 0 (height of the middle cerebral artery), 20 Semi-thin sections (4µm) were created and mounted on slides. There were the following stains carried out: - H & E, 2 sections (overview, bleeding, edema, inflammation, cavitation) - Nissl, 10 cuts (number of neurons) - Luxol-Fast-Blue, 5 sections (myelinisation degree) - Serum proteins - IgG, 2 sections (integrity blood-brain barrier). For the analysis of the special stains Nissl (neurons, gray matter) and Luxol-Fast-Blue (myelin, white matter), semi-automatic methods were used. Analysis of H & E and serum protein staining (occurrence of positive staining in the brain tissue) was performed by meandering, microscopic examination of the sections in a 100x

magnification. In fig.52 you can see the representative photographs of the various colourings shown for both groups. Cerebral haemorrhages were only detected in areas of the cerebral pressure probe in H & E staining according to MRI findings. Swelling, occasional, edema or inflammatory reactions of the meninges are attributed to the implantation of the intracranial pressure probe and are visible only in this area. A cavitation could not be observed in any group. No Nissl staining in the dyeability of the neurons changes are detected. There is no indication of a neural damage in the examined area. A significant difference of the averaged Nissl positive cells per slide between the control group and the TUS-treated group could not be determined, see fig.53A. Also, no indication of injury could be observed in myelination (nerve fiber density) fig.53B. A quantitative analysis of Luxol dye staining area showed no significant difference between the TUS and TOL Control group fig.53B. The IgG staining revealed no blood-brain barrier disorders (outside the area of the brain ICP probe).

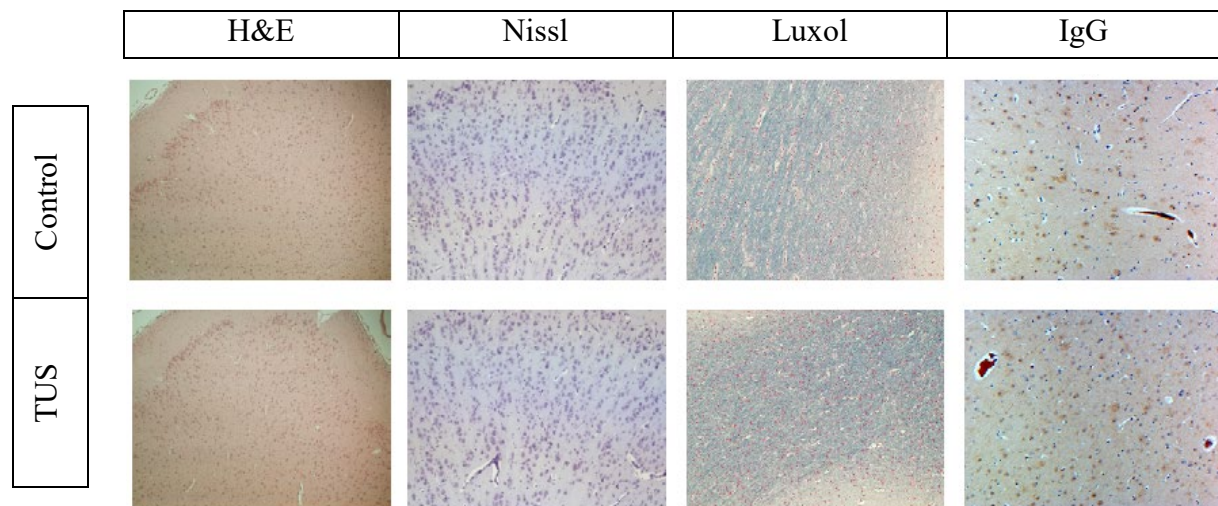


Figure 52: Histological analyzes Sheep brain, representative images of the two groups

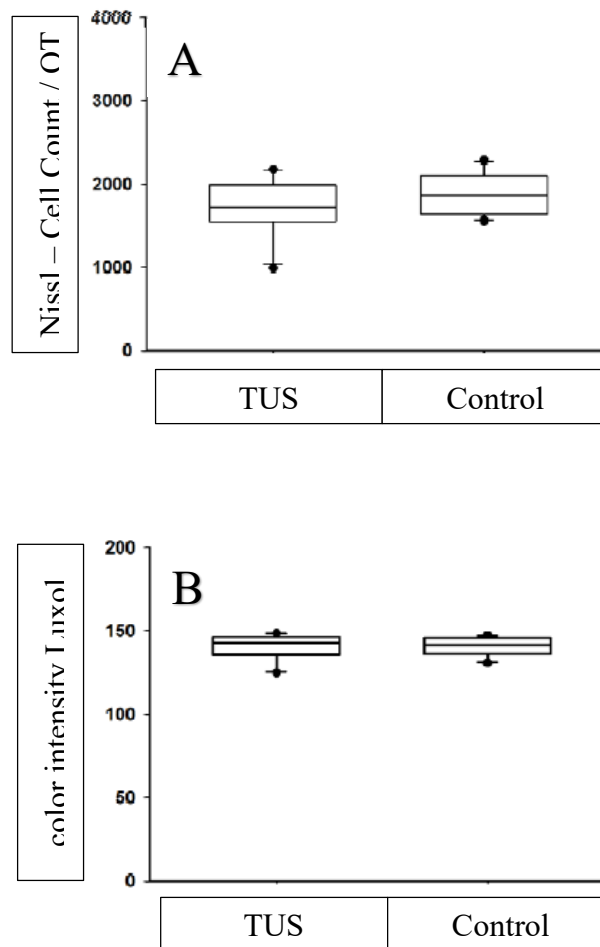


Figure 53: (A) statistical evaluation of the Nissl-positive cell counts (neurons) in Nissl staining. There is no significant difference between the two groups; (B) Statistical evaluation of the stained myelin area in the Luxol stain. There is no difference between

8.6 Summary

In these experiments with 20 merino sheep, (10 male, 10 female) all animals received unrestricted clearance for testing showing the safety of the TUS method. During the experiment, the vital signs brain temperature and intracranial pressure were determined by implantation of a brain probe, as well as pulse, rectal body temperature and mean invasive blood pressure. All parameters showed no significant difference between the control group and the TUS-treated group. After completion of the 6-hour treatment, the animals were subjected to an MRI scan (1.5T). In all acquired MRI sequences, in addition to the changes due to the implantation of the brain probe, no abnormal findings were found in any animal. The subsequent pathological examination of the brains and organs revealed no significant difference between the weight and the macroscopic findings between the two groups. However, in all animals, a pressure point of the skin in the TUS probe area between right eye and ear are observed, indicating a very firm

pressure of the ultrasound probe attributed to the skull. The described histological evaluation of the brains revealed the H & E staining no deviation from the physiological findings except the range of implantation of the brain probe. Furthermore, in the Nissl and Luxol staining no damage to the nerve tissue can be detected in the examined area. There was also no evidence of a blood-brain barrier disorder (IgG staining). In conclusion, it can be stated that during the investigations described and performed here, no significant difference between the control group and the TUS treated group could be detected.

9 Chapter 9

9.1 Portable ACG system for human clinical trials

Objective

Despite intensive research and development over the past decades, the neurological pathologies e.g. strokes, still faces major challenges in terms of clear and rapid diagnosis. Moreover, the accurately neurological diagnosis of a stroke or micro-strokes as WML is time-consuming and medical examination takes place only in central units. Currently, a differentiated diagnosis of a stroke is not possible earlier i.e. at the emergency site or in the ambulance. At the moment, the brain diagnostic takes place through clinical imaging, especially through computed tomography (CT) and magnetic resonance therapy (MRI) in a specialised units or hospital departments. Because in case of a stroke, before a therapy begins, it must be clarified whether the cause of the stroke is a cerebral infarction or a cerebral hemorrhage. As a rule, doctors conduct a computer tomography of the head. Safe differentiation is absolutely crucial to the patient's chance of surviving and recovery. In addition, to ensure the success of the therapy, the treatment of a cerebral infarction must be within a time window of four to five hours after vascular occlusion. Our focus is to use this narrow time window to maximum efficiency. Exactly this optimization is a long-term goal of the ACG method.

Beside strokes, some other hazardous brain tissue alterations, acute or chronic, should be diagnosed with ACG method as well in the near future. Today good diagnosis in the early phases of brain disorders, can only be made by a very experienced specialist, such as a neurologist or psychiatrist, who can interpret a patient's initial symptoms because many brain tissue pathologies are often difficult to detect with standard medical imaging as those minor changes in the brain tissue do not show any discrepancies in picture that was taken. Unfortunately, similarly to mental health problems, other brain illnesses such as traumatic brain injuries are hard to detect or to track with standard imaging or bio-chemical analysis. On the one hand, these are often too minor to occur on the single image, and on the other hand, they are too fast for chemical analysis, thus making it difficult to treat them effectively.

As already stated, the brain is a subject to various injuries with age due to physiological processes and disease. Some of them are acute in nature e.g. a stroke and some are subtle as e.g. white matter lesion. The white matter lesion (WML) or white matter hyperintensities (WMH) can be one of the first signs of micro-damaging in the brain. The implementation of ACG as easy to use method designed to capture states of human brain tissue and its changes was shown in some human medical trials. Such non-invasive examination can be done in the near future by a general practitioner or even the family doctor. Such examinations will take no longer than 3 minutes and record all the complex data needed for a good diagnosis as already stated in chapter 7 with "small acoustic brain map".

9.2 Basic idea of the ACG measurement process



Figure 54: ACG is a set of techniques designed to capture states of human brain tissue and its changes

This approach can be very useful for fast and early detection and diagnosis of chronic slowly developed brain disorders. As one of the first example studies on this medical “pathway” the white matter lesion (WML) or white matter hyperintensities (WMH) diagnostic by the patient with atrial fibrillation (AF) can be shown as very representative.

ACG signals and Magnetic Resonance Imaging (MRI) results were compared to WML assessment in the brains of patients with atrial fibrillation (AF). The study included 97 patients (age 66.26 ± 6.54 years) with AF. According to MRI data, the patients were assigned into four groups depending on the number of lesions: L0 - 0 to 4 lesions, L5 - 5 to 9 lesions, L10 - 10 to 29 lesions, and L30 – 30 or more lesions. ACG method clearly differentiate the groups L0 (with $0 \div 4$ lesions) and L30 (with more than 30 lesions) of WML patients. Fisher’s Exact Test shows that this correlation is highly significant ($p < 0.001$). The new, easy and cost-effective method for detecting WML can be used in patients with atrial fibrillation. This study was performed in accordance with the Declaration of Helsinki and approved by the Human Investigation Review Committee at the Warsaw Medical Chamber. Each participant provided written informed consent to participate in this study. More information about the medical studies can be found in the relevant medical publications [54] [55] [56] [57] [58].

To give just one example, during one of the clinical sub-studies which included 55 patients with AF; the study population had a mean age of 66.1 ± 6.7 , a CHA2DS2, VASc of 2.5 ± 1.3 , and a mean HAS-BLED of 1.65 ± 0.9 . The recorded data consisted of 55 cases grouped by factor

variable nLF (number of lesions) and described by 266 variables. These basic types of variables consist of the physical signal values like: absorption, attenuation, amplitude, relative sound velocity, transition time through the head. All were used for the 10 different frequencies. The preliminary analysis using statistical usability consisted evaluation of these all 266 variables. The next step of evaluation was, using statistical learning procedure GBM (General Boosting Machine) to verify which variables are the most informative for the classification of the number of the lesion groups (nLF factor variable). The classification procedure was constructed by using these variables and is sketchy and is described in the next point.

9.3 First analysis: Classifying with the aim 4 groups

The main function of the system boards is: to run the measurement algorithms and to the cases are described by 266 variables. Two variables are connected with general information: gender and age of case. The ultrasonic measurements represent than 264 variables. These variables consist of 7 basic types of physical signal description. There are:

- **Alpha:** it is also called absorption coefficient. It's a physical value of damping per Length unit.
- **Attenuation:** is a physical value which is direct connected with Alpha. All in all, this value say how great is the signal damping for this particular patient and frequency.
- **AMP:** is the plain amplitude of signal.
- **Velocity:** is the velocity of sound in head.
- **ToA:** this is the time it takes for the signal to pass through the head.
- **AlphaC:** is a product between Alpha and Velocity of sound with the aim to become independent from the size of head.
- **QuasiC:** is the resultant speed based on a reference speed.
- **AlphaQuo:** is a calculated between Alpha of different frequencies with the aim to become independent from the size of head and to show relation between absorption coefficients of different frequencies.
- **ElastQuo:** is shows the elasticity of head in a quotient, between different frequencies.

Each of the variables were measured for the given 10 frequencies. The used frequency band was from 0.5 MHz up to 2.5 MHz and almost equidistant in frequency step. Two variables are calculated as ratio between the frequency pairs, AlphaQuo and ElastQuo. This was made for different frequencies and therefore there only 9 values instead of 10. Each of these time series are described by 3 quartiles (25%, 50% and 75% percentiles). The sufficiency of this quartile's representation was proven statistically using principal components method, for discrimination between number of different groups lesions. The preliminary analysis consisted in using statistical usability evaluation of the 266 variables. The evaluation was provided to verify which variables are the most informative for the classification of the data into the number of lesions groups (nLF factor variable). Using statistical learning procedure GBM (General Boosting Machine) the 1000 classification trees were constructed. This method for every case gives four

probabilities. The maximum of these four gives the group membership. In the given cases the result is like in fig.55. There are four clearly separated groups. The cases with smallest number of lesions (from 0 to 4) form the group L0. The next group, L5 collect the cases with 5 up to 9 lesions. The third group collect the cases with 10 up to 29 lesions. The group with 30 or more lesions forms the group L30. The groups are almost equinumerous: L0 consist of the 14 cases, L5 12 cases, L10 14 and L30 15 cases.

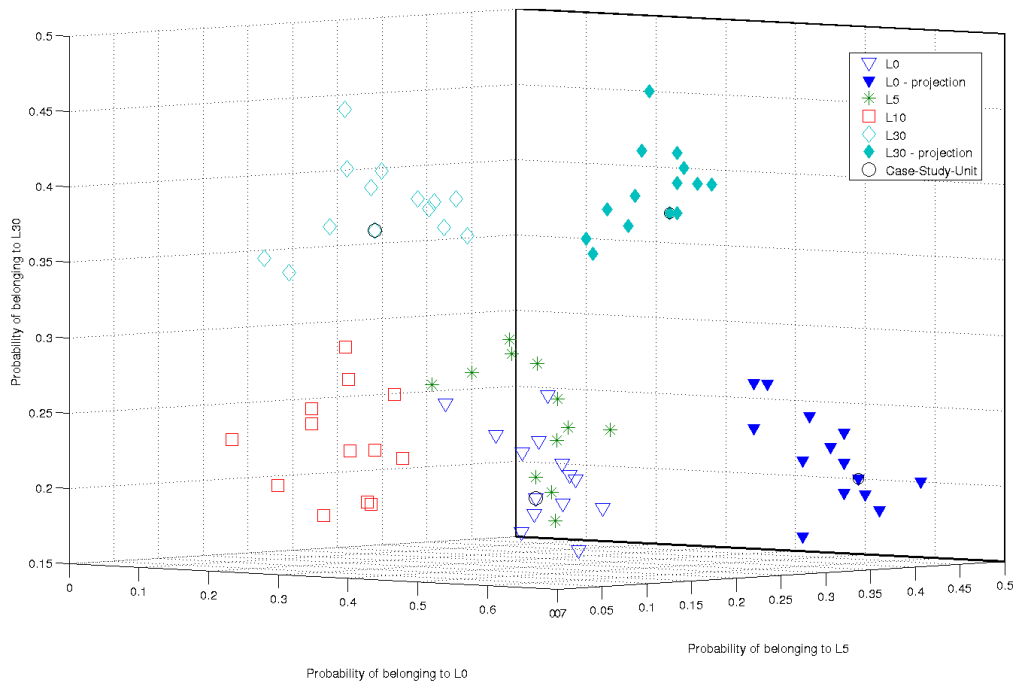


Figure 55: Result of the GBM-Classification. The points are represented by the classification probability to the groups L0, L5 and L30. The filled symbols represent the projection of the points from groups L0 and L30 on the plane L0-L30 probability

All in all, the most informative frequencies are the lower (0.5 MHz – 0.9 MHz) and low middle (0.9 MHz – 1.1 MHz) frequencies.

Student distance values greater than 2 are significant on $p < 0.05$ level. The values are in table 8 shown the variables with highest Student distance. Column p value represents the significance level of the classification, using this particular variable.

	Variable	Student Distance	p-value
1	“AlphaQuo_25_3” 25% percentile of AlphaQuo of lower frequency (Frequency 3) in frequency-band	2.32	2.0%
2	“QuasiC_50_4” 50% percentile of QuasiC of lower frequency (Frequency 4) in frequency-band	2.31	2.1%
3	“AlphaQuo_50_3”	2.30	2.1%

	50% percentile of AlphaQuo of lower frequency (Frequency 3) in frequency-band		
4	“AlphaQuo_75_3” 75% percentile of AlphaQuo of lower frequency (Frequency 3) in frequency-band	2.29	2.2%

Table 8: Statistical data - Student distance of a selection of variables

Some other, probably more relevant depiction of the results, is the 2D plot of the two most discriminative variables, please see fig.56 and fig.57.

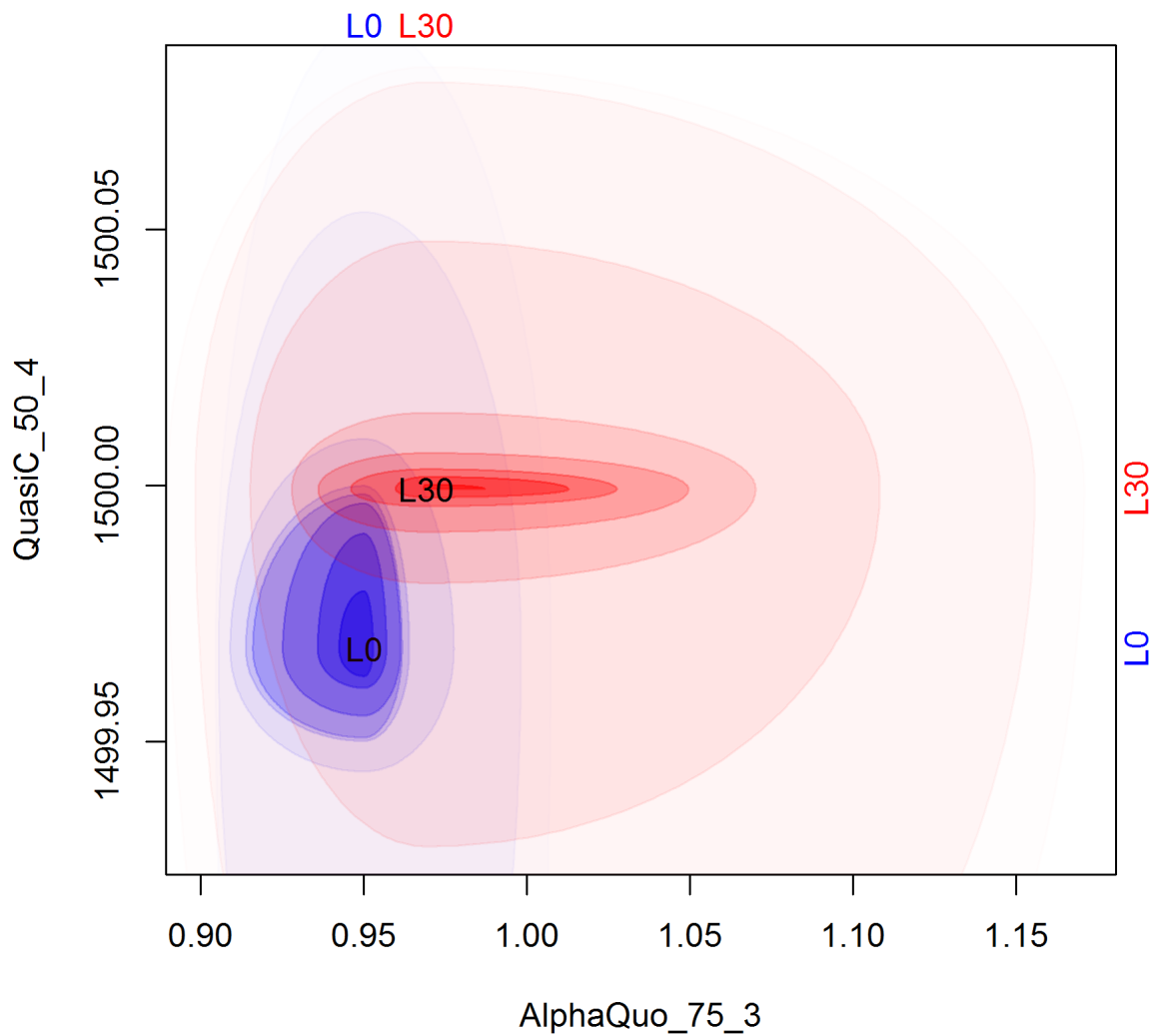


Figure 56: Comparison of varying force of two most discriminative variables: AlphaQuo_75_3 and QuasiC_50_4: The most extremal groups L0 and L30 are easily distinguishable

The colors represent the groups of lesions: L0 – blue, L5 – green, L10 – magenta, L30 – red. The points L0, L5, L10, L30 represent the medians of the variables. The contours with different color intensity contain from most typical (the strongest intensity) up to less typical data (the weakest intensity). Each contour contains the same number of recorded values

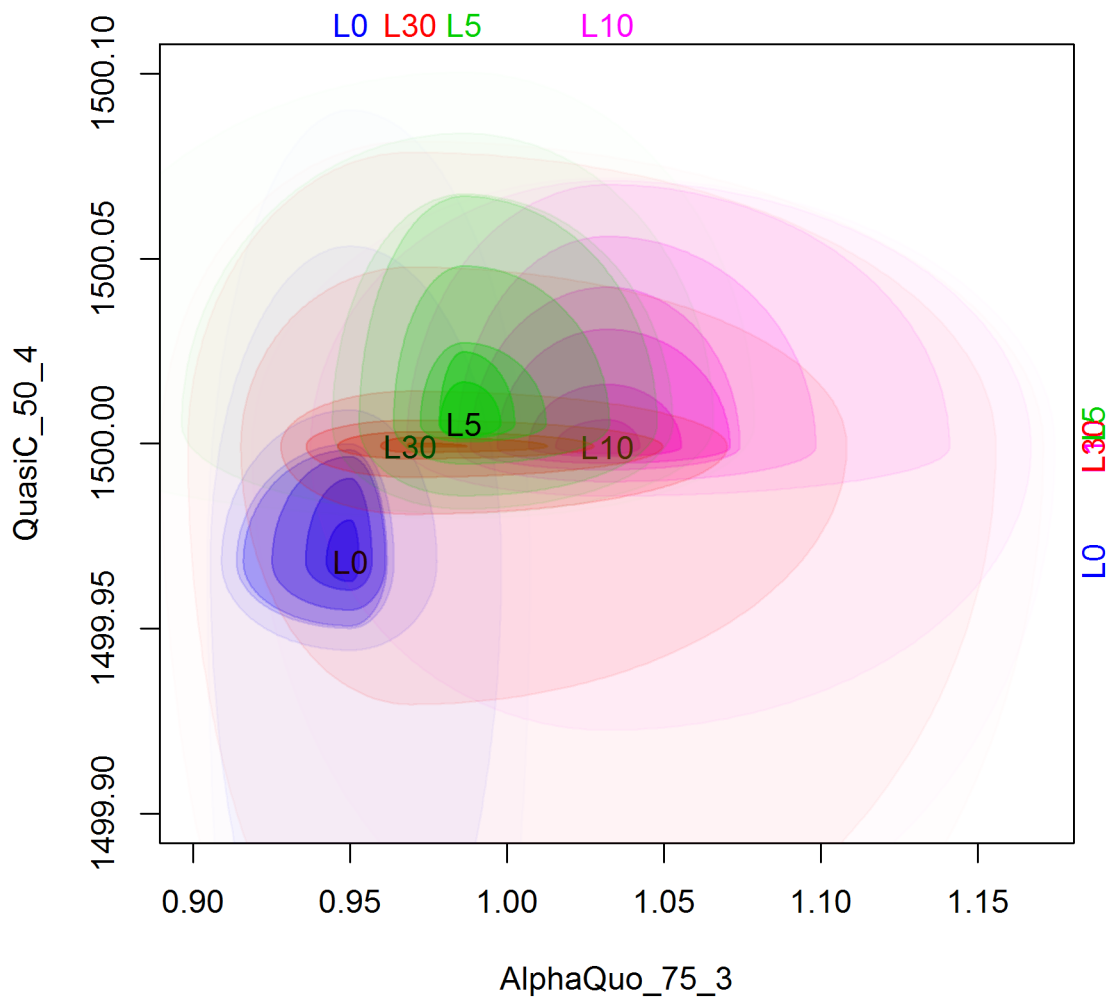


Figure 57: Density distribution of two most discriminative variables: AlphaQuo_75_3 and QuasiC_50_4.

9.4 Advance dynamic application for septic encephalopathy diagnosis

The second approach, or the second possible medical pathway, is using ACG for real-time monitoring of acute brain pathologies at the patient's bedside. One of the best examples are the clinical studies conducted with the University Medical Clinic in Rostock, Germany. The patients had severe septic shock with septic associated encephalopathy (SAE). The incidence and severity of septic encephalopathy (SE) are prognostically relevant and represent a common and serious neurological complication of severe sepsis [59]. Sepsis is often complicated by an acute and reversible deterioration of mental status, which is associated with increased mortality and is consistent with delirium but can also be revealed by a focal neurologic sign. Sepsis-associated encephalopathy is accompanied by abnormalities of electroencephalogram and somatosensory-evoked potentials, increased in biomarkers of brain injury (i.e., neuron-specific enolase, S-100 β -protein) and, frequently, by neuroradiological abnormalities, notably leukoencephalopathy. Its mechanism is highly complex, resulting from both inflammatory and

non-inflammatory processes that affect all brain cells and induce blood-brain barrier breakdown, dysfunction of intracellular metabolism, brain cell death, and brain injuries. Its diagnosis relies essentially on neurologic examination that can lead one to perform specific neurologic tests. Electroencephalography is required in the presence of seizure; neuroimaging in the presence of seizure, focal neurologic signs or suspicion of cerebral infection; and both when encephalopathy remains unexplained. In practice, cerebrospinal fluid analysis should be performed if there is any doubt of meningitis. An exact and direct diagnosis is very complicated as an exclusion diagnosis and makes an early diagnosis difficult.

Using the ACG method, density and elasticity changes of cerebral tissue can be detected non-invasively and, on the bedside, thus demonstrating pathologies. In a pilot study in patients with septic shock, the importance of the ACG method should be evaluated as a possible new diagnostic tool for the SE using the deep data learning and advance signal processing [60].

The methodology in this prospective clinical study at the University of Rostock, 20 intensive care patients were observed over a period of 28 days. Ten surgical patients with septic shock and clinical suspicion of SE (sepsis group: SG) were compared with ten non-septic and non-delirious postoperative patients (control group: CG). The SG received ACG measurements on days 1, 3, 7 and 14. The ultrasound probes were placed on both sides of the skull behind the ears for the ACG measurement. 10 measuring cycles of 3 minutes were recorded (10 different frequencies from 0.5 MHz to 2.5 MHz). At the same time, the neurological status, the Delirscores ICDSC (the grade of the patient's deliriousness) and CAM-ICU scores, the RASS score for sedation depth, the APACHE II and SOFA score, and laboratory parameters were collected. The same was true for the control group - but with ACG measurements on days 1 and 3. A positive opinion from the Ethics Committee of the University of Rostock was available before the study started and the study was registered (A 2016-0026 / ClinicalTrials.gov: NCT03173196). The patient data were statistically evaluated in the absence of normal distribution with the Kruskal Wallis and following the Mann-Whitney U test. Symptoms (CAM-ICU) were analysed between the groups with the Chi-square test. The results of ACG measurements and clinical measurements were correlated with the Pearson test. Previously, the measurement data were processed by two methods: first, deterministic (dimensionality of the data) and secondly, stochastic (genetic algorithm).

The clinical evaluation results show a very positive conclusion. Hospital survival was 90% in SG. All patients in the CG were negative for CAM-ICU and ICDSC scores were 0 at all time points. In SG, all patients were CAM-ICU positive at inclusion; On day 3, 9 patients were positive for CAM-ICU (day 7: 8 positive, day 14: 7 positive). The median of ICDSC scores in the SG was 4.00 at inclusion; 4.5 on day 3; 4.0 on day 7 and 5.0 on day 14. All patients had RASS values between -3 and +3 at the time of measurement. The best correlations between the results of the ACG measurements and the clinical parameters were found in the SOFA score, and somewhat weaker in the ICDSC score. The parameters lactate, PCT, creatinine and bilirubin correlated significantly less well with the results of ACG measurements. The evaluation by genetic algorithm showed better correlations which are summarised in table 9.

Parameters	Correlation coefficient based on	
	<i>dimensionality</i>	genetic algorithm
SOFA	0.66	0.82
ICDSC	0.45	0.75
Laktat	0.32	0.75
PCT	0.17	0.82
Kreatinin	0.13	0.70
Bilirubin	0.45	0.78

Table 9: Comparison of the Pearson correlations of the dimensionality parameters with the major components obtained by genetic algorithm and the clinical parameters

CAM-ICU: Confusion Assessment Method for the Intensive Care Unit
 ICDSC: Intensive Care Delirium Screening Checklist
 PCT: Procalcitonin
 SOFA: Sepsis-related Organ Failure Assessment

As shown in table 9 the best correlation for both strategies is achieved via correlation of ACG data with SOFA score. Figures 58 to 61 visualise this correlation. The correlation of the genetic algorithm (GA) is stronger what can be easy take from those pictures. In both cases, it is possible to distinguish the two patient groups, but in the case of genetic algorithm the separation is somewhat clearer [61] [62].

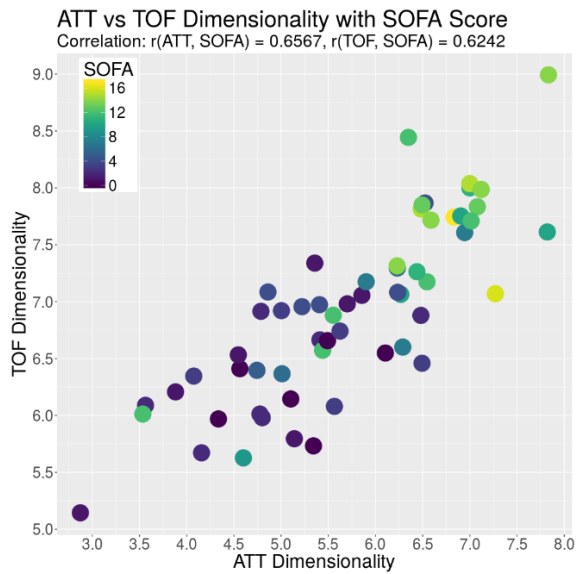


Figure 58: Dimensionality plot of the attenuation (ATT) versus time of flight (TOF). Every dot represents one patient on one day, the color represents the SOFA score of that patient on that day

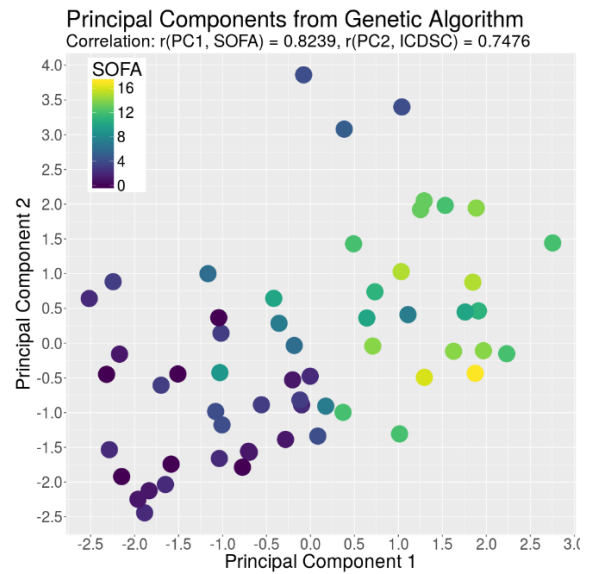


Figure 59: Plot of the principal component derived by the genetic algorithm (GA) based on the SOFA score on the X-axis and the principal component derived by the GA based on the ICDSC on the Y-axis. Every dot represents one patient on one day, color coded with the SOFA index on that day

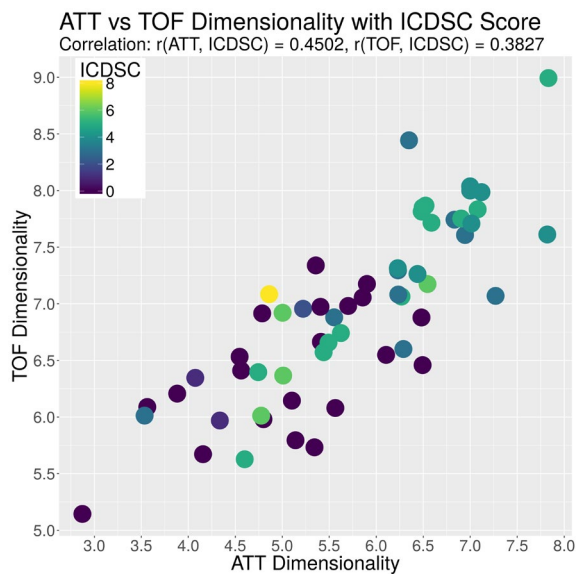


Figure 60: Plot of the dimensionality of the attenuation (ATT) vs. the dimensionality of the time of flight (TOF). Every dot represents one patient on one day, the color represents the ICDSC score of that patient on that day

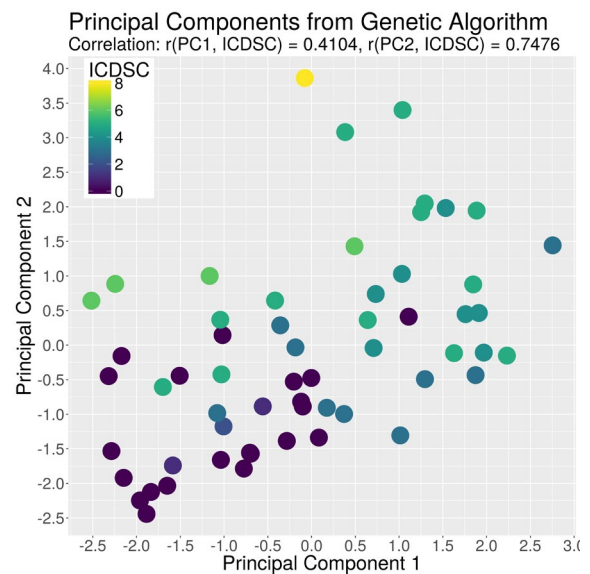


Figure 61: Plot of the principal component derived by the genetic algorithm (GA) based on the ICDSC score on the X-axis and the principal component derived by the GA based on the ICDSC on the Y-axis. Every dot represents one patient on one day, color coded with the ICDSC index on that day

In order to detect maleficent changes in the brain by the SAE patients, a feature called data dimensionality is proposed. This is a measure for asynchronicity of frequency-related features.

In a healthy brain, frequency-related features should be almost in sync, while a brain disorder lowers the synchronicity and therefore increases the dimensionality of the data [54] [55] [63]. To compute this feature, at least two frequency-dependent time series, in this case the time of flight (TOF) or attenuation (ATT) for 10 different frequencies are used. For each data matrix, the principal component analysis (a singular value decomposition of the data matrix) is computed and especially the explained variance for each component is of interest. The dimensionality of the data is defined as the minimal number of components necessary to reach a threshold of explained variance, for example how many principal components are necessary to explain 95 percent of the variance of the system. This imitates the value of the dimensionality of the data from 1, meaning that almost all of the dynamics of the system can be described by using only 1 linear combination of the input values, to the number of frequencies used, which means that the value shows a different dynamic for every frequency [1] [64]. The Genetic Algorithm (GA) feature selection is based on the nature concept of evolution and was first adapted by Barricelli [65] [66], but first Holland made the concept widely known in 1975 [67]. The algorithm contains the steps of creating a population, assessing the fitness of every individual, mating of the fittest and mutation. It has been shown by Schmude [68] that GA feature selection is a viable option in the context of ACG data. In the figures 58-61 every dot represents one patient at one measurement day. In the fig.58 and fig.60 the x-axis represents the dimensionality calculated from the attenuation (ATT) time series and the y-axis represents the dimensionality calculated from the time of flight (TOF) time series. Some details of the dimensionality parameters were described in the upper part of this section. The full details of this clinical study will be published shortly in the PLSONE journal.



Figure 62: Shows the ACG System- UltraEASY 2 used for clinical trials. It consists two ACG probes joined by a strap on the patient's head connected to an output device with touchscreen to record and data presentation. All components are assembled to a trolley to be transportable

In this first study with SAE patients, the dimensionality parameter reaches a good correlation with the SOFA score which is surprising since the parameter was deterministically chosen based on theoretical assumptions. The dimensionality parameter itself is designed to be a measure of disorder in the brain which might explain why no single laboratory parameter could be correlated with it. Since the dimensionality gives a measure for the system as a whole, like the SOFA score, it would be susceptible to many different parameters and their interactions, rather than single parameters of organ failure. The next fig.63 gives a general overview on the dimensionality development on the patients with SAE.

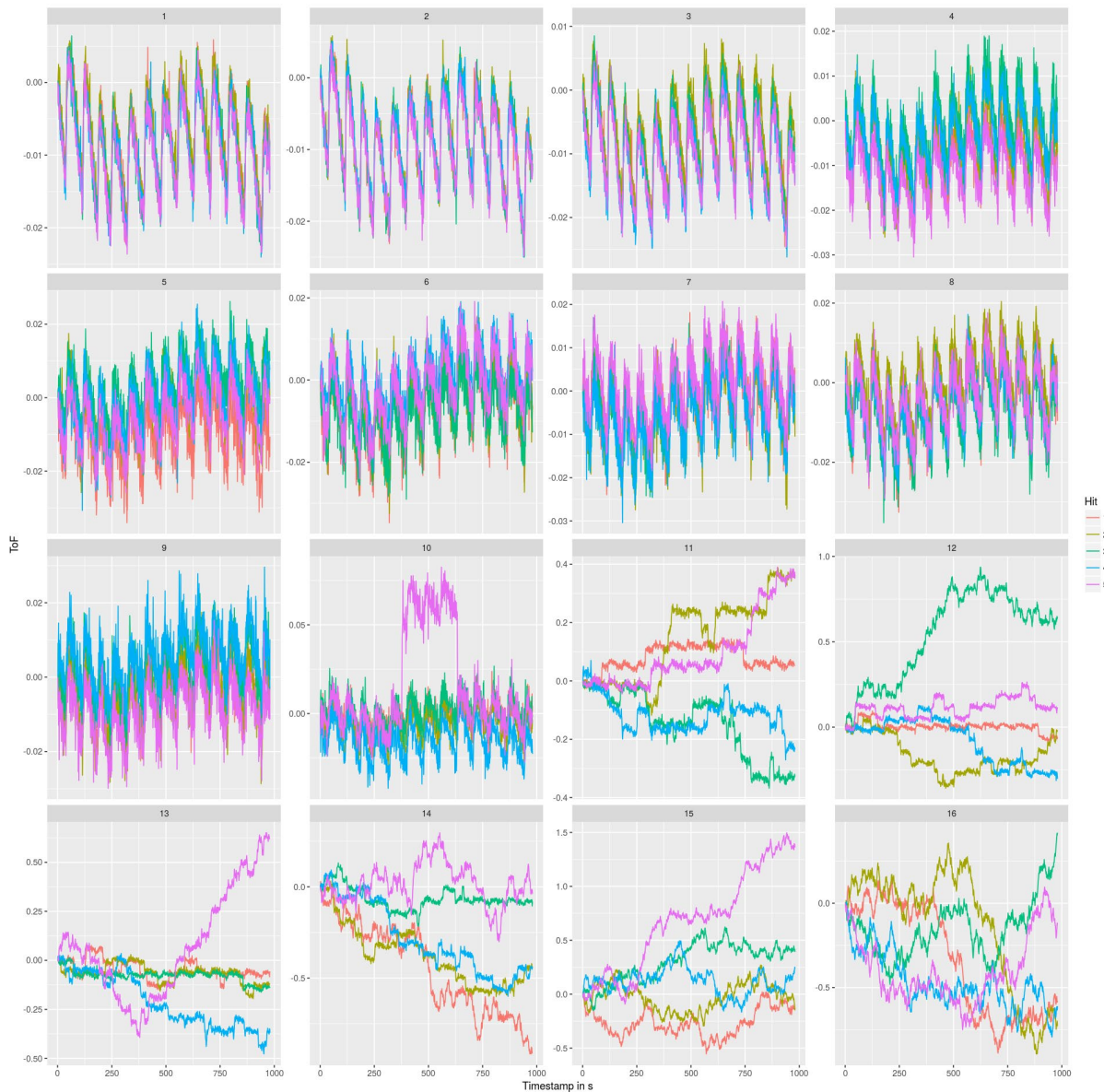


Figure 63: Shows the ACG System readings of 5 different frequencies - a theoretical parameter based on crafted assumptions and referred as the dimensionality of the recorded data can be calculated from the curves behavior. The ToF values are plotted as relative in $[\mu s]$ and shows the increasing pathology 1 – less, 16- most

The ACG data were recorded with an average signal strength of 80.9 percent \pm 14.6percent, which is sufficiently high. The data were processed using two different approaches. The first is a deterministic one where a parameter based on theoretical assumptions was crafted, referred to as the dimensionality of the data. The second one is a stochastic one which involves genetic algorithm (GA) feature selection and principal component analysis. Both approaches show that complex changes in the brain tissue during a septic shock can be detected by the ACG. It will help, the ACG method, to establish itself as a possible non-invasive monitoring and future medical diagnostic procedure for SAE patients. In further studies, the results of this pilot study should be further validated, also with the aid of other classic diagnostic methods of SAE as

EEG, MRI and biomarker. The implementation of a quicker and more effective diagnostic method will provide significant economic benefits, in addition to the benefits of better patient outcomes and meaningful healthcare cost savings.

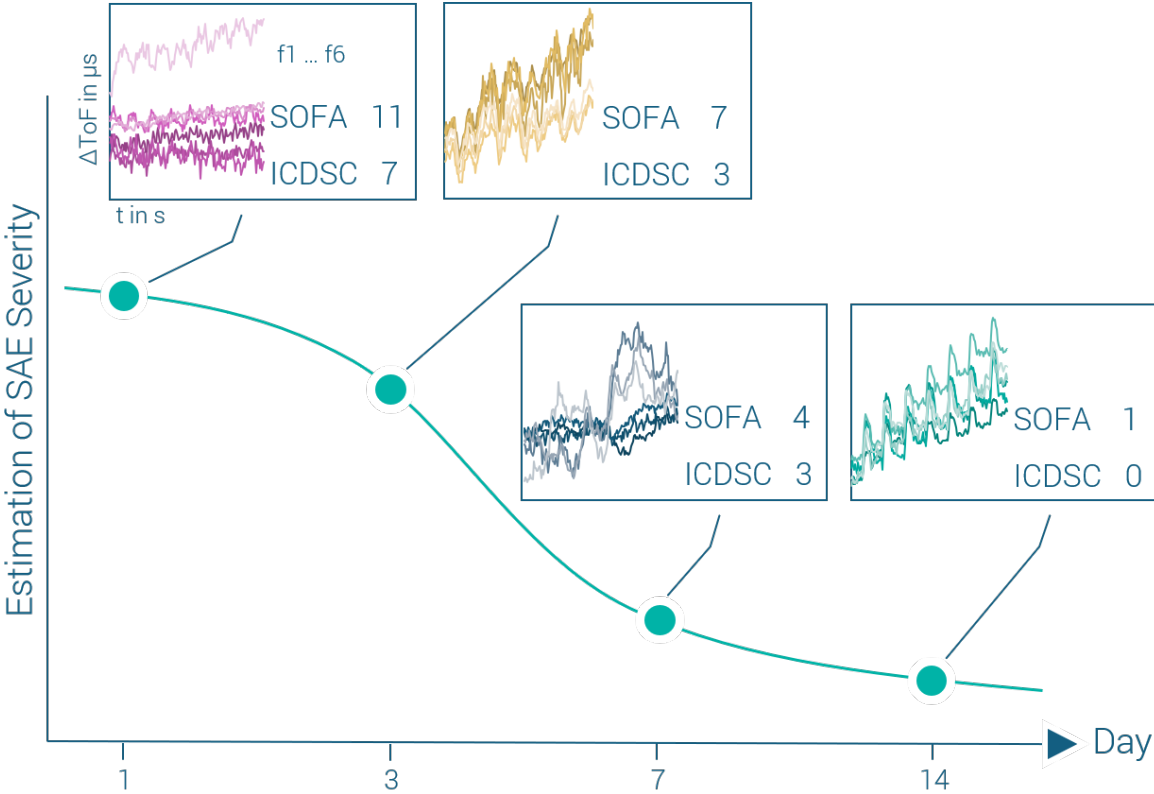


Figure 64: Behaviour of the ToF curves during the long-term monitoring, up to 14 days, by patients with sever SAE during their therapy. For near description please see chapter 9

Generally speaking, for many years, there has been no attainable brain monitoring solution to continuously check the brain’s health status during routine check-ups, for surgery (anaesthesia, preoperative, during and post-operative) and in critical care sessions. Slowly, the monitoring of brain functions is asserting its importance beside cardiac performance and other major organ functions, that are monitored intensively. This trend relies heavily on technical innovations, enabling the understanding of our most important and most complex organ. Thanks to modern computer technology, ACG enables, among other things, a fast, very precise and non-invasive diagnosis of the brain tissue in the beginning of the therapeutic time frame as well as further, continuous brain monitoring. Furthermore, brain monitoring can tackle a whole array of neuropathology’s and as preliminary studies have shown, the possible application of ACG far exceeds the diagnosis and treatment of WML or SAE.

Currently, a precise diagnosis for neuro-degenerative disease and treatment is only possible with three imaging methods, which are PET (Positron Emission Tomography), CT (Computed Tomography) and MRI (Magnetic Resonance Imaging). These so-called “gold standard” methods require considerable time and have high costs (i.e. both significant capital and

operating expenses). Moreover, radiologists or neurologists are required to read the scans and to provide a precise diagnosis. Importantly, while treating a cerebral pathology, time is the most critical factor (i.e. because "time is brain"), ACG enables an individual assessment and continuous monitoring at-risk patients (long-term and remote patient monitoring). This works goal is therefore to add ACG to the existing "gold standard" technologies. Additionally, each new clinical study broadens the field of application for this fascinating ultrasound technology. A fast and precise diagnosis is paramount for saving lives and with an aging population, Parkinson's disease, dementia, SAE, mTBI and stroke care presents an EU-wide social challenge with regard to healthcare and quality of life. These new applications will disrupt the current market for brain diagnostic devices and improve the ability to save lives as well as greatly reduce costs in the healthcare sector and for the society as a whole.

10 Chapter 10

10.1 Conclusion und Outlook

The accuracy and patient-friendliness of the ACG method as well as its primer medical diagnostic value demonstrated in this work makes it suitable for clinical use. The WML detection can be used on a selective basis in those patients whose indication for invasive CT or MRT measurement is doubtful for many reasons and may, if appropriate, serve as a decision support for the implantation of ulterior pharmaceutical or otherwise treatment. Beside the WML and SAE, the use of ACG method seems particularly useful in the traumatic brain injury patients, stroke patients, as these patients often do not undergo e.g. invasive ICP monitoring and are at risk of an elevated ICP being detected too late. In addition, it provides a good estimation for continuous monitoring of cerebral autoregulation in non-sedated and sedated patients.

Further improvements in the accuracy of signal acquisition through the development of reference databases and the use of new methods such as the fuzzy pattern classification appear possible and are planned for the future. In particular, a hybrid approach, in combinations of linear, non-linear, genetic algorithms and fuzzy pattern methodologies are considered promising. In particular, further physiologically based features (for example arterial BP invasive or non-invasive, ECG signal, ICP, age, gender, etc.) could be examined for their suitability for the classification of the patient data. Furthermore, in the case of the fuzzy pattern model involving the autoregulation, it should also be examined whether dimensionality leads to optimizations similar to those in the genetic case model. With regard to clinical application, it also seems interesting to investigate the extent to which it is possible to use the data collected during an invasive ICP measurement for a patient-specific calibration of ACG as the nICP method. This could potentially shorten the duration of the invasive measurement and significantly reduce the risk of infection for the patient.

This work shows the molecular acoustic background of the Acousto-Cerebro-Graphy, as well as the disrupt and paradigm breaking concept of using the multispectral acoustic quasi-constant signal packages to collect the embrace information about the brain tissue alteration. My work on the ACG method lead to several invention in the filed of medical system construction, signal processing and matter/tissue classification. These inventions are granted already with several US and PCT Patents – five of them are directly used in this work, to describe the measurement procedure and are depicted in the publication list. An advanced empirical research was an important element of this work approach.

Concluding, the presented thesis consists the following original achievements:

1. The originally designed paradigm breaking concept of ACG method proved to be useful in acute and chronic brain injury patients and in the near future will disrupt the current market for brain diagnostic devices
2. ACG is valuable extension of convectional ICU cardio-vascular monitoring to the cerebrovascular monitoring for holistic supervision of the multimorbid patients. A fast and precise diagnosis is paramount for saving lives, increasing the healthcare standards and the quality of life within an aging population.
3. Digitized medical data is a tremendous asset and vital currency for connected healthcare. Data analytics as presented in this thesis brings it all together, completing the connected health ecosystem by simultaneous data reduction as shown on fig.50. Analytics of the new applications as ACG, makes the data actionable and will ultimately transform healthcare by enabling decisions to be made by each of the members in the full circle of care around an individual.
4. Introduced patented algorithms considerably improved the accuracy of signal acquisition and tremendous accelerate the data processing. Its “filter” performance can be easily adapted to the other application fields as e.g. telecommunication and long-range sensing. They allow also a further miniaturisation on the system up to ACG-on-Chip.
5. The algebraic research and inventions presented in this thesis in chapter 6 are on common nature and can be plainly applied to different medical and technical fields of application. It retains its validity in the field of MRT signal acquisition and processing as well as the power net stability and some aspects of geological exploration.

Hypotheses presented in this works are current, original, important, and in many aspects, pioneer as it is its verification. The present work is thematically located in the interdisciplinary field of engineering, physics, mathematics and medicine. My concern was to make the topic discussed comprehensible and interesting for both doctors and engineers. I hope that the related content balancing act has succeeded.

Table of Illustration

Figure 1: Normal pressures and shear stresses which act on a volume element of an elastically deformable medium [2].....	3
Figure 2: Cerebral blood flow as a function of central blood pressure	14
Figure 3: Anatomy of Cerebrovascular system (poster cedars-sinai-edu)	15
Figure 4: Anatomy of the brain (Anatomical Chart Company, Illinois)	17
Figure 5: Major cerebral arteries and the Circle of Willis [15]	19
Figure 6: The brain venous system [16].....	20
Figure 7: The relationship between intracranial pressure and volume.....	22
Figure 8: Propagation of the cardiac pulse pressure signal	23
Figure 9: Layers model of the human head (*with ventricles).....	27
Figure 10: Imaging plane of the human head.....	29
Figure 11: Axial (transversal) plane view of the brain (ultrasound probe position) with possible acoustical field coverage	29
Figure 12: Oversimplified layers model of the human head. Ultrasound signal traveling from transmitter T to receiver R in a Medium with dimension d.....	33
Figure 13: ToF to heartbeat curve of a 72 years old male, taken with ACG system – please take a closer look on the reversal P1 and P2 notches reflecting a state of disturbed autoregulation as described in Ch.2.3 – Intracranial pressure ICP	35
Figure 14: Scheme of a system for measurement of phase relations of acoustic wave packets.....	37
Figure 15: Approximation of sampled signal.....	38
Figure 16: Diagram of time estimation method T_p	38
Figure 17: Diagram of time estimation method T_p	49
Figure 18: Diagram of time estimation method T_p	49
Figure 19: Diagram of time estimation method T_p	50
Figure 20: Diagram of time estimation method T_p	50
Figure 21: Block processors draft	56
Figure 22: The operation of block processors	57
Figure 23: Block processor model.....	58
Figure 24: Block processor - Cyclic clock (inside view).....	59
Figure 25: Matrix block processor – Signal (inside view).....	59

Figure 26: Matrix block processor - Retrieve UV block (inside view).....	60
Figure 27: Matrix block processor – Oscilloscope. No transient values are observed on the left side of the target-performance comparison curves – top diagram is the target curve; the middle is the performance curve with NO transient behavior and the lower curve is the bias with NO transient behavior also (details in text)	62
Figure 28: Stream processors draft.....	64
Figure 29: The operation of stream processors	65
Figure 30: TRI stream processor model	66
Figure 31: Stream processor TRI – Signal (inside view).....	67
Figure 32: Stream processor TRI – RetrieveUVb (inside view).....	68
Figure 33: TRI stream processor – Oscilloscope. The transient values are well observed on the left side of the target-performance comparison curves – top diagram is the target curve the middle is the performance curve with the transient behavior and the lower curve is the bias with similar transient behavior (details in text).....	68
Figure 34: LSM stream processor model.....	69
Figure 35: LSM Streamer – Signal (is identical as on fig.21).....	70
Figure 36: Stream LSM processor – RetrieveUVb	71
Figure 37: Stream LSM processor – Scope. Some transient values can still be observed on the left side of the signal curves – top diagram is the target curve; the middle is the performance curve with very minor transient behavior and the lower curve is the bias curve with also very minor transient behavior (details in text).....	71
Figure 38: Stream processor TRI (RetrieveUVb) with averaging block.....	72
Figure 39: Stream LSM processor (RetrieveUVb) with averaging block.....	72
Figure 40: Running average (n=5) - (inside view).....	72
Figure 41: LSM stream processor with n=5 averaging – Oscilloscope. The subplots follow the same structure as before. Top diagram is the target curve, the middle is the performance curve and the lower curve is the bias – please take a closer look on the transient response of the system. Next figure shows a zoom look on this behavior.	73
Figure 42: Stream processor TRI with n=5 averaging and oscilloscope zoom on the first data points. On the left side of the signal the transient values can be observed. The subplots follow the same structure as before. Top diagram is the target curve, the middle is the performance curve and the lower curve is the bias.....	73
Figure 43: Position of transducers and the shapes of the sent signal and a received one.....	74
Figure 44: Finding the best fitting sine-like curve	75
Figure 45: Distortions at beginnings of pulses	76

Figure 46: Multispectral signal with H=10 frequencies	77
Figure 47: At the top a sample sequence - below to the left, the same sequence taken modulo 2.0, 5.0, 0.5 and 1.0, respectively. To the right there are the results of unwinding the sequence to the left	80
Figure 48: Signals with improperly (top) and with properly distributed peaks (bottom).....	81
Figure 49: A block diagram of a TUS System. The ultrasound probes are not depicted in this diagram	83
Figure 50: Comparison representation of the total recorded data using the advance TUS system. Considering the value potential, it holds, the data is comparably small in size. The single measurement contains 2x 20 frequencies with recalculated phases (32-bit) and 16-bit amplitude value – 40x 48-bit in total.....	88
Figure 51: MRI evaluation, representative data sets, * only the implantation site of the intracranial pressure probe showed locally very limited changes in the T2 * sequence	92
Figure 52: Histological analyzes Sheep brain, representative images of the two groups.....	93
Figure 53: (A) statistical evaluation of the Nissl-positive cell counts (neurons) in Nissl staining. There is no significant difference between the two groups; (B) Statistical evaluation of the stained myelin area in the Luxol stain. There is no difference between	94
Figure 54: ACG is a set of techniques designed to capture states of human brain tissue and its changes	97
Figure 55: Result of the GBM-Classification. The points are represented by the classification probability to the groups L0, L5 and L30. The filled symbols represent the projection of the points from groups L0 and L30 on the plane L0-L30 probability.....	99
Figure 56: Comparison of varying force of two most discriminative variables: AlphaQuo_75_3 and QuasiC_50_4: The most extremal groups L0 and L30 are easily distinguishable	100
Figure 57: Density distribution of two most discriminative variables: AlphaQuo_75_3 and QuasiC_50_4.....	101
Figure 58: Dimensionality plot of the attenuation (ATT) versus time of flight (TOF). Every dot represents one patient on one day, the color represents the SOFA score of that patient on that day ..	104
Figure 59: Plot of the principal component derived by the genetic algorithm (GA) based on the SOFA score on the X-axis and the principal component derived by the GA based on the ICDSC on the Y-axis. Every dot represents one patient on one day, color coded with the SOFA index on that day.....	104
Figure 60: Plot of the dimensionality of the attenuation (ATT) vs. the dimensionality of the time of flight (TOF). Every dot represents one patient on one day, the color represents the ICDSC score of that patient on that day	104
Figure 61: Plot of the principal component derived by the genetic algorithm (GA) based on the ICDSC score on the X-axis and the principal component derived by the GA based on the ICDSC on the Y-axis. Every dot represents one patient on one day, color coded with the ICDSC index on that day	104

Figure 62: Shows the ACG System- UltraEASY 2 used for clinical trials. It consists two ACG probes joined by a strap on the patient's head connected to an output device with touchscreen to record and data presentation. All components are assembled to a trolley to be transportable..... 106

Figure 63: Shows the ACG System readings of 5 different frequencies - a theoretical parameter based on crafted assumptions and referred as the dimensionality of the recorded data can be calculated from the curves behavior. The ToF values are plotted as relative in [μ s] and shows the increasing pathology 1 – less, 16- most..... 107

Figure 64: Behaviour of the ToF curves during the long-term monitoring, up to 14 days, by patients with sever SAE during their therapy. For near description please see chapter 9 108

Table of Tables

Table 1: The basic parameters assumptions for the human skull-brain model [34].....	30
Table 2: Human head model of the ultrasonic signal attenuation and expected time of flight along the measurement path [34].....	31
Table 3: Time allocation and consuming table for the phase calculation procedure.....	43
Table 4: Optimisation table for the used procedure	44
Table 5: Matrix block processor - Value summary	61
Table 6: Presentation of the release animal clinical parameters.....	91
Table 7: Statistical data of the clinical parameters listed in Tab.5	91
Table 8: Statistical data - Student distance of a selection of variables.....	100
Table 9: Comparison of the Pearson correlations of the dimensionality parameters with the major components obtained by genetic algorithm and the clinical parameters	103

References

- [1] M. Wrobel, "Advanced ultrasonic interferometer and method of non-linear classification and identification of matter using same". USA Patent US000007878062B2, 27 06 2006.
- [2] W. Schaaffs, Molekularakustik, Springer-Verlag, 1963.
- [3] E. Mach, Die Mechanik in ihrer Entwicklung, Leipzig: Brockhaus , 1883.
- [4] C. Schäfer, Die Einführung in der theoretischen Physik, B.G. Teubner, 1962.
- [5] R. Hooke, Lectures de potentia restititiv, London, 1678.
- [6] Landolt-Börnstein, Group II Molecules and Radicals - 5: Molecular acoustics, Springer-Verlag, 1967.
- [7] E. Mach, Prinzipien der Wärmelehre, Johann Ambrosius Barth, 1919.
- [8] C. Toliás and S. Sgouros, Initial Evaluation and Management of CNS Injury, Wayback Machine, 2006.
- [9] H. Mattle, M. Mumenthaler and E. Taub, Fundamentals of Neurology, Thieme-Verlag, 2016 | 2nd edition.
- [10] P. D. Hurn and R. J. Traystman, Overview of Cerebrovascular Hemodynamics, Toronto: Primer on Cerebrovascular Diseases by Academic Press, 1997.
- [11] E. V. Reis, Oxygen and Cerebral Blood Flow, Toronto: Primer on Cerebrovascular Diseases by Academic Press, 1997.
- [12] R. Tadeusiewicz, Sieci neuronowe, Akademicka Oficyna Wydawnicza RM, 1993.
- [13] R. Tadeusiewicz, Problemy biocybernetyki, Warszawa: Panstwowe Wydawnictwo Naukowe, 1991.
- [14] R. Rossen, H. Kabat and J. P. Anderson, "Acute arrest of cerebral circulation in man," *Arch Neur Psych*, vol. 50, no. 5, pp. 510-528, 1943.
- [15] J. G. Chusid, Correlative Neuronanatomy and Functional Neurology, Los Altos: Lange Medical Publications, 1970.
- [16] H. A. Shenkin, M. H. Harmel and S. S. Kety, "Dynamic anatomy of the cerebral circulation," *Arch. Neurol. Psychiat.*, vol. 60, pp. 240-252, 1948.
- [17] K. Welch, Primer on Cerebrovascular Diseases, Toronto: Academic Press, 1997.
- [18] B. Mokri, "The Monro-Kellie hypothesis: applications in CSF volume depletion," *Neurology*, vol. 56, pp. 1746-1748, 2001.
- [19] G. Burrows, On Disorders of the Cerebral Circulation and on the Connection between Affections of the Brain, Philadelphia: Lea & Blanchard, 1848.
- [20] H. Cushing, The Third Circulation in Studies in Intracranial Physiology and Surgery, London: Oxford University Press, 1926.

- [21] F. Gjerris and J. Brennum, "The cerebrospinal fluid, intracranial pressure and herniation of the brain," in *Clinical Neurology and Neurosurgery*, Copenhagen, FADL's Forlag Aktieselskab, 2004, pp. 179-196.
- [22] P. H. Raboel and J. J. Bartek, "Intracranial Pressure Monitoring: Invasive versus Non-Invasive Methods," in *Critical Care Research and Practice*, 2012.
- [23] M. E. Wagshul, P. K. Eide and J. R. Madsen, "The pulsating brain: A review of experimental and clinical studies of intracranial pulsatility," *Fluids and Barriers of the CNS*, vol. 8, no. 5, 2001.
- [24] S. R. Heisey and T. Adams, "Role of Cranial Bone Mobility in Cranial Compliance, Experimental Study," *Neurosurgery*, Vols. Volume 33, Number 5, no. November 1993, 1993.
- [25] "Neurowissenschaft, Cerebrospinalflüssigkeit," Spektrum.de, 28 10 2018. [Online]. Available: www.spektrum.de.
- [26] "Liquordruck," Roche Lexikon Medizin, 2019. [Online]. Available: <https://www.roche.de/lexikon/index.htm>.
- [27] W. Wegner, *Enzyklopädie Medizingeschichte*, Berlin: De Gruyter, 2005.
- [28] A. Anoop, P. K. Singh, R. S. Jacob and S. K. Maji, "CSF Biomarkers for Alzheimer's Disease Diagnosis," *International journal of Alzheimer's disease*, 2010.
- [29] P. Grätzel von Grätz, *Der Schlaganfall*, Berlin: Broschüre des BMBF zum Integrierten Forschungs- und Behandlungszentrum (IFB), 2012.
- [30] K.-J. Wolf and F. Fobbe, *Farbkodierte Duplexsonographie - Grundlagen und klinische Anwendung*, Stuttgart: Thieme-Verlag, 1993.
- [31] C. Burrell and P. Chauhan, "Intracranial Dispersion Model," Defence R&D Canada, Toronto, 2012.
- [32] N. Lynnerup, J. Astrup and B. Sejrsen, "Thickness of the human cranial diploe in relation to to age, sex and general body build," *Head & Face Medicine*, vol. 13, no. 1, 2005.
- [33] M. Pakula, F. Padilla and P. Laugier, "Influence of the filling fluid on frequency-dependent velocity velocity and attenuation in cancellous bones between 0.5 and 2.5 MHz," *Journal of the Acoustical Society of America*, vol. 126, no. 6, p. 3301–3310, 2009.
- [34] F. W. Kremkau, R. W. Barnes and P. C. McGraw, "Ultrasonic attenuation and propagation speed in normal human brain," *Journal of the Acoustical Society of America*, vol. 70, no. 1, p. 29–38, 1981.
- [35] F. Fry and J. Barger, "Acoustical properties of the human skull," *Journal of the Acoustical Society of America*, vol. 63, no. 5, p. 1576–1590, 1978.
- [36] T. Ueno, B. Macias, W. Yost and A. Hargens, "Pulsed phase lock loop device for monitoring intracranial pressure during space flight," *J Grav Physiol*, vol. 10, pp. 117-118, 2003.

- [37] M. Heifetz and M. Weiss, "Detection of skull expansion with increased intracranial pressure," *J of Neurosurg*, vol. 55, pp. 811-812, 1981.
- [38] S. Heisey and T. Adams, "Measurement of cranial bone mobility," David Kopf Instruments - Kopf Carrier No. 31, Tujunga, CA, 1992.
- [39] G. Steinbach, B. Macias, K. Tanaka, W. Yost and A. Hargens, "Intracranial Pressure Dynamics Assessed by Noninvasive Ultrasound During 30 Days of Bed Rest," *Aviation, Space, and Environmental Medicine*, vol. 76, no. 2, pp. 85-90, 2005.
- [40] B. Schmidt, "Nichtinvasive Erfassung des Hirndrucks mittels des transkranialen Dopplersignals und der Blutdruckkurve unter Verwendung systemtheoretischer Methoden," TU Chemnitz, Chemnitz, 2003.
- [41] M. Wrobel, "Phaseshift interferometer". USA Patent US020070100578A1, 1 11 2005.
- [42] L. Jodlowski, "Measurement of harmonic signal phase with application of low frequency of sampling," *Molecular & Quantum Acoustics*, vol. Vol.19 , 1998.
- [43] L. Jodlowski, M. Szustakowski and M. Piszczek, "Analysis of Measurement Possibilities of Long Bulk Wave for Technical Application," *Molecular & Quantum Acoustics*, vol. Vol.20, 1999.
- [44] L. Jodlowski, M. Szustakowski and M. Piszczek, "Passage Time Measurement of Medium Probe Signal with the Use of Phase Method with Quasi-Continuous Wave," *Molecular & Quantum Acoustics*, vol. Vol.20, 1999.
- [45] Matlab Documentation, Natick, Massachusetts.: The MathWorks, Inc., 1994-2019.
- [46] R. Zurmühl and S. Falk, *Matrizen und ihre Anwendungen 1 - Grundlagen. Für Ingenieure, Physiker und Angewandte Mathematiker*, Berlin: Springer, 1997.
- [47] A. Kolany and M. Wrobel, "Phase detection method based on a receiving sequence of scanned values". European Patent Patent EP000003207635B1, 14 10 2015.
- [48] A. Kolany and M. Wrobel, "Phase detection method based on a plurality of consecutive values of a receiving signal". European Patent Patent EP000003207634B1, 14 10 2015.
- [49] A. Kolany and M. Wrobel, "Phase detection method based on a plurality of consecutive values of a receiving signal". USA Patent US000010135449B2, 14 10 2015.
- [50] A. Kolany and M. Wrobel, "Some algebraic and algorithmic problems in Acoustocerebrography," *Bulletin of the section of logic*, vol. Vol.45, no. Number $\frac{3}{4}$, 2016.
- [51] P. He, "Experimental verification of models for determining dispersion from attenuation," *IEEE Transactions on Ultrasonics, Ferroelectrics, and Frequency Control*, vol. 46, no. 3, p. 706–714, 1999.
- [52] T. Szabo, "Diagnostic Ultrasound Imaging," *Inside Out*, no. Elsevier Academic Press, pp. 75-, 2004.

- [53] A. Dreyer, "Bericht Auswertung Arbeitspaket B.1 - Early discrimination between Cerebral Hemorrhage and Obstructive Ischemia," Fraunhofer-Institut für Zelltherapie und Immunologie, Leipzig, 2014.
- [54] M. Wrobel, A. Dabrowski, A. Kolany, A. Olak-Popko, R. Olszewski and P. Karłowicz, "On ultrasound classification of stroke risk factors from randomly chosen respondents using non-invasive multispectral ultrasonic brain measurements and adaptive profiles," *Biocybernetics and Biomedical Engineering*, vol. 36, no. 1, pp. 18-28, 2015.
- [55] P. Schmude and M. Wrobel, "Detecting Changes in the Human Brain caused by Atrial Fibrillation using Ultrasound and Deep Learning," *Poster presented at European Stroke Conference*, no. E-Poster Ref. No. L 022, 2017.
- [56] W. Dobkowska-Chudon, M. Wrobel, E. Frankowska, A. Dabrowski, P. Karłowicz, A. Zygadlo, A. Krupienicz, A. Nowicki and R. Olszewski, "Utilizing Comparison Magnetic Resonance Imaging and Acoustocerebrography Signals in the Assessment of Focal Cerebral Microangiopathic Lesions in Patients with Asymptomatic Atrial Fibrillation (Preliminary Clinical Study Results)," in *EAA 2016 Congress, Archives of Acoustics 2016, Volume 41, Issue 2*, Jastrzębia Góra, Poland, 2016.
- [57] R. Olszewski, W. Dobkowska-Chudon, M. Wrobel, P. Karłowicz, A. Dabrowski, A. Krupienicz, T. Targowski and A. Nowicki, "Is Acoustocerebrography a new non-invasive method for early detection of the brain changes in patients with hypertension?," in *Poster accepted for European Society of Cardiology Conference*, Barcelona, August 2017.
- [58] W. Dobkowska-Chudon, M. Wrobel, P. Karłowicz, A. Dabrowski, A. Krupienicz, T. Targowski, A. Nowicki and R. Olszewski, "Detecting cerebrovascular changes in the brain caused by hypertension in atrial fibrillation group using acoustocerebrography," *PLoS ONE*, vol. Volume 13, no. Issue 7, 2018.
- [59] N. Chaudry and A. Duggal, "Sepsis Associated Encephalopathy," *Advances in Medicine*, no. ID 762320 , 2014.
- [60] M. Bogdan, A. Kolany, U. Weber, R. Elze and M. Wrobel, "Computer Aided Multispectral Ultrasound Diagnostics Brain Health Monitoring System based on Acoustocerebrography," in *conference paper MEDICO 2016; DOI: 10.1007/978-3-319-32703-7_191*, Cyprus, 2016.
- [61] A. Sievert, G. Richter, J. Ehler, M. Wrobel, R. Klemp, T. Mencke, G. Nöldge-Schomburg and M. Sauer, "Pilotstudie zur Diagnose einer septischen Enzephalopathie durch Akustocerebrografie - Zwischenauswertung," in *Poster presented at DAC Nürnberg, May 4, 2017; E-Poster Ref. No. 2.2.12*, Nürnberg, 2017.
- [62] M. Sauer, G. Richter, A. Sievert, T. Mencke, J. Ehler, P. Schmude, M. Wrobel, R. Klemp and G. Nöldge-Schomburg, "Diagnose einer septischen Enzephalopathie durch Akustocerebrografie - Ergebnisse einer Pilotstudie," in *Poster presented at DIVI Leipzig, Dec 8, 2017; E-Poster Ref. No. EP/11/01*, Leipzig, 2017.

- [63] L. Sekhar, M. Sun, D. Bonaddio and R. Sciabassi, "Acoustic recordings from experimental saccular aneurysms in dogs," *Stroke*, vol. 21, no. 8, pp. 1215-1221, 1990.
- [64] M. Wrobel and S. Stergiopoulos, "Non-invasive monitoring of intracranial dynamic effects and brain density fluctuations". USA Patent US000007854701B2, 21 12 2010.
- [65] N. Barricelli, "Esempi numerici di processi di evoluzione," *Methodos*, p. 45–68, 1954.
- [66] A. Fraser, "Monte Carlo analyses of genetic models," *Nature*, vol. 181, no. 4603, p. 208–209, 1958.
- [67] J. Holland, *Adaptation in Natural and Artificial Systems*, Cambridge: MIT Press University of Michigan, , 1975.
- [68] P. Schmude, "Feature Selection in Multiple Linear Regression Problems with Fewer Samples Than Features," in *Rojas I., Ortuño F. (eds). Lecture Notes in Bioinformatics 2017, Part 1, 85-95*, Granada, 2017.

STATUTORY DECLARATION

I hereby declare that I have authored this thesis independently, that I have not used other than the declared sources / resources, and that I have explicitly marked all material which has been quoted either literally or by content from the used sources.

Leipzig, February 20, 2019

Mirosław Krystian Wróbel